UNIVERSITY OF PERUGIA

UNIVERSITY OF COPENHAGEN
FACULTY OF SCIENCE

G-quadruplex complexed with photosensitive ligands: a multi-technique biophysical study

Candidate: Valeria Libera

Tutors:
Dr. Lucia Comez
Prof. Alessandro Paciaroni
Prof. Lise Arleth

This thesis has been submitted to the PhD School of the Faculty of Science, University of Copenhagen and to the PhD School of Science and Technology for Physics and Geology - XXXV cycle of the University of Perugia

Contents

Abstract

G-quadruplexes (G4s) are non-canonical four-stranded DNA helical structures formed through the stacking of four in-plane Hoogsteen-paired guanine bases. Conformational triggers of G4s have a huge potential in many areas, from nanotechnology to biomedicine. The aim of this thesis is to investigate the G4 conformational changes upon ligand complexation and by light activation. Firstly, a few small molecules were selected and tested as DNA ligands proving their capability to induce G4 secondary structure rearrangements and stabilisation. Among them, two photosensitive ligands were chosen: TMPyP4 porphyrin and photo-isomer pyridinium-decorated dithienylethene (DTE). Irradiation is a precise method in which timing, location, and strength of light can be easily controlled. Therefore, the use of photosensitive ligands could represent a molecular tailoring method for controlling changes in morphology and stability of G4s by non-invasive irradiation. Although several classes of drugs able to form complexes with G4s have been identified, the investigation of the G4-ligand interaction under different experimental conditions is still a challenge requiring the use of many techniques operating on different spatial and temporal scales.

Here, the results from a multi-technique approach combining structural and molecular information to get access to the G4s properties are reported. In-house techniques, such as UV-Visible absorption, circular dichroism and fluorescence spectroscopy, were combined with small-angle X-ray/neutron scattering methods and UV-resonant Raman spectroscopy available at large-scale facilities. To provide new insights from the experimental data, a multivariate singular value decomposition method was employed to extract quantitative information from complex datasets.

Overall, the proposed strategy allowed obtaining an experimental scheme to trigger conformational variations in the G4-drug complexes and to define the photo-physical parameters of the irradiation process (photo-reaction efficacy, irradiation time, photo-product stability) according to specific applications. One

of the most important results of the work concerns the irradiation of the complex formed by the human G4 telomeric sequence $AG_3(TTAG_3)_3$ (Tel22) and TMPyP4. At DNA concentration of tens of micromolar, irradiation with 430 nm partially destroys the Tel22 structure, possibly by oxidising the guanines. Interestingly, at a concentration one order of magnitude larger, porphyrin binding promotes Tel22 dimerisation and light irradiation increases dimer fraction.

In the future, the synergistic use of information at different structural levels will serve as a diagnostic strategy to carry out photo-control of G4 dimerisation and stabilisation or tetrad disruption. Apart from applications in biomedicine, the use of photosensitive ligands to modulate the conformation of G4 complexes could be employed to tailor DNA nanometric bricks for light-switching reversible applications and biosensing technologies. This aspect was highlighted in the case of the interaction between Tel22 and DTE.

This thesis is divided as follows: the first chapter is a brief introduction to the polymorphic world of G4s, focusing the attention on their structure, possible applications, and finally on the specific case of Tel22. The second chapter gives an overview of the techniques employed for the experiments: UV-Vis absorption, circular dichroism, UV resonant Raman, and fluorescence spectroscopy and small-angle X-ray/neutron scattering. An additional section is dedicated to the singular value decomposition method. The third chapter collects the results obtained for Tel22 alone. This sequence is highly polymorphic, so it is essential to define its conformational structural properties in different environmental conditions. The fourth chapter is about the conformational changes induced on the Tel22 structure by the complexation with a set of small molecules. The fifth chapter extends the analysis to photosensitive ligands (DTE and TMPyP4) interacting with Tel22. Both dark and light conditions were taken into account. The last chapter is focused on the Tel22 conformational changes induced by complexation with porphyrin TMPyP4 in the high-concentration regime. These conditions allowed the use of small-angle scattering techniques at the characterisation of the quaternary structure level. At the end, conclusions and perspectives are discussed.

Danish abstract

G-kvadruplexer (G4'ere) er ikke-kanoniske firestrengede DNA-helixstrukturer, der dannes ved at stable fire Hoogsteen-parrede guaninbaser. Konformationsafhængige aktivatorer af G4'ere har et enormt potentiale inden for mange områder, fra nanoteknologi til biomedicin. Formålet med denne afhandling er at undersøge konformationsændringer af G4 ved ligandkompleksdannelse og ved lysaktivering. Først blev nogle små molekyler udvalgt og testet som DNA-ligander, for at vise deres evne til at inducere ændringer i sekundærstruktur og stabilitet af G4. Blandt dem, blev to lysfølsomme ligander valgt: TMPyP4-porfyrin og fotoisomer pyridinium-dekoreret dithienylethen (DTE). Lys-aktivering er en præcis metode, hvor timing, placering og styrke af lys-strålen let kan kontrolleres. Derfor kunne brugen af lysfølsomme ligander udgøre en molekylær skræddersyet metode til at kontrollere ændringer i G4's morfologi og stabilitet ved ikke-invasiv bestråling med lys. Selv om flere klasser af lægemidler, der kan danne komplekser med G4er er blevet identificeret, er undersøgelsen af G4-ligand-interaktionen under forskellige eksperimentelle betingelser stadig en udfordring, der kræver anvendelse af mange teknikker, der opererer på forskellige rumlige og tidsmæssige skalaer. Her præsenteres resultaterne af en multiteknisk tilgang, der kombinerer strukturel og molekylær information om G4's egenskaber. In-house teknikker, såsom UV-Vis absorption, cirkulær dichroisme og fluorescensspektroskopi, blev kombineret med småvinkelrøntgen-/neutronspredningsmetoder og UV-resonans Raman-spektroskopi, som er tilgængelige på store forskningsfaciliteter. For at give ny indsigt fra de eksperimentelle data blev der anvendt en multivariat singulærværdi dekomponeringsmetode til at udtrække kvantitativ information fra komplekse datasæt. Samlet set har den foreslåede strategi gjort det muligt at opnå en eksperimentel fremgangsmåde til at påvirke konformationelle variationer i G4-lægemiddelkomplekserne og at definere de fotofysiske parametre for lys-bestrålingsprocessen (fotoreaktionseffektivitet, bestrålingstid, fotoproduktstabilitet) i henhold til specifikke anvendelser. Et af de vigtigste resultater af arbejdet vedrører bestråling af det kompleks, der er dannet af den humane G4-

telomersekvens $AG_3(TTAG_3)_3$ (Tel22) og TMPyP4. Ved en DNA-koncentration på et tocifret antal mikromolær ødelægger bestråling ved 430 nm delvist Tel22-strukturen, muligvis ved oxidering af guaninerne. Interessant nok ved en koncentration, der er en størrelsesorden større, fremmer porfyrinbinding Tel22-dimerisering, og lysbestråling øger dimerfraktionen. I fremtiden vil den synergistiske anvendelse af information på forskellige strukturelle niveauer tjene som en diagnostisk strategi til at foretage fotokontrol af G4-dimerisering og -stabilisering eller splittelse af tetrameren. Ud over anvendelser inden for biomedicin kan brugen af lysfølsomme ligander til at modulere konformationen af G4-komplekser anvendes til at skræddersy nanometriske DNA-blokke til reversible lysskiftende applikationer og biosensorteknologier. Dette aspekt blev fremhævet i eksemplet med interaktionen mellem Tel22 og DTE.

Chapter 1:

G-quadruplex: non-canonical DNA structure

1.1 Introduction

Non-canonical DNA structures, especially G-quadruplexes (G4s), have gained a lot of attention in the last two decades. Even though at first they were seen as structural curiosities, they are now recognised to be involved in a number of key genome functions. This chapter is not meant to be an in-depth review of G4 structure and functions but it is a short overview with the basic knowledge required to better understand this work. For excellent reviews see [1–6].

1.2 Brief history of G-quadruplex

DNA structure was solved in 1953 by Watson, Crick, and Franklin [7]. This event was the first milestone to study and visualise DNA topologies. At that moment, probably, nobody suspected that a "non-canonical" DNA structure could occur. After less than one decade, in 1962, Guedin et al. [8] revealed a DNA structure composed of two or more G-tetrads, i.e. four guanines (G) held together by Hoogsteen hydrogen bonds, stacked on top of each other. This structure, called G4, is shown in figure 1.1. The four guanines are held together by Hoogsteen hydrogen bonds [9]. The hydrogen bond network is not enough to guarantee a stable structure, therefore the G4 is primarily stabilised through the overlap of π orbitals of stacked guanines and by the presence of a monovalent cation centrally coordinated to O6 of the guanines [10]. DNA and RNA G4s can adopt very polymorphic structures having specific and crucial roles for many biological functions.

Preferentially, the folding of G4s is promoted by the presence of cations, such as K^+ (placed in between G-tetrads) and Na^+ (sitting in the tetrad plane) [11].

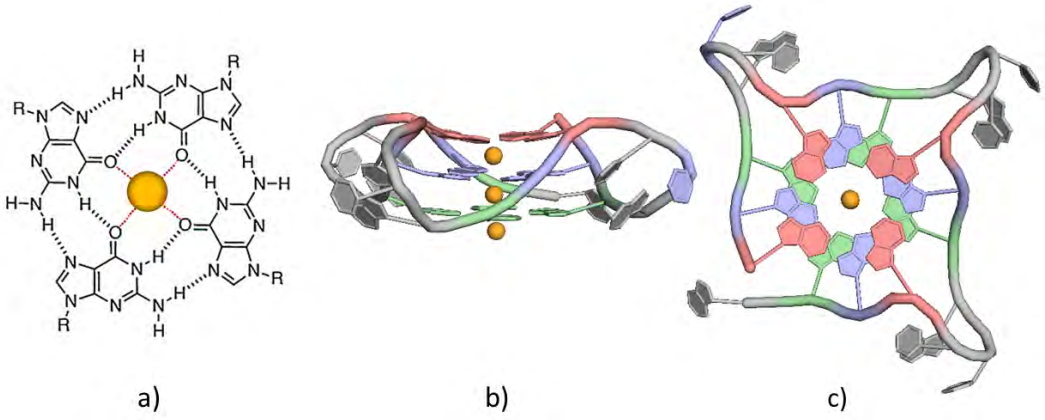

Figure 1.1: G4 schematic view: a) G4 tetrad, composed of four guanines held together by Hoogsteen hydrogen bonds and a central cation. b) Lateral and c) top view of G4. In each plane, the guanines making up the tetrad are coloured differently.

At the end of the 80s, it was revealed that guanine-rich telomere sequences spontaneously formed G4 structures *in vitro* under physiological conditions [12–14]. However, only in the twenty-first century, thanks to the use of G4-targeting antibodies [15–19], they were first observed in cells. Since their first appearance, many G4 structures have been resolved, and X-ray crystallography and NMR spectroscopy have offered insights into their topology characterisation with the main focus on the human telomeric or promoter sequences [20–23]. In order to predict potential G4 structures in the genome, algorithms employing sequence motifs like $G_{\geq 3}N_xG_{\geq 3}N_xG_{\geq 3}N_xG_{\geq 3}$ were designed and implemented based on biophysical investigations and employing on various G4 structures [4, 24]. For the first models, the necessary requisite was to have four continuous stretches of guanines and at most seven nucleotides long loops. As a result of the observation of many G4s with different properties, like longer loops and discontinuities in G-stretches causing bulges [25, 26], new predictive models were developed. Later, machine learning came to the aid on the G4 prediction formation thanks to the recent availability of massive experimental datasets on G4s [27].

1.3 Topology and structure

One, two, or four distinct strands of DNA (or RNA) can be combined to produce quadruplexes, which can be unimolecular or intermolecular. G4s can have a wide range of topologies due to the many possible combinations of strand direction, loop size, and sequence. As said before, they are composed of a core of at least two stacked G-tetrads that are joined by loops made of mixed-sequence nucleotides. Many factors affect the G4 arrangement: type of monovalent ion, pH, concentration, molecular crowding, temperature, and other environmental conditions. It was experimentally found that a variety of G4 structures can form [3]. Propeller-like loops result from adjacent linked parallel strands and bridge the bottom G-tetrad with the top G-tetrad, giving rise to the G4 topology usually known as "parallel". Along with the propeller, also the lateral and the diagonal loops are present in G4s, the former connecting adjacent G-strands, while the latter the opposite G-tetrads. Lateral and diagonal loops are present in the G4 topologies called "antiparallel" and "hybrid". Even if it is a simplified view, it is often convenient to divide the G4s into these three mentioned families: parallel (↑↑↑↑), antiparallel (↑↓↑↓), and hybrid (↑↑↓↑ or ↑↓↑↑), each arrow indicates the phosphodiester backbone direction from 5' to 3'. A schematic cartoon of the three G4 topologies and the corresponding loops is present in figure 1.2.

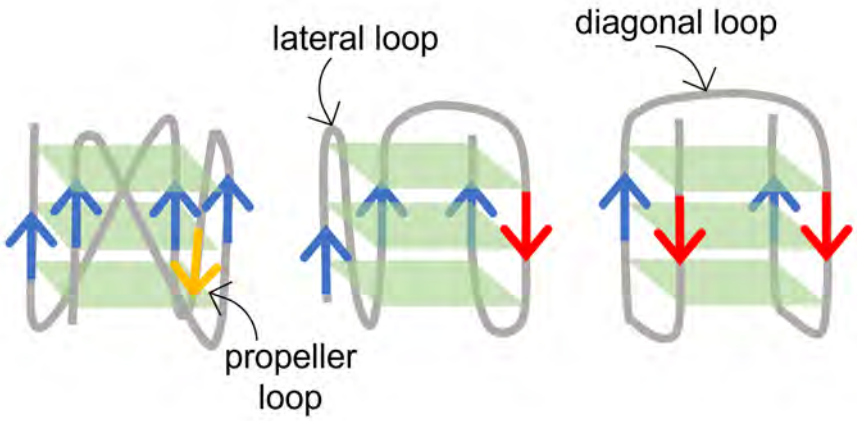

Figure 1.2: Cartoon of the parallel, hybrid, and antiparallel topologies and of the propeller, lateral, and diagonal loops.

Four grooves, which are the cavities delimited by the phosphodiester backbones, are present in all quadruplex structures. Variable groove dimensions, such

as narrow, medium, and wide, are determined by the overall topology and the type of loops. The depth of the grooves is the result of different orientations of the glycosidic bond. The glycosidic bond angle (GBA) χ can be in two diverse conformations (see figure 1.3): *syn* when $-90° < \chi < 90°$ or *anti* when $90° < \chi < 180°$.

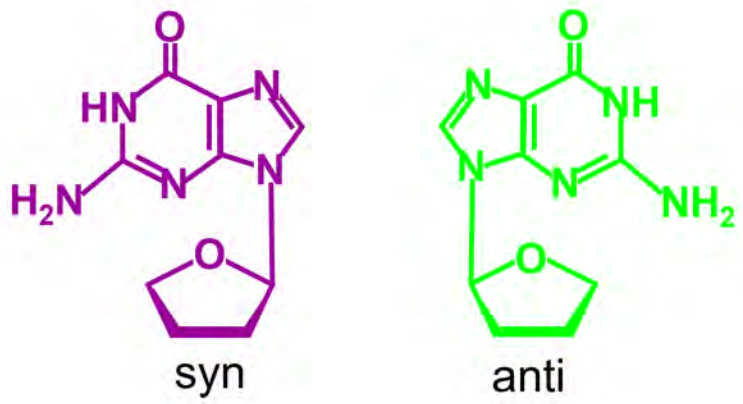

Figure 1.3: Chemical structure of *syn* and *anti* glycosidic bond angles.

Since guanine segments provide the possibility for a wide range of different hydrogen bond alignments, a more specific classification is needed to describe the G4 structural diversity. The Webba da Silva group suggested a new exhaustive description including the number of guanines in the stem, the kind of loops connecting the G-tracts, and the GBA relative to the starting nucleotide closest to the 5' end [3, 28, 29]. The types of loops are identified with their initials "p,l,d" (propeller, lateral, and diagonal) and a +/- is placed before the initial, + (-) indicates clockwise (anti-clockwise) direction with respect to 5' end. The latter is the most common in G4s. For even greater specificity, an additional description can be provided for lateral loops. After the letter l the subscripts m, n or w can be added to indicate the grooves type (medium, narrow, wide).

To better explain this nomenclature, two examples follow. Figure 1.4 shows the schematic cartoon of the 22 bases human telomeric G4 in two different conformations. On the left the representation of the 1KF1 structure, which is a $-p-p-p$, and on the right the 143D one, which is $+l_w d-l_n$. When compared to the common description, it is obvious how effective this naming approach is to describe the several possible G4 structure combination; however, for the sake of simplicity, the expression parallel, antiparallel, and hybrid will often be used in this work.

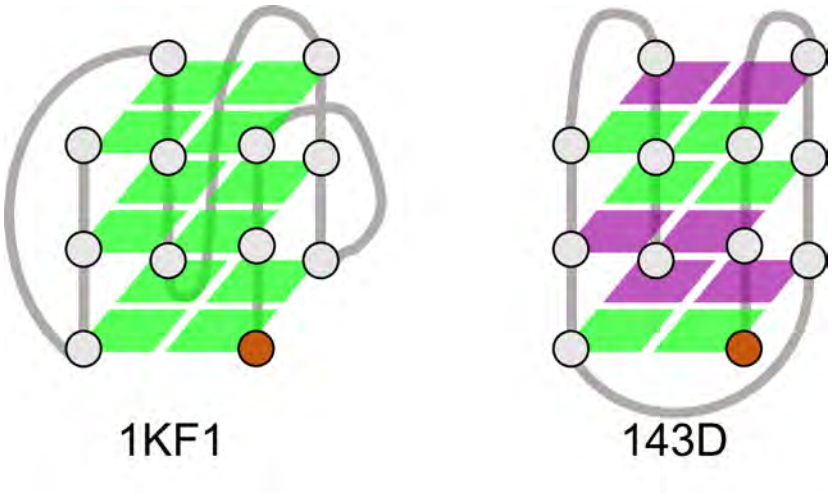

Figure 1.4: Schematic representation of the folded structures of Tel22 in two different topologies. The green and purple squares represent the guanine bases in the corresponding *anti* and *syn* conformations, respectively. The red circle is the reference starting point.

1.4 G-quadruplex applications

G4s are extensively studied and can have several applications, from the development of new nanodevices to the medical-pharmaceutical field. From the biological point of view, more than 400000 G4s have been predicted in the human genome [30]. Their location is often related to cancer biology and genome activities like transcription, replication, genome stability, and epigenetic regulation [31, 32]. Usually, they are found in telomeres, promoter regions, 5'-UTR and 3'-UTR, ribosome binding sites, and in long non-coding RNA. From the beginning, many efforts were made to study telomeric G4s. It is well known that in the terminal part of chromosomes the telomeres are composed of single-strand DNA rich in guanines and it was demonstrated that G4 formation can occur in these regions [14]. The stabilisation of the G4 structure can block the activity of the telomerase [33]. This enzyme, which is present in stem cells but not in the somatic ones, is in 85% of tumour cells and it elongates the telomeres when they are cut during each cell division, giving cancer cells an infinite lifespan [34, 35]. A stable G4 can inhibit the telomerase action and make cancer cells no longer immortal.

Many investigations are related to the use of G4 as a new and promising anticancer target. Moreover, G4s are present in the promoter of oncogenes and it seems that they are a key regulatory checkpoint [36]. In fact, in the literature,

there are examples where the G4 acts as a transcription repressor [37–41]. Clearly, also in this context, the anti-cancer application of this non-canonical DNA comes to light, not only because the G4 alters the transcription, but also because it is present in 67% of genes involved in cancer.

In addition to their biological role, G4s can have many applications in therapeutics and nanotechnology fields. In fact, they have also entered clinical use as aptamers [42], which are short oligonucleotides employed as medicines that bind to certain biological targets to carry out their tasks. G4 aptamers are now being developed for a range of human ailments, including inflammatory diseases, prion diseases, and thyroid disorders. G4 aptamers can function as anticoagulant, anticancer, antiviral, antibacterial, and antifungal drugs. In 1910 it was observed that concentrated guanosine in monophosphate solutions were able to form "gels" [43]. Now we know that it was the first identification of G4-wires, which are lengthy stacking interactions of hundreds of G-tetrad units. G4-wires are now being evaluated for their usage in nanoelectronics applications due to their substantial π overlap, structural rigidity, and guanine low ionisation potential [44]. Due to its high polymorphism and, in some cases, the ability to control topology switching or structure formation and destruction, G4 is considered a new possible component of nanodevices, as biosensor logic gates [45, 46].

1.5 Human telomeric G-quadruplex

Telomeres are guanine-rich sequences made up of tandem DNA motif d(TTAGGG) [47] and G4 can occur in their terminal 150-250 nucleotides where DNA is in single-stranded form [12]. Since the telomeric quadruplex could be used as a future target for cancer therapeutics, the human telomeric sequence $AG_3(TTAG_3)_3$ (Tel22) has gained a lot of attention in the past decades. Due to its polymorphic nature and propensity to switch from one conformation to another when placed in different experimental conditions, its structure in physiological conditions is still an open question. In 1993 Wang and Patel solved the nuclear magnetic resonance (NMR) solution structure in Na^+ environment and in those conditions the Tel22 is in the antiparallel topology [48]; in figure 1.5 its PDB.

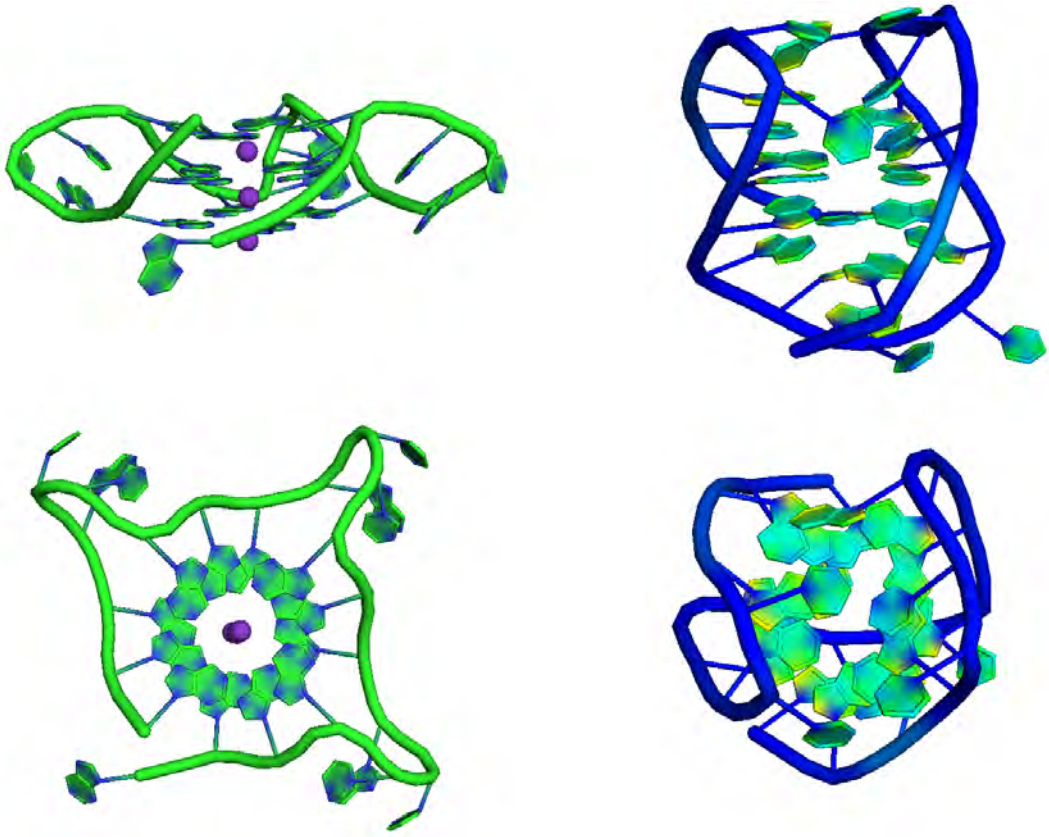

Figure 1.5: Cartoon representation of the PDB structures of Tel22 with different cations. On the left: Tel22 crystal structure in K^+, PDB 1KF1 [20]. On the right: Tel22 NMR structure in Na^+, PDB 143D [48].

After almost ten years, the crystal structure in K^+ was solved by Parkinson et al. [20] and, in this case, the same sequence is in a parallel topology, shown in figure 1.5. Even if the two techniques investigate two different conditions and DNA concentration, this result was unexpected and has brought attention to Tel22 conformation in the K^+ solution. As a matter of fact, gaining knowledge of the Tel22 structure under physiological conditions is relevant for G4 drug design. For this purpose, circular dichroism and NMR are remarkably sensitive to investigate the G4 conformational topologies in solution. Ambrus et al. revealed that the polymorphism of the human telomeric sequence is not just the effects of the two cations but it is also related to the DNA environmental conditions. In fact, the Tel22 in K^+ solution is in a hybrid-type mixed parallel/antiparallel-stranded structure [21, 49, 50] while, as said before, its crystal structure is in the parallel configuration. They also investigated the effect of the addition of potassium ion on the G4 structure in sodium, discovering that even small quantities of K^+

lead to conformational rearrangement and, thus, shift toward the hybrid topology. Surprisingly, the Tel22 topology in K^+ is also affected by changing the DNA concentration: circular dichroism showed the propensity to switch from hybrid to parallel conformation as concentration increases from $\sim$ 40 μM to 4.5 mM [51]. However, not all telomere topologies are biologically significant and some factors can alter the predominant conformation in physiological conditions such as crystal packing, dehydration, crowding, and non-physiological cation. In 2019 using ^{19}F-NMR technology to monitor the folding of Tel22 in HeLa cells, it was discovered that just the hybrid conformations occur [52]. For this reason, studying DNA in hybrid configurations is also relevant to mimic *in-vivo* conditions.

1.6 Interaction with small molecules

Since G4 has been proposed as a powerful target for anticancer therapeutics and for many other clinical applications, many efforts have been made to optimise the performances of the binders according to their use. The G-Quadruplex Ligands Database now has about 1000 small compounds that target G4 structures [53]. Small molecule G4 binders often contain similar features, such as a steric bulk to prevent intercalation with double-stranded DNA, an aromatic surface for π-stacking on the top of G4s, or a positive charge to interact with the loops [54]. However, the rational design of new G4 ligands is not easy and can be challenging due to its intrinsic polymorphic nature. In principle, the ligands must have a strong G4 affinity but also to be selective as compared to the duplex DNA and, nowadays, more G4 topology specificity is requested to optimise the quadruplex functions. Despite a huge literature on the development of new G4 binders and many ligands have been shown to inhibit the telomerase action [55–58], a molecule able to pass all the clinical trials and to be used for therapeutic applications has not yet been identified due to the poor drug-like properties. Quarfloxin, for instance, did not proceed with phase III [59], despite having completed phase II [60] as a prospective therapeutic treatment against various malignancies due to its strong albumin binding. The next steps will be to find ligands able to target just specific G4 topologies and to improve pharmacokinetic properties.

1.7 Photosensitive ligands and light stimuli

It has been demonstrated that a wide variety of small-molecule ligands bind with G4s, causing significant modifications to the DNA folding topology or even its unfolding. The goal is to find a ligand, an external agent capable of modifying the properties of the G4 but not interfering with the environment. Several external stimuli were used to regulate material reactions, including temperature, pH, electrical field strength, and molecular recognition. The external trigger for biological processes with the higher potential is likely photo-irradiation. In fact, in contrast to the irreversible addition of chemical stimuli, which tends to build up, irradiation generally does not contaminate the system, making it a traceless technique once irradiation has stopped. For this reason, in this thesis, it was decided to employ photosensitive ligands and light stimuli to trigger DNA conformational changes. As a spatio-temporally controllable non-invasive tool for biological applications, light presents unmatched perspectives. To date, the requirement to induce switching with UV light, which is frequently harmful and penetrates most milieux only partially, restrains the development of effective photodynamic systems in significant ways. Many efforts have been made in a variety of fields to individuate natural compounds or to create artificial photosensitive systems that react predominantly to visible and near-infrared light (400-1000 nm).

In this work, the irradiation effects on Tel22 upon complexation with two relevant photosensitive ligands were studied. The former is the TMPyP4 porphyrin, which is able to downregulate the expression of genes by quadruplex formation in the promoter region. Porphyrins produce singlet oxygen ($^1O_2$) when exposed to radiation, a feature that is frequently employed in photodynamic therapy. In particular, it has recently been demonstrated that singlets preferentially oxidise guanines at the exterior faces when interacting with G4s, producing a large number of radicals. The latter is a recently synthesised pyridinium-decorated dithienylethene (DTE) ligand, which has been shown to selectively target G4 with discrimination against duplex DNA, and to produce reversible photo-switching between the open (1o) and closed (1c) isomers by alternating blue/red visible light exposure [61].

Chapter 2:

Materials and methods

2.1 Introduction

In this chapter, the fundamental principles and methods adopted in this work are briefly explained. Contextually, the environmental conditions of each experiment are described. It is worth mentioning that in potassium environment the human telomeric Tel22, due to its high polymorphic propensity, and its heterogeneity in solution, is difficult to characterise. As evidence of this, the reported NMR measurements in the literature show guanine imino spectral overlap with the consequent impossibility of resolving the structure. The lack of information on structural characterisation is a huge limitation in developing new selective anticancer drugs. In this context, this work has the aim of providing a methodology to investigate G4 conformational changes and drug interaction employing a multi-scale approach combining in-house techniques such as UV-Vis absorption, circular dichroism and fluorescence with UV resonant Raman spectroscopy and small-angle neutron/X-ray scattering available at the large scale facilities.
This chapter is based on few extensive reviews [62–73].

2.2 UV-Visible absorption spectroscopy

One of the most common techniques for sample characterisation in material science is UV-Vis absorption (ABS) spectroscopy. ABS is helpful for investigating the electronic properties of materials and biological samples. It measures the attenuation of a beam of light after it passes through a sample, the absorbance

A is defined as the logarithm of the reciprocal of the transmittance T:

$$A = -\log(T) = \log(\frac{I_0}{I}) \tag{2.1}$$

where I_0 and I are the incident and the transmitted intensity, respectively. Assuming that there is a linear relationship between the absorber concentration and the absorbance, ABS is used to get quantitative information on the sample concentration through the Beer-Lambert law:

$$A = lc\epsilon \tag{2.2}$$

where l is the path length, c is the absorbing species concentration, and ϵ is the extinction coefficient, a measure of the degree of light absorbance of a chemical species at a specific wavelength.

Therefore, UV-Vis absorption was employed not only for estimating G4 and ligands concentration but also to get information on the DNA-drug interaction. Indeed, the G4 binders usually have an absorption peak far from that of the G4s (260 nm) and, by monitoring their intensity changes and their peak shifts during a titration experiment, it is possible to estimate the number of binding sites and, sometimes, also the kind of interaction and the binding constant. UV-Vis absorption measurements were performed using a Jasco V-570 Spectrophotometer, with a quartz cuvette path length of 1 mm. The UV-Vis investigated spectral range was from 190 to 800 nm.

2.3 Circular Dichroism spectroscopy

Circular Dichroism (CD) is a really useful tool for investigating the secondary structure conformational changes of proteins and nucleic acids. It provides a method for determining the effect of a mutation or a change of environment (temperature, pH, ionic strength) on the overall molecular structure. Moreover, it is widely used because it needs only small amounts of samples and it does not damage them. CD signal is not produced by all the molecules, but just from those that are optically active. For this purpose, an important property is the

rotational strength (R_{oa}) defined as follows:

$$R_{oa} = \mu_e \cdot \mu_m \tag{2.3}$$

where μ_e is the electronic dipole moment and μ_m is the magnetic moment. The R_{oa} is the imaginary part of the scalar product of the electric dipole and the magnetic dipole induced by the light. A molecule is optically active if the rotational strength is different to zero. If a molecule has a plane or centre of symmetry, the rotational strength is zero and there is no optical activity. Instead, when the magnetic and electric fields are not orthogonal, the molecule is optically active, and it happens when there is an asymmetry in the system. Substances are optically active when they rotate the plane of polarisation of a beam of light passing through it. Chiral molecules have covalent bonds that cannot be superimposed on their mirror images and they are optically active. CD is a light absorption spectroscopy, which measures the difference in absorption of left-handed and right-handed circularly polarised light:

$$CD = \Delta A = A_l - A_r = lc\epsilon_L - lc\epsilon_R = lc\Delta\epsilon \tag{2.4}$$

where l is the path length, c is the absorbing species concentration, and ϵ is the extinction coefficient.

2.3.1 Circular Dichroism of G-quadruplexes

Chromophores are the functional groups in molecules that absorb light and produce electronic transitions. The amide group and some groups in the aromatic amino acids are the chromophores of proteins, while the nucleobases are those of oligonucleotides. These moieties are the ones that produce a CD signal. In particular, guanine possesses two absorption bands in the 240–290 nm region, which are connected to two $\pi \rightarrow \pi^*$ transitions at about 279 and 248 nm [74, 75]. In G4s the G-tetrads are stacked on top of the other and turned one with respect to the adjacent. This rotation generates the chiral exciton coupling between transition dipole moments of guanines. This effect is generated by two or more chromophores that are chirally oriented [76] and gives rise to two bands with opposite signs, where the wavelength of the zero CD signal corresponds to the one where there is the maximum in the absorption spectra. The G4 CD

signal strongly depends on the exciton coupling that is generated by the orientation of the glycosidic bonds (*syn* and *anti*), which change the overlapping of molecular orbitals. The different combinations of *syn*/*anti* configurations give rise to different G4 topologies. This is the reason why CD is so sensitive to G4 secondary structure changes. In a three-tetrad G4 system, the number of possible G-tetrad glycosidic bond and the loop combinations makes 32 possible configurations but, to simplify, they can be grouped into three main topology families: parallel, antiparallel, hybrid. Chaires' group created a library of CD spectra of 23 well-characterised G4s with a known structure [77], most of them can be placed into these three secondary structure topologies. As a rule of thumb, they can be distinguished by their maximum and minimum, the parallel maximum is at ~ 260 nm and the minimum at 245 nm, while the antiparallel has two maxima at ~ 295 nm and 245 nm and a minimum at 260 nm, lastly the hybrid with maxima at 295 nm and 260 nm and minimum at 245 nm. Figure 2.1 shows the CD signature of these three configurations: spectra are obtained by averaging the 23 CD signals forming the library [77].

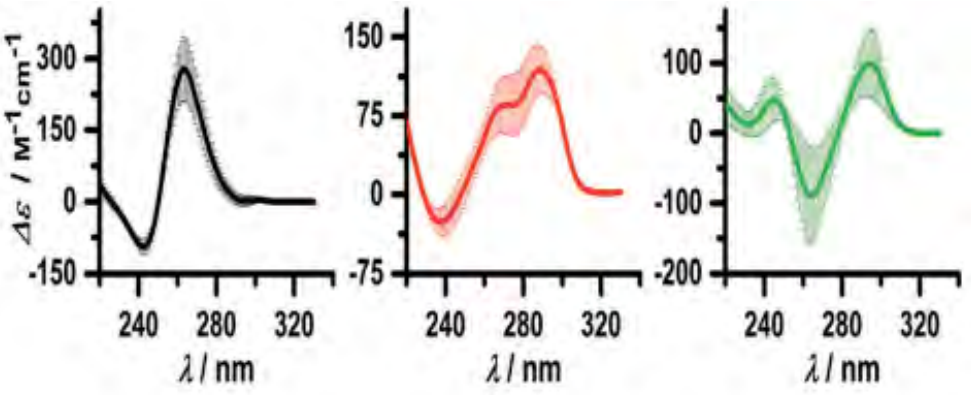

Figure 2.1: Average CD spectra of the three main topology families. In black the parallel group, in red the hybrid, and in green the antiparallel. Figure taken from [77].

2.3.2 Spectropolarimeter Jasco J-810

Circular Dichroism experiments were carried out with a Jasco J-810 spectropolarimeter. When it is not specified, to achieve the best signal to noise ratio, a 1 mm path-length quartz cuvette was employed with tens of micromolar of DNA concentration. The CD experiments of chapter 6 were carried out by utilising a 0.1 mm path-length quartz cuvette and a DNA concentration of hundreds of

micromolar. For Tel22 the investigated CD range was between 220 nm to 350 nm, sometimes extended up to 500 nm to look at the induced CD spectra of the ligands, and the scan speed was set at 50 nm/min. The melting experiments were achieved through a thermal bath.

The schematic view of the spectropolarimeter Jasco J-810 is shown in figure 2.2. The light, emitted from a xenon lamp, is converged by the M1 mirror into the S1 entrance slit, and then there is the optical system related to the first monochromator, whereas the second monochromator is related to the optical system between the S2 intermediate slit and the S3 exit slit. A double monochromator ability to reduce stray light is essential for CD measurements. The instrument employs crystal prisms (P1 and P2) with different axial orientations, to produce a monochromatic and also linearly polarised light that oscillates in the horizontal direction. The modulator converts from linear polarised light into right and left circularly polarised beams of light, which pass through the shutter (SH) to the sample compartment. After the interaction with the sample, the light is detected by the photomultiplier (PM).

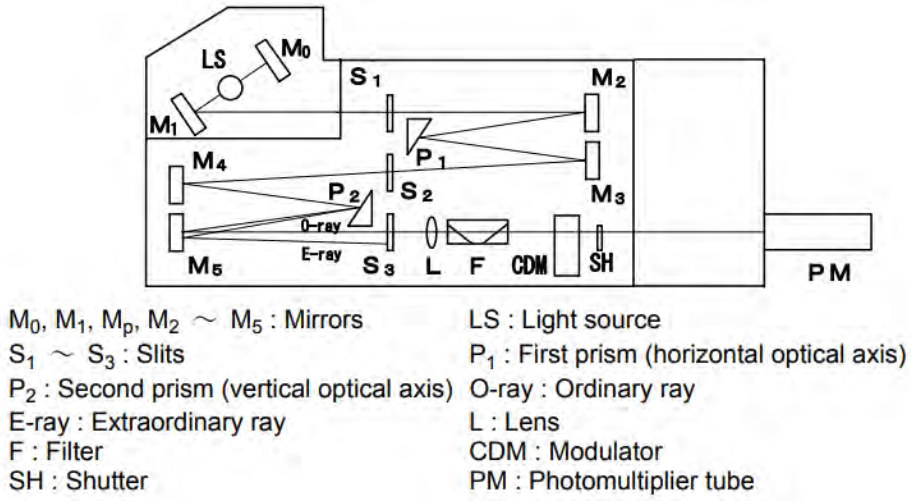

Figure 2.2: Block diagram of the optical system of spectropolarimeter Jasco J-810. The figure is taken from J-810 Series Hardware Function Manual.

2.4 Fluorescence spectroscopy

Fluorescence (FLUO) is the ability of some atoms and molecules to absorb light at a specific wavelength and then to emit light at a longer wavelength after a

short interval; the typical emission rate is 10^8 s^{-1} [62]. The fluorescence process can be divided into three main steps: first, the molecule excitation by an incident photon that happens in the femtosecond timescale, then, there is the vibrational relaxation of the excited electron to a lower energy level (10^{-9} s), and, at the end, a photon with a longer wavelength is emitted and the electron returns to the ground state (10^{-12} s). The Jablonsky diagram, shown in figure 2.3, schematises the process that takes place between the absorption and the emission.

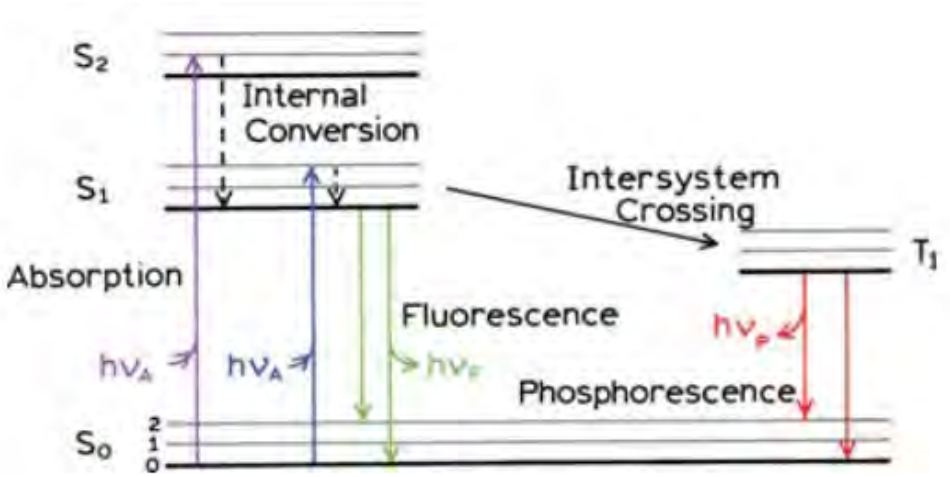

Figure 2.3: Schematic of Jablonski diagram. Figure taken from [62].

Fluorescence spectroscopy measurements were carried out using a homemade apparatus located at the Physics Department of Sapienza University of Rome. The sample was excited with the 365 nm pulses of an Ekspla NT340 laser (repetition rate 10 Hz, 5 ns pulse duration). The laser power was kept below 5 mW to minimise photo-bleaching effects. The fluorescence emission was collected at an angle of 90° with respect to the excitation beam and delivered to a f=3.2 Czerny Turner spectrograph (Horiba Ltd) equipped with a 600 gr/mm diffraction grating, ensuring a spectral resolution better than 1 nm. The dispersed fluorescence light was detected by a CCD. The spectra were processed and analysed using LabSpec 6, Origin 9, and Matlab softwares.

2.5 UV Resonant Raman spectroscopy

Raman spectroscopy is a well-established technique to investigate the chemical-physical properties of matter. In particular, it probes the intramolecular and in-

termolecular vibrational modes, which can be used as markers of chemical bonds. It is based on the inelastic scattering of electromagnetic radiation with the target and, in conventional Raman experiments, the radiation source is typically in the visible region, to avoid damage of biological samples. Conversely, UV Resonant Raman (UVRR) spectroscopy exploits UV light as an exciting wavelength, which matches the absorption band maximum of chromophores in biological samples. If the excitation wavelength corresponds to an absorption band for a specific vibronic, the Raman intensity for that transition is greatly enhanced. In conventional Raman process, the molecule goes to an unstable and virtual excited state, while UVRR promotes to a real vibronic excited state, therefore the cross-section of these events can be 10^3 times higher. This property allows to measure samples in very diluted conditions, down to 10^{-8} M [66]. Moreover, the contribution from different chromophores is less overlapped in UVRR spectra than in the conventional Raman, and this is ascribable to the selective magnification of specific signals associated with the chromophores excited. Nevertheless, self-absorption is a UVRR limitation, since it can reduce the total scattered light, influencing the relative Raman intensity. Photo-degradation of the sample can be avoided by spinning systems that continuously agitate the sample.

2.5.1 UVRR on nucleobases

DNA absorption depends on its nucleobases, in figure 2.4 it is shown the absorption signal of salmon sperm DNA and the deoxynucleotide triphosphates dATP, dCTP, dGTP, and dTTP. Human telomeric G4s are mainly composed of guanines, and the dG absorption depends on two principal electron transitions, one that involves the N7=C8 site (centred at 255 nm) and another related to the C2=N3–C4=C5–N7=C8 group (centred at 275 nm) [78]. The absorption spectrum of the other deoxynucleotides are quite different: adenine shows a maximum located at $\sim$ 260 nm, thymine at 266 nm, while cytosine at $\sim$ 275 nm with a shoulder at $\sim$ 230 nm [78].

Due to the relatively varied UV absorbance pattern that nucleotides display, one can enhance the contributions made by individual bases in the DNA UVRR spectrum by carefully selecting the excitation wavelength in accordance with the electronic transitions of certain nucleobases. Figure 2.5 shows the UVRR spectra of salmon sperm DNA obtained with different excitation wavelengths.

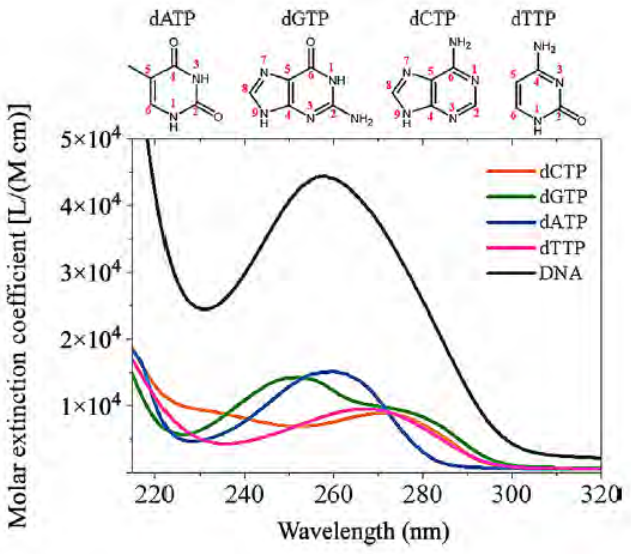

Figure 2.4: UV absorption spectra of salmon sperm DNA (black) and deoxynucleotide triphosphates dGTP (green), dATP (blue), dTTP (pink), and dCTP (orange). Top panel: chemical structures of nucleotides. Figure taken from [66].

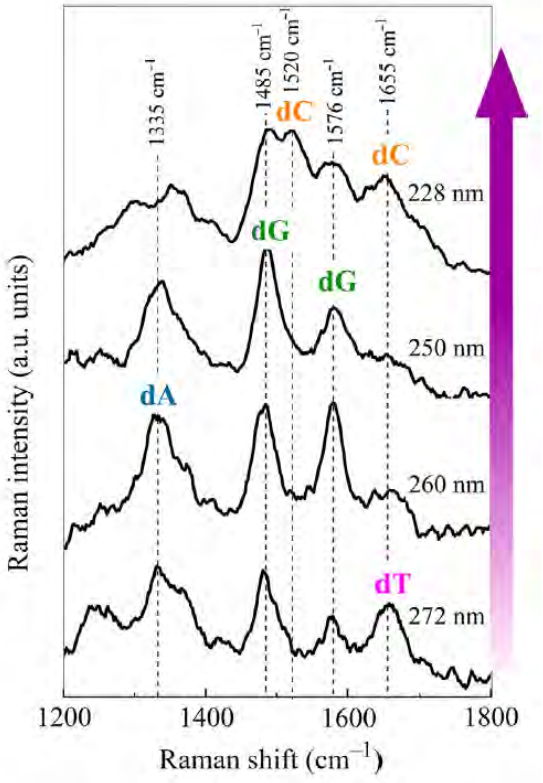

Figure 2.5: UVRR spectra of salmon sperm DNA at different excitation wavelengths (228, 250, 260, and 272 nm). Figure taken from [66].

It is worth noting that the 250 nm-excited UVRR signal is mainly related to the in-plane vibrational mode at 1485 cm^{-1} (bending of C8–H and stretching of C8=N7 and N9–C8 [79]) and at 1576 cm^{-1}. It is possible to use UVRR spectroscopy to gain molecular insights into the conformational modifications that take place when G4 interacts with small molecules. The peak shifts give information on the modification of bond strength, while the intensity increase/decrease can be related to the binding mode. For example, a hypochromic effect indicates a more compact G4 structure, likely induced by end-staking upon the external G-tetrads. Instead, intercalation promotes a hyperchromic effect [79]. Moreover, this effect can also be associated with an unstacking of the G-tetrads due to unfolding.

2.5.2 IUVS beamline

UVRR measurements were performed at the IUVS beamline at Elettra Sincrotrone (Trieste) supported by a synchrotron-based set-up [66]. Samples were placed into a 10 mm path quartz cuvette. Depending on the experiment, the excitation wavelength was set at 220, 250, and 266 nm. The spectral resolution was $\sim$ 2.6-5 cm^{-1}/pixel. The beam power measured on the samples was set from 4 to 400 μW to optimise the better signal-to-noise conditions and, to prevent any possible sample damage caused by prolonged UV exposure, continuous stirring was employed. Tunable UV synchrotron radiation permits to map the whole resonances of the sample.

Following, a brief description of the IUVS set-up is reported. The beamline is made up of two separate branch lines, one for UV Brillouin scattering and one for Raman scattering (shown in figure 2.6). The 32 mm undulator provides photons in the tunable range of 5-11 eV (λ between $\sim$ 113 nm and 280 nm), and the higher order harmonics of the undulator are cut through two mirrors. Then, 5 degree grazing incidence silicon mirror acts to deviate the beam into the two different set-ups. For UVRR, the beam is in the 200-280 nm range with a bandwidth of 50 nm, which has to be monochromatised. The beam is brought inside a 750 nm Czerny-Turner spectrometer furnished with three holographic UV-optimised gratings of 1800 g/mm, 2400 g/mm, and 3600 g/mm, allowing a final bandwidth of 10 cm^{-1}. After the monochromator, a spherical lens collimates the beam, which is brought to the sample for Raman scattering. A spherical lens with a diameter

of 5.08 cm and a focal length of 100 mm serves as the focusing and collecting lens, resulting in a backscattering configuration. The analyser system is made of three interconnected Czerny-Turner spectrometers with different focal lengths, which are able to increase the resolution, reduce the elastic component, and measure Raman peaks up to ≈ 50 cm^{-1}. The information on the experimental apparatus was taken from the instrument website (www.elettra.eu).

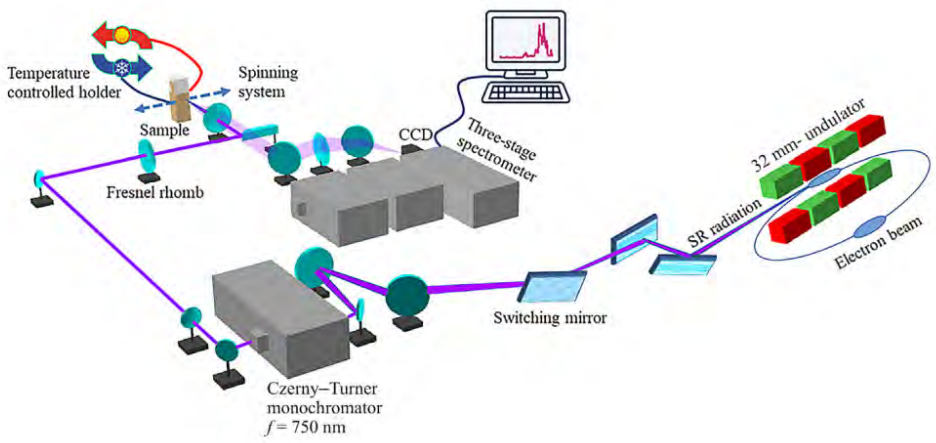

Figure 2.6: Overview of the IUVS UVRR set-up.

2.6 Small-angle scattering

Small-angle scattering (SAS) is a low-resolution technique that cannot resolve atomic dimensions but gives useful information on the shape and size of biological samples. This scattering method describes the nano-scale size range, which can be extended from Angstrom to micrometer. The SAS resolution depends on the smallest angle for which data can be measured, that value is strictly related to the longest distance that can be observed. An advantage over high-resolution techniques is that small amount of sample is needed and it can be measured near physiological conditions, in solution, without sample crystallisation. In the case of Tel22, SAS methods can make the difference, since it has been shown in the previous chapter that the human telomeric G4 is highly polymorphic and its structure is strongly environmentally sensitive. Moreover, this technique permits to analyse the structural conformational changes induced by external stimuli and the construction of 3D structural models from the one-dimensional SAS profile.

SAS takes advantage of the wave nature of X-rays and neutrons, which can be described starting from the wavelength and the amplitude. In X-rays the wavelength can be obtained from $\lambda = 1.256/E$ where E is the photon energy, while for neutrons the de Broglie equation is used where $\lambda = 396.6/v$, with v the (group) velocity of neutrons. When X-rays/neutrons reach the sample, they interact with electrons/nuclei of the atoms, which generate secondary waves. Then, coherent scattering can interfere in a constructive or destructive way.

The main parameter that describes the SAS method is the scattering vector or momentum transfer:

$$Q = \frac{4\pi \sin\theta}{\lambda} \tag{2.5}$$

where θ is the half angle between the incident and the scattered wave and λ is the incident radiation wavelength. The scattering intensity as a function of the momentum transfer can be described as follows:

$$I(Q) = \langle \int \mid (\rho(\vec{r}) - \bar{\rho}_s) e^{-i\vec{Q}\cdot\vec{r}} d\vec{r} \mid^2 \rangle \tag{2.6}$$

where $\rho(\vec{r})$ is the scattering density of the particle at position r, $\bar{\rho}_s$ is the solvent scattering density and their difference ($\Delta\rho$) is called contrast. Usually, the Fourier transform of the scattering intensity, the pair distance distribution $P(r)$, is used to get information on the particle structure and shape. Figure 2.7 illustrates a few examples. $P(r)$ represents the distribution of distances between pairs of particles contained within a given volume, it vanishes at $r = 0$ and at $r = D_{max}$, which is the maximum linear dimension. To have good information on the longest distances, data have to be also acquired at $Q < \pi/D_{max}$. Other two parameters related to the shape and the size of the scattering particle are the radius of gyration (R_g) and the forward scattering intensity $I(0)$. The latter parameter can be estimated from extrapolation and it is also related to other quantities:

$$I(0) = \frac{C\Delta\rho^2 C v^2 M_w}{N_a} \tag{2.7}$$

where C is the mass per unit volume, $\Delta\rho$ the contrast, v the specific volume, M_w the molecular weight, and N_a the number of Avogadro. R_g is a measure of the overall size of the macromolecule, it is defined as the average square centre of mass distances in the particle weighted by the scattering density. R_g can be estimated from the Guinier approximation, which is valid when $QR_g < \frac{1}{3}$ for

globular particles, while the upper limit is smaller for extended shapes. The Guinier equation is the following:

$$I(Q) = I(0)e^{\frac{-Q^2R_g^2}{3}} \tag{2.8}$$

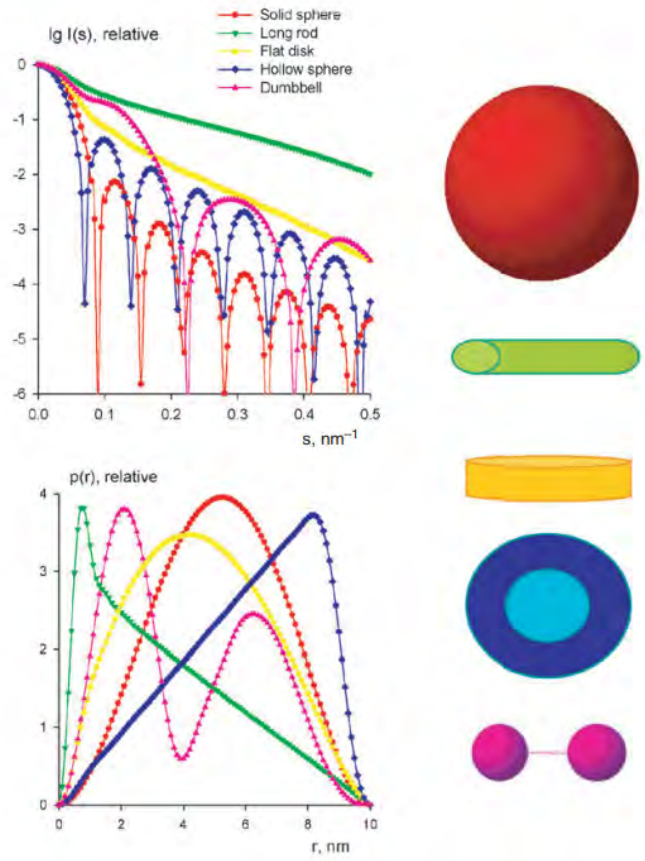

Figure 2.7: Scattering intensities and $P(r)$ of geometrical objects, where s is the scattering vector. Figure taken from [80].

To check the internal consistency and robustness of the data, R_g and $I(0)$ can be extrapolated also from the $P(r)$:

$$R_g^2 = \frac{\int r^2 P(r)dr}{2\int P(r)dr} \tag{2.9}$$

$$I(0) = 4\pi \int_0^{D_{max}} P(r)dr \tag{2.10}$$

To assess the degree of unfolding or the flexibility of the samples, the Kratky

plot can be evaluated, where $Q^2I(Q)$ is plotted *vs* Q and, at high Q in the Kratky plot, disordered or flexible molecules exhibit a plateau, while compact/globular samples have a bell-shaped (Gaussian) peak. It can be also used to see if the sample has been subject to radiation damage. Different Kratky plots are shown in figure 2.8.

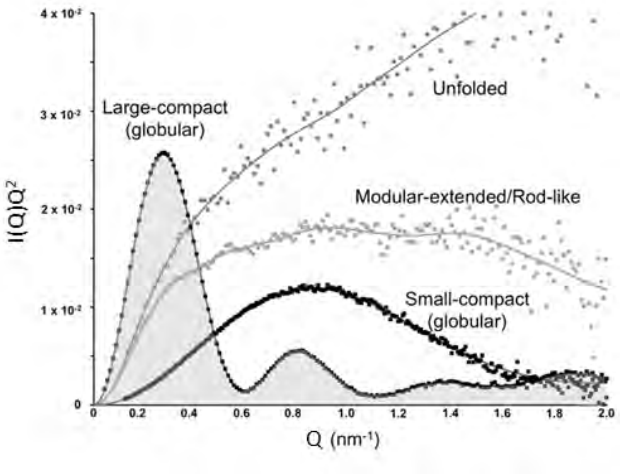

Figure 2.8: Kratky plots from SAXS data of large and small globular, modular-extended/rod-like, and completely unfolded proteins. Figure taken from [81].

SAXS and SANS can be employed as complementary techniques, the former is characterised by a higher flux with a better signal-to-noise ratio, but has the disadvantage that can cause sample radiation damage, while the latter can be used as a control as it does not produce changes in biological systems and, moreover, the contrast can be enhanced through solvent deuteration or deuterium-labelled components of the sample.

2.6.1 D22 beamline

SANS measurements were carried out at the small-angle diffractometer D22 at ILL (Institut Laue-Langevin, France). The experiment was conducted with the incident wavelength of 0.60 ± 0.06 nm with two different sample-detector distances, namely 1.5 m and 5.6 m, allowing a Q 0.1-5 nm^{-1} range. SANS data were reduced using Grasp software (developed by C. Dewhurst), considering transmission and incident flux scaling as well as blocked beam and empty cell subtraction. They were scaled to absolute intensity using direct flux measurement. Data are available here: http://doi.ill.fr/10.5291/ILL-DATA.8-03-980.

D22 was chosen as it has the highest flux at the sample in the 0.45-4 nm wavelength range than any classical constant-wavelength pin-hole small-angle neutron scattering instruments. This is due to the brilliant horizontal cold source, the velocity selector short rotor, its high transmission, and the quite large cross-section of the beam (55 mm x 40 mm). Figure 2.9 shows the D22 set-up, the main components are the velocity selector, the collimation system, the sample holder, and the detection system. The wavelength selector consists of a long rotating drum of 25 cm, with a 28300 rpm highest speed. It is usually used in a 10 % wavelength band, but it can be varied from 8 to 20% resolution. The collimation system is formed by eight sections, each of them composed of three tubes: one is the neutron guide, the second has an antiparasitic aperture, the third is equipped for future set-up. The sample-source distance depends on how many guide sections are used. A remotely controlled XYZ and rotation table, as well as an Eulerian cradle for mounting devices for working in air or vacuum, comprises the sample equipment. The sample-to-detector distances from 1.1 m to 17.6 m can cover a Q range of 0.004 nm^{-1} to 5 nm^{-1}. The detectors are made of 3He and the multidetector area is the largest of any small-angle scattering instrument; with 0.8 cm x 0.8 cm pixels and 16 K resolution, the detection death time is 2 μs. The information on the experimental apparatus was taken from the instrument website https://www.ill.eu/.

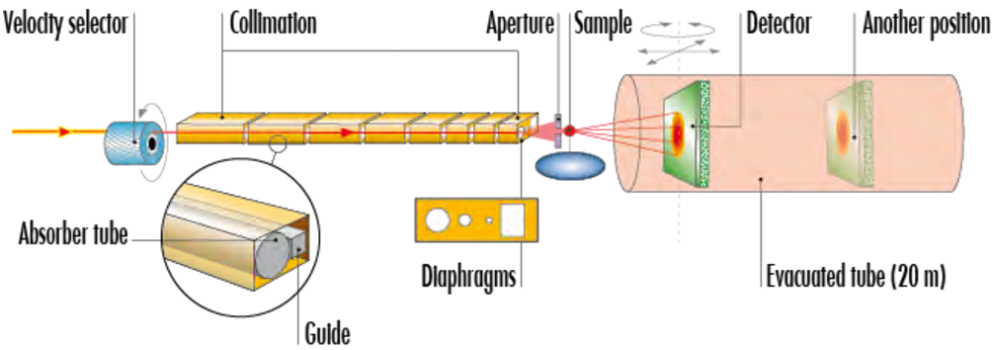

Figure 2.9: Scheme of the small-angle diffractometer D22 set-up.

2.6.2 SWING, BM29, and Austrian SAXS beamlines

SAXS measurements were performed at the SWING beamline at SOLEIL synchrotron (France), at BM29 beamline at ESRF synchrotron (France), and at the Austrian SAXS beamline of Elettra synchrotron (Italy). SAXS instruments have

a similar set-up to that of SANS, composed of a X-ray source, a beam collimation apparatus, a sample holder, a beam stop, and a detection system. Since three different apparatuses were used for SAXS measurements, the main instrument parameters are summarised in the following table:

Table 2.1: SAXS parameters set-up.

	SWING	BM29	Austrian
Energy range (KeV)	5-16	7-15	5.4, 8, 16
Q Range (nm^{-1})	0.007-5	0.025-6	0.045-6
flux (photons/s)	10^{12}-10^{13}	10^{12}-10^{13}	10^{13}

The three beamlines have many components in common, so only BM29 will be described. A schematic view of the apparatus is shown in figure 2.10. It can be divided into three main parts: optics, experimental, and control hutches. First of all, to preserve the monochromator mechanics with the largest beam size that optics can use, primary slits limit the white beam to a size of 4 mm. Then, the beam is cleaned from any parasitic scattering by secondary slits and three axes of white beam attenuators are present to protect the double multilayer monochromator from lower energies. The monochromator, which scatters in the horizontal plane with a spacing of 9 mm between the monochromatic and incident white beams, is an almost fixed exit. The mainly used source energy is 12.5 keV but it can vary between 7 and 8 keV, the resolution $\Delta E/E$ is around 1.6%. The monochromator vessel has a water-cooled beamstop built into it that serves to stop any white beam from the first multilayer from escaping while letting the monochromatic beam pass. The X-ray beam at the monochromator entrance is typically 4 mm x 4 mm. Then, the beam reaches the Rh-coated toroidal mirror that focuses the monochromatic radiation in the detector plane with a spot of 0.5 mm x 0.5 mm. At the beginning of the experimental hutches, the slit blue box for beam cleaning is located. The slits have two pairs of blades composed of Si-crystal layer and they are made of tungsten carbide. The illuminated spot on the sample is defined by guard slits and is typically 0.5 mm x 0.5 mm, producing a 0.2 mm x 0.2 mm beam on the detector plane. Thanks to the flight tube, the beam path from the capillary sample to the detector is conducted in vacuum. At the end a beamstop is placed, composed of a hollow tungsten cylinder with an external diameter of 3 mm, a wall thickness of 1 mm, and an integrated diode with an active size of 1 mm x 1 mm. For each frame that is recorded, a diode

reading and detector count are done. Moreover, in order to check the beam shape, a beam viewer containing a fluorescent screen is placed in the beam and also a diode counts photons. The information on the experimental apparatus was taken from the instrument website https://www.esrf.fr/home.html and from [82].

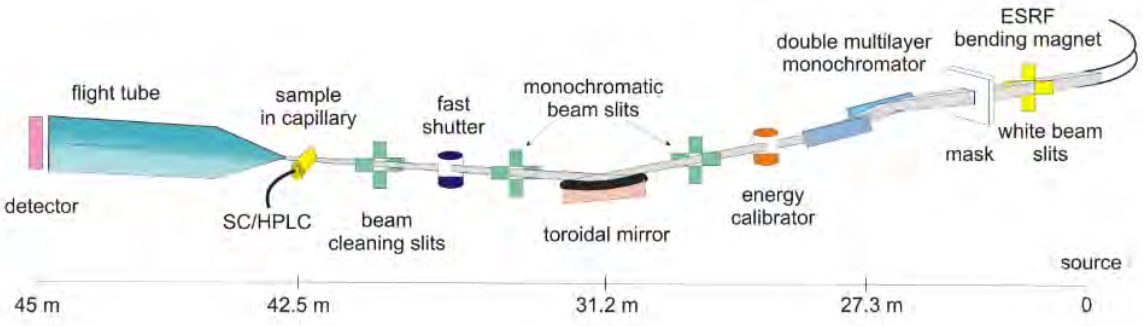

Figure 2.10: Schematic picture of BM29 beamline.

2.7 Singular Value Decomposition

Singular value decomposition (SVD) is a procedure taken from linear algebra that consists of factorising a matrix **D** (m x n with m>n) into the product of three matrices, as follows:

$$\mathbf{D} = \mathbf{USV}^T \tag{2.11}$$

where $\mathbf{V}^T$ is the transpose matrix of **V** (n x n) matrix and **U** is a m × m matrix. **U** and **V** are unitary matrices, composed by orthonormal vectors. **S** is a non-negative diagonal rectangular (m x n) matrix, the elements of which are called singular values (s_i), they are uniquely determined and sorted in decreasing order.[1] The biggest index i such that $s_r > 0$ is the rank of **D**. Therefore, the first r columns of **U** are an orthonormal basis for **D**. Another crucial characteristic of SVD is that each subset made up of the first i components of the **U**, **V** and **S** offers the best i-component approximation to **D** in the least-squares sense. In the analysis of experimental data, the **D** matrix always contains noise and experimental errors, therefore the first n s_i values are unlikely to be null, so

[1]The vectors of **U** are the eigenvectors of $\mathbf{DD}^T$, while the vectors of **V** the eigenvectors of $\mathbf{D}^T\mathbf{D}$. The singular values are the square roots of eigenvalues of $\mathbf{DD}^T$ and $\mathbf{D}^T\mathbf{D}$.

assumptions are needed to find the minimum number of vectors to describe the whole dataset with a good approximation. This aspect is really important since the SVD is applied in various contexts, from statistics and signal processing to psychology. In the context of G4 unfolding, where, in most cases, the melting pathway cannot be described with a two-step model (folded and unfolded), the SVD analysis has the capability to find the least number of states able to describe the whole unfolding process and to obtain thermodynamic information.

The main steps of this analysis will be briefly described taking into account the following scientific literature [67–69]. First of all, the 3D melting curves have to be acquired by recording the whole experimental spectra as a function of temperature. In this work the CD and UVRR data were analysed through SVD but, certainly, also data from other experimental techniques with many other external stimuli can be interpreted with this methodology. Figure 2.11 shows an outline of the data type that is used in SVD analysis.

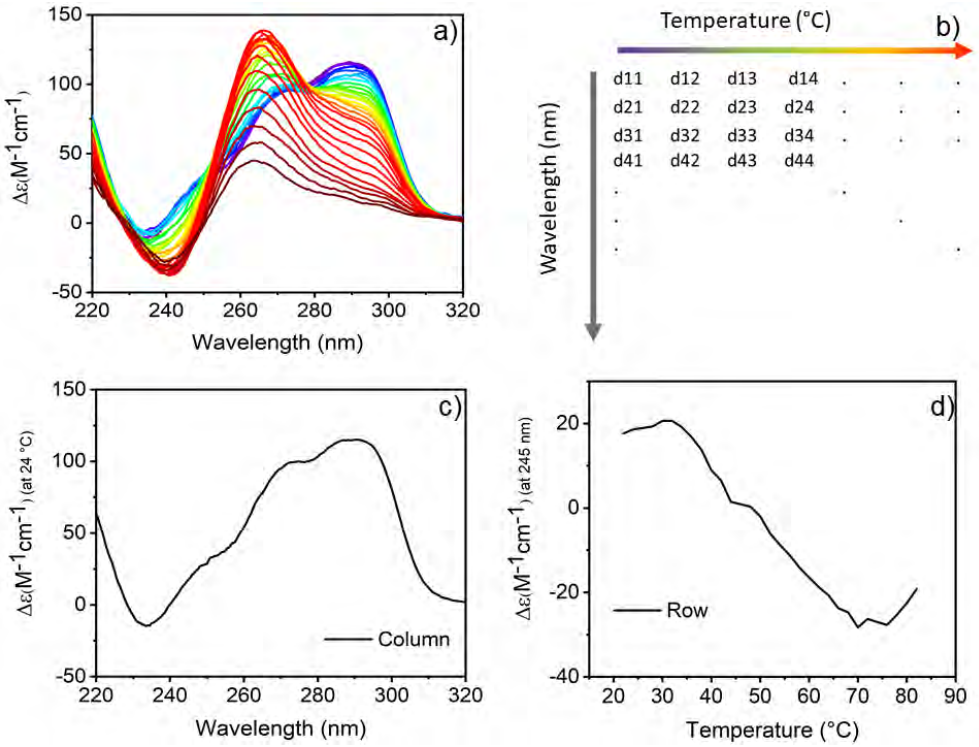

Figure 2.11: Structure of dataset used for SVD analysis. a) CD multidimensional melting data. b) Data matrix structure created from data presented in panel a. c) Column of the data matrix showing the CD spectrum at 24 °C. d) Row of the data matrix showing the CD intensity behaviour as function of temperature at a single wavelength.

In this example, CD data are shown: in the columns CD spectra at each temperature are reported, while the rows show the CD intensity trend at a single wavelength as a function of temperature. The SVD method was applied through an algorithm in Octave [83], which gives as output the three matrices of the decomposition. The basis spectra in the **U** matrix are normalised components with CD spectral shapes, the combination of which forms the family of spectra of starting dataset, while the **V** matrix is made of the amplitude vectors as a function of temperature (or other external variables). The **S** matrix is diagonal and is formed by the singular values representing each component weight.

Figures 2.12 show the first four columns of matrix **U** and of matrix **V**.

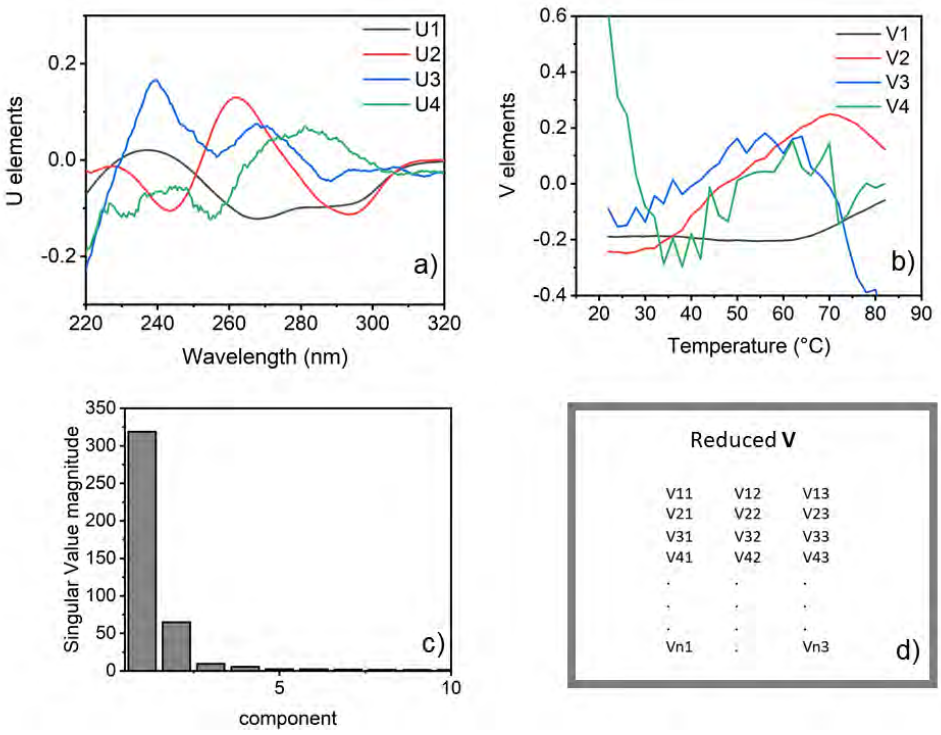

Figure 2.12: Basis spectra determined using SVD. a) First four column of matrix **U** and b) of matrix **V**. c) Histogram of the magnitude of the first ten singular values. d) Reduced **V** matrix composed by the first three columns.

As the number of columns increases, the vectors have a progressively randomly distributed shape. From some parameters related to these matrices, it is possible to obtain the number of spectral species that comprise the whole experimental dataset independently of any physical/chemical model. This is one of the most beneficial and outstanding features of SVD analysis. The screening to determine the number of significant vectors was done using Octave with a homemade script,

which is composed of a few steps and it:

1. Evaluates the singular values, plotting them in a graph; a sharp slope change is present when the magnitudes of the singular values diminish, collapsing into noise (see figure 2.12 c)).

2. Calculates the relative variance of each singular value. A cut-off can be set when the sum of few singular values reaches a relative variance higher than 0.99.

3. Calculates the auto-correlation of the vectors in **U** and **V** matrices. To be significant, they have to be larger than 0.8. The shapes of the selected vectors are non-random, while the others are usually noise-like.

From these parameters, the number of significant components can be extracted, and the whole experimental dataset is reproduced, with a good approximation, just with the reduced matrices, in which only the significant diagonal elements of the **S** matrix and the corresponding columns of the **U** and **V** matrices are kept. This last step is summarised with the following equation, where $\mathbf{U}'$, $\mathbf{S}'$, $\mathbf{V}'$ are the reduced matrices:

$$\mathbf{D}' = \mathbf{U}'\mathbf{S}'\mathbf{V}'^{T} \tag{2.12}$$

The reduced matrix $\mathbf{V}'$ is shown in figure 2.12 d), where just the first three vectors were selected from the screening that evaluates the number of significant components. To reconstruct the real species and to get the thermodynamic parameters, the reduced V' vectors have to be fitted with specific equations related to the physical mechanism analysed. The idea is that the whole dataset is made of several topology species ($St_j(\lambda)$), with a specific CD signal, and their populations $M_j(T, p_k)$ change as temperature increases, p_k are the model parameter, like thermodynamic quantities. The **D** matrix can be decomposed as:

$$\mathbf{D}(\lambda, T_i) = \sum_{j=1}^{N} St_j(\lambda) M_j(T_i, p_k) \tag{2.13}$$

and in matrix notation:

$$\mathbf{D} = \mathbf{StM}(p_k) \tag{2.14}$$

Considering that $\mathbf{D}$ can be approximated with $\mathbf{D}'$ without losing precious information and that the $\mathbf{U}'$ bases have just mathematical significance and that they are orthonormal to $\mathbf{D}'$, the linear combination of them can give any other set of basis vectors, for instance, $\mathbf{St} = \mathbf{CU}'$, where $\mathbf{C}$ is a matrix of coefficients. Combining equations 2.12, 2.14 and this last assumption, the thermodynamic model can be founded on the hypothesis that:

$$\mathbf{V}'^{T} = \mathbf{CM}(p_k) \tag{2.15}$$

Therefore, in this work, the V' vectors were fitted with an extension of van't Hoff equations (Equation 2.16, 2.17 and 2.18) and a set of rotational coefficients. From the results, it would be possible to reconstruct the topological species $St_j(\lambda)$ and their populations $M_j(T, p_k)$. Figure 2.13 a) shows a fitting example, while in panel b) the coefficient matrix and the thermodynamic equations used for the fit are present.

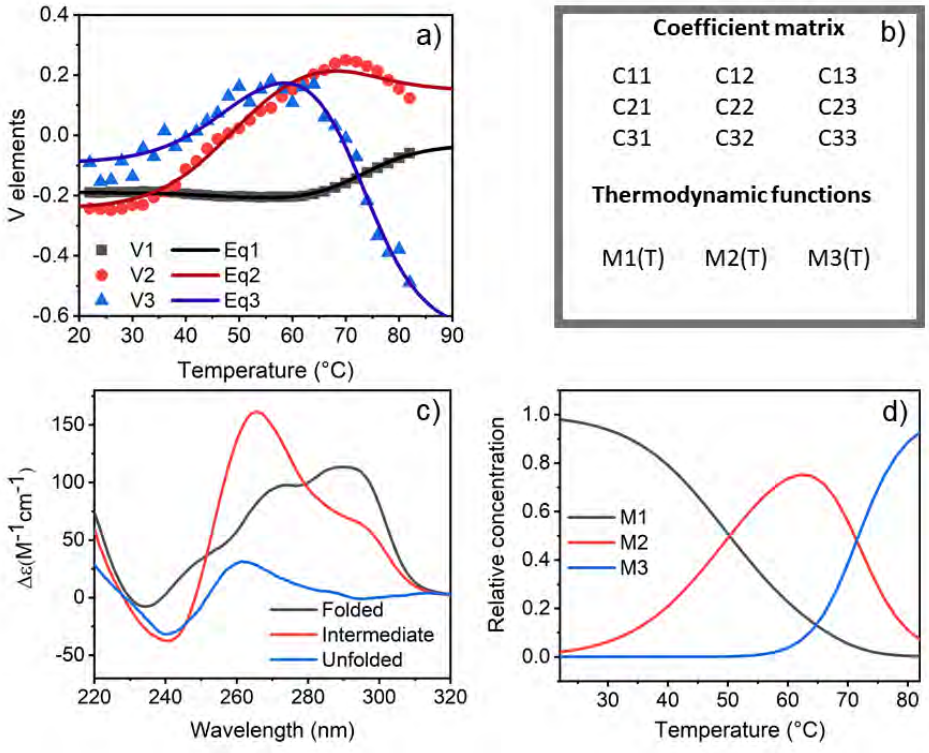

Figure 2.13: Global fit results. a) Fit of the vectors in $\mathbf{V}'$ with a linear combination of 2.16, 2.17, and 2.18. b) Schematic view of the $\mathbf{C}$ matrix and the thermodynamic equations. c) Reconstructed spectra of significant species (folded, intermediate, unfolded) and d) their relative concentrations (M1, M2, M3).

Since in this work the van't Hoff equations were used to fit the V' vectors, the p_K parameters are the temperature and the enthalpies related to each step of the unfolding. Global nonlinear least-squares fitting of the SVD amplitude was optimised with a custom-made script implemented in Gnuplot [84]. Once obtained the coefficients of the $\mathbf{C}$ matrix, they are used to reconstruct the real significant species (see figure 2.13 c)), which are a linear combination of the vectors in the $\mathbf{U}'$ matrix, while the extracted thermodynamic parameters serve to build the populations (see figure 2.13 d)) relative to each species.

$$M1(T) = \frac{e^{-\frac{dH1}{R}(\frac{1}{Tm1}-\frac{1}{T})-\frac{dH2}{R}(\frac{1}{Tm2}-\frac{1}{T})}}{e^{-\frac{dH1}{R}(\frac{1}{Tm1}-\frac{1}{T})-\frac{dH2}{R}(\frac{1}{Tm2})} + e^{-\frac{dH1}{R}(\frac{1}{Tm1}-\frac{1}{T})} + 1} \tag{2.16}$$

$$M2(T) = \frac{e^{-\frac{dH1}{R}(\frac{1}{Tm1}-\frac{1}{T})}}{e^{-\frac{dH1}{R}(\frac{1}{Tm1}-\frac{1}{T})-\frac{dH2}{R}(\frac{1}{Tm2})} + e^{-\frac{dH1}{R}(\frac{1}{Tm1}-\frac{1}{T})} + 1} \tag{2.17}$$

$$M3(T) = \frac{1}{e^{-\frac{dH1}{R}(\frac{1}{Tm1}-\frac{1}{T})-\frac{dH2}{R}(\frac{1}{Tm2})} + e^{-\frac{dH1}{R}(\frac{1}{Tm1}-\frac{1}{T})} + 1} \tag{2.18}$$

Chapter 3:

Human telomeric G-quadruplex $AG_3(TTAG_3)_3$

3.1 Introduction

This chapter is dedicated to the characterisation of the human telomeric G-quadruplex $AG_3(TTAG_3)_3$ (Tel22). This sequence is the one that has been used throughout the discussion of the thesis, therefore it is the main character of this work. Studying Tel22 is highly tricky since many factors affect its polymorphic nature. To highlight its behaviour in different experimental conditions, a multi-technique approach was needed. The results show that the environment is a critical factor in regulating G4 conformational properties. Here DNA concentration, temperature, and solvent effect are taken into account.
The results presented in this chapter are mainly from two articles we published in 2022 [73, 85].

3.2 Sample preparation

The oligonucleotide $AG_3(TTAG_3)_3$ (Tel22) was purchased from Eurogentec and used without further purification. For all the measurements in solution, the same procedure was followed [79, 86, 87], if another procedure was used it is specified in the text. The powder was dissolved in 50 mM phosphate buffer at pH 7, 0.3 mM EDTA, and 150 mM KCl, heated to 95 °C for 8 minutes and then slowly cooled down to room temperature with steps of 5 degrees in 3.5 hours. The sample was left at room temperature overnight. The concentration of the solution was estimated from UV absorption measurements at 260 nm, using a molar extinction coefficient of 228500 $M^{-1}cm^{-1}$. An example of Tel22 absorption spectrum is reported in figure 3.1 a). Each DNA stock solution was prepared

at about 1 mM. At higher concentrations, Tel22 starts to aggregate and these aggregates are not completely destroyed also at 95 °C [73]. In this chapter, the spectra obtained by annealing DNA at higher concentrations will also be shown; just for them, a different procedure was used, where the first annealing was done at around 13 mM, and then the samples were diluted to obtain concentrations of 4.5 mM, 1.2 mM, and 0.6 mM and annealed again.

3.3 Tel22 in standard conditions

To investigate the Tel22 polymorphism, the first step was to characterise its structure using a multi-technique approach able to observe DNA over a wide spatial landscape. Circular dichroism, UV-Vis absorption, small angle scattering, and UV resonance Raman spectroscopy can give insight into DNA structural and molecular aspects. Each method is characterised by distinct markers for G4, giving specific information that can be combined with the results obtained from other techniques. Figure 3.1 a) shows the UV-Vis absorption of Tel22 in solution at 40 μM, characterised by a peak at 260 nm, typical of DNA, which derives from the conjugated double bonds in the purine and pyrimidine rings. Figure 3.1 b) shows the corresponding CD spectrum, which is the identity card of the G4 secondary structure. Under our experimental conditions, i.e. potassium buffer and 40 μM DNA concentration, Tel22 is in a mix of antiparallel and hybrid conformations, characterised by a maximum at $\sim$ 295 nm, a shoulder at 270 nm, and a minimum at 240 nm.

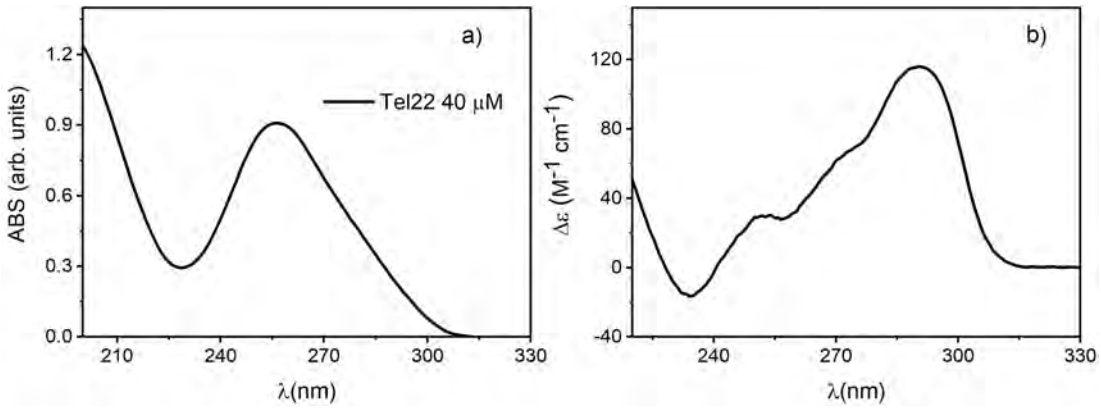

Figure 3.1: a) Absorption and b) CD spectrum of Tel22 at 40 μM.

UVRR measurements were carried out at the same CD conditions, exploiting

the advantage over the conventional Raman technique to use rather low concentrations of DNA due to the enhancement of the Raman intensities of the bands assigned to the distinct chromophores of the system. A 250 nm excitation wavelength ensures that, in the case of Tel22, the bands at ~ 1482 cm^{-1} (band A), 1578 cm^{-1} (band B), and 1611 cm^{-1} (band C) are mainly related to the dG residues vibrations, with a smaller contribution from the dA [88, 89]. Base stacking interactions suppress the resonance Raman signal [90] and, therefore, the intensity of these bands provides information on the unstacking of G-tetrads. Figure 3.2 shows the UVRR of Tel22 in the 1200-1800 cm^{-1} region: each band depends on different molecular vibrations, the band A is assigned to the bending of C8–H and the stretching of N9–C8 and C8–N7, band B arises from the stretching modes of C4–N3, C5–C4, and N7–C5 in dG residue, while band C is mainly attributable to the NH_2 scissoring mode [88]. Both guanine and adenine exhibit these in-plane vibrations, although the latter exhibits a much smaller enhancement since its absorption is almost at a minimum at 250 nm.

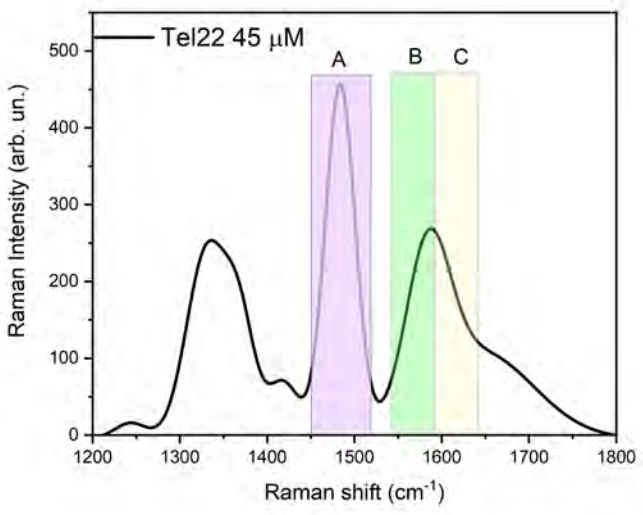

Figure 3.2: UVRR spectra of Tel22 at 45 μM. The principal bands are highlighted with different colours.

To complete the structural characterisation, small-angle scattering measurements were performed, providing valuable information on G4 structural features at the nanoscale. The sample can be still considered in dilute conditions, being the Tel22 concentration ~ 500 μM, and the whole scattering intensity derives from the form factor, while the structure factor can be neglected since in this

dilute regime the scattering intensity is proportional to the averaged scattering from a single particle and the intermolecular correlations are not observed.

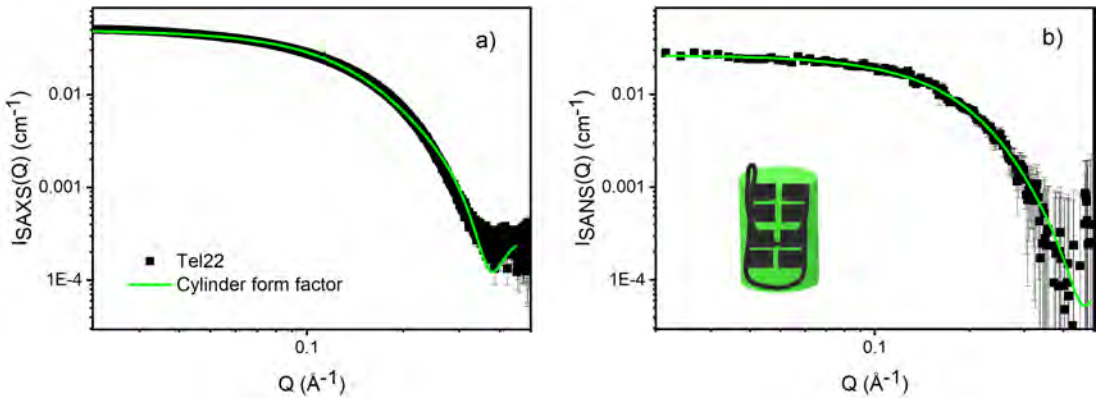

Figure 3.3: Comparison between the SAXS a) and SANS b) patterns (black) of Tel22 profile with the theoretical form factor of a cylinder (green).

Figure 3.3 represents the SAXS and SANS patterns: they are both characterised by a flat shape at low Q, while at high Q they have a Q^{-4} trend. This behaviour is typical of objects of cylindrical shapes, the form factor of a cylinder can indeed reproduce the experimental data. Tel22 is in a monomeric state in these conditions, therefore this cylinder can be seen as a monomeric unit. SAXS profiles are well represented by a cylinder with radius 10 ± 1 Å and height 36 ± 1 Å, while radius 9 ± 1 Å and height 27 ± 1 Å for SANS. The discrepancy of values depends on the fact that SAXS is sensitive to the contrast contributions from the hydration layer and the ion cloud, while SANS is not [91, 92].

3.3.1 Tel22 unfolding

Usually, the G4 melting pathway can not be described as a two-step model, where just the folded and unfolded populations are present. Many works have shown that at least one intermediate is needed to complete the telomeric G4 denaturation pathway [68, 79]. A two-state model oversimplifies the complexity of the denaturation process, losing precious information on the stability of different conformers. Knowing the thermodynamic parameters of the intermediate states offers a way to understand the switching between conformers and this is fundamental to increase our comprehension of telomere stability. In this work, many melting experiments of Tel22 complexed with different drugs will be shown. Tel22 unfolding, in the experimental conditions of this thesis, was also analysed in Ref.

[79]. There, SVD was applied to CD data, finding out that the whole unfolding process contains two intermediate states. The reconstructed significant species and their relative concentration as a function of temperature are shown in figure 3.4, and the obtained melting parameters are reported in table 3.1.

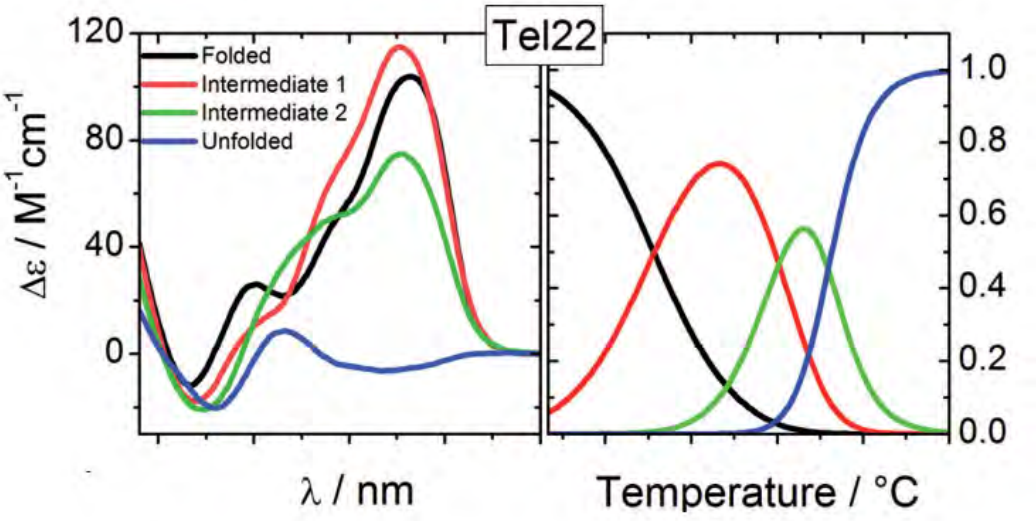

Figure 3.4: In the left panel the spectra of significant species for Tel22 and in the right panel their relative concentration as a function of temperature. Figure is taken from [79].

Table 3.1: List of parameters associated with Tel22 melting, obtained with SVD analysis [79]. Temperature are expressed in °C and enthalpies in kcal mol^{-1}.

	T_{m1}	T_{m2}	T_{m3}	dH_1	dH_2	dH_3
Tel22	38.5±0.3	60.3±0.3	68.9±0.2	-27±2	-41±3	-63±4

3.4 Conformational changes and aggregation induced by DNA concentration

In the previous chapter, it was pointed out that Tel22 switches to an antiparallel structure in a sodium environment. However, even more surprisingly, it was shown a concentration-dependent conformational transition in potassium solution from a mix of systems to a parallel topology [51]. Aware of that, a campaign of measurements was carried out to understand the impact of the concentration

starting from the preparation procedure. This section will show samples prepared by annealing at higher concentrations, see section 3.2, where aggregates are formed so strongly that not even the dilution or a second annealing can break them. SAXS measurements on G4 solutions at various DNA concentrations were employed to investigate the structural properties of concentrated G4 samples. The scattering pattern can be divided into two regions, high Q with Q$>$ 1 nm^{-1}, where the signal is mainly dependent on the form factor P(Q), as happens in dilute conditions, and low Q, where the Tel22 multimerisation is remarkable since in this region the scattering is more sensitive to the large length scales objects. Figure 3.5 shows the higher-order structures arising from the multimerisation of G4 units, and Tel22 monomer prepared with the standard G-quadruplex procedure (see section 3.2).

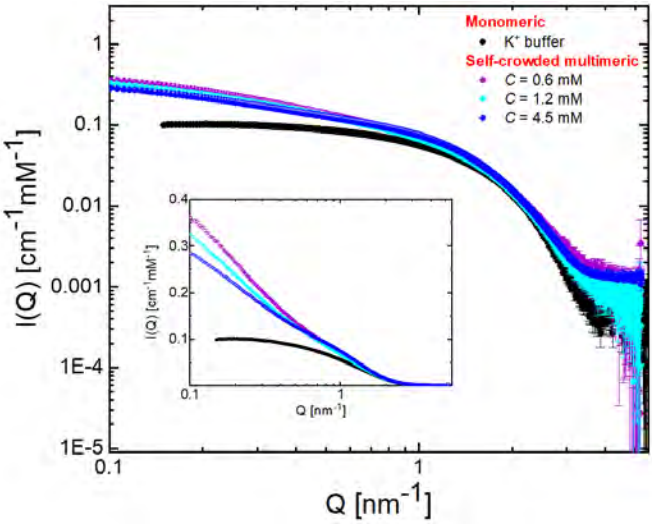

Figure 3.5: SAXS intensities of Tel22 at different concentrations. The data are presented in absolute scale and are normalised to each molar concentration. In the inset, the same data are shown on a linear-log scale. Figure taken from [73].

While the form factor in the monomeric state can be described as a hard cylinder, the other spectra need more care to be analysed. To get information on Tel22 self-assembly, a novel computational approach was used to reproduce the SAXS intensity through Monte Carlo simulations, by modelling the Tel22 unit as a hard cylinder with two attractive sites at the basis (for more details see [73]). This coarse-grained model gives information on the hydrophobic (stacking) forces between G4 units. The stacking interaction increases along with the DNA concentration as well as the number of aggregate units with dimers and trimers being the most probable forms. It was also discovered that the samples have significant

polydispersity with an exponential distribution of lengths, implying step-growth polymerisation. All the parameters extracted by the model are presented in table 3.2 .

Table 3.2: List of parameters associated with the simulation that better reproduces the SAXS intensity of the Tel22 in self-crowding conditions.

multimeric samples	M [a]	G^0_{ST} [b] [kcal mol^{-1}]	H^0_{ST} [c] [kcal mol^{-1}]	S^0_{ST} [d] [cal mol^{-1}K^{-1}]
0.6 mM	2.5	-0.76	-6.12	-18.3
1.2 mM	2.4	-0.70	-5.82	-17.5
4.5 mM	3.4	-1.21	-6.47	-18.0

[a]Average chain length. The error on the values of M has been estimated to be of the order of 10%.[b]Stacking free energy calculated for a 1 M standard concentration of G4s and $T = 293$ K. [c]Enthalpic contribution to G^0_{ST}. [d]Entropic contribution to G^0_{ST}.

This approach is really useful because, although most studies on G4s have concentrated on their monomeric state, there is evidence that G4s can take a variety of multimeric forms [93]. The same samples were also measured by circular dichroism, to investigate the secondary structure changes, see figure 3.6.

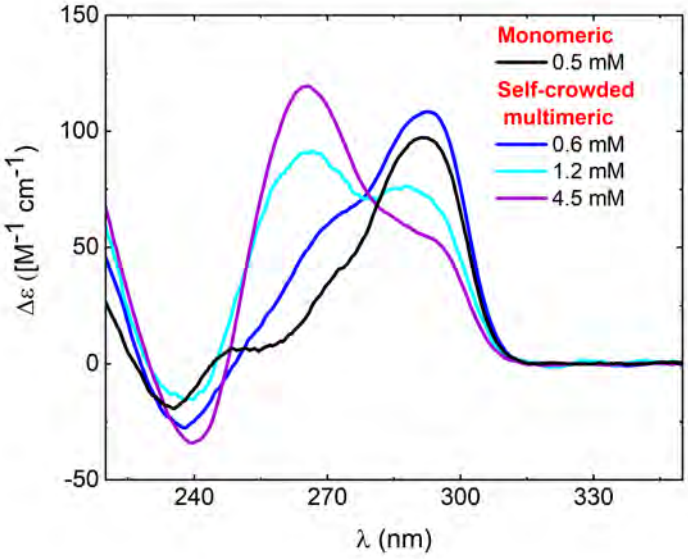

Figure 3.6: Circular dichroism of Tel22 at different concentrations. Samples at 0.5 mM (black) and 0.6 mM (blue) were measured with 0.1 mm path length quartz cuvette, while those at 1.2 mM (cyan) and 4.5 mM (violet) were recorded with the one with 0.01 mm path length. Figure taken from [73].

The monomeric Tel22 shows its typical features, with a maximum at about 295 nm, a shoulder at 270 nm, and a minimum at 240 nm; the sample at 0.6 mM with aggregates has a similar shape with a higher shoulder. As concentration increases, the maximum shifts down and a new peak appears at 265 nm, indicating an increase of the parallel topology. This analysis that combines experiments with simulations can give a quantitative picture of human telomere G4 multimerisation. In future, this methodology could be applied to extended G4 telomeric sequence, offering precious information for the rational design of anticancer drugs.

3.5 Correlation between Tel22 and solvent vibrations upon melting

This section goes in more detail into the knowledge of the solvent structural properties around the Tel22 upon thermal melting. As a matter of fact, UVRR exploits simultaneously the vibrational behaviour of G4 and its aqueous solvent. In general, not much is known about the hydration layer around G4. Most of the work has been performed in crowded conditions, where it seems that their pronounced polymorphism is strictly regulated by their hydration [94–97]. Water molecules can go in both the medium and the narrow grooves; however, recent research found out that the latter can accommodate extended filiform networks of water molecules, called spines [98]. Antiparallel and hybrid topologies are indeed more prone to host stable water spine structures. In diluted conditions, many factors affect the G4 structure because each state is separated by small energy barriers, therefore it is intriguing to investigate the relation between solvation and G4 conformations.

This analysis focuses on both solute and solvent UVRR fingerprint regions and, upon melting, their vibrational features are connected with CD secondary structure information. In this case, to access the DNA chromophore vibrations and acquire the OH stretching region, an excitation wavelength of 220 nm was used. Figure 3.7 shows the UVVR spectra of Tel22 from 1000-4000 cm^{-1} at different temperatures. The Tel22 region (I) is extended from 1300–1800 cm^{-1} while the vibrations associated with the intramolecular structure of the H-bond network from 3000–3900 cm^{-1} (II). Experimental profiles were acquired in a temperature

range between 26 °C to 90 °C at steps of 4 degrees. As temperature increases, the spectra in region I exhibit a growth in intensity due to the unstacking process caused by unfolding.

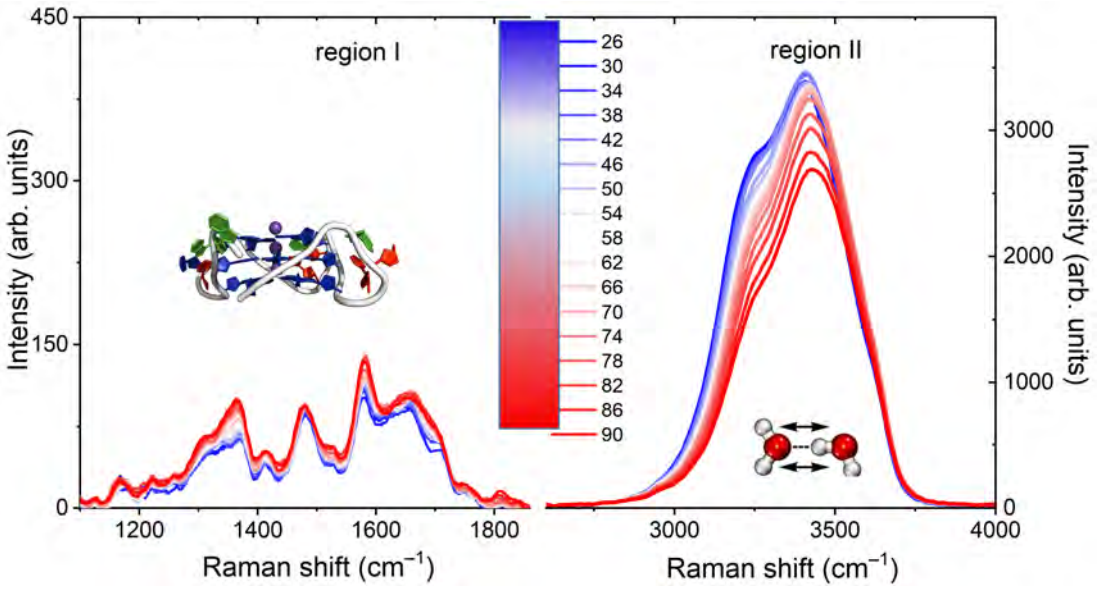

Figure 3.7: UVRR spectra of the Tel22 at 45 μM as a function of temperature. Figure taken from [85].

3.5.1 SVD analysis

Bidimensional analysis over the Raman fingerprint regions was employed to get access to the multistep thermal path towards the unfolding of the vibrational bands related to stretches of ring bonds of the nucleotide basis and water vibrations. The SVD was applied to both the Raman regions and three spectroscopically distinct species were found in each range in agreement with [79], where the excitation wavelength was set at 250 nm. The melting pattern is described by a Fold-Intermediate-Unfold process (F⇌I⇌U) and, since both the zones possess this behaviour, a global fit, to get the thermodynamics parameters, of the two datasets by sharing the T_{m1} and the T_{m2} was performed. The temperatures found for each step were T_{m1} (44 °C) and T_{m2} (76 °C), respectively. The obtained parameters are reported in table 3.3 and figure 3.8 shows the spectral species and their relative populations as a function of temperature.

Table 3.3: Melting parameters for Tel22 aqueous solution from a global fit on SVD vectors derived for both regions I and II. T_{m1} and T_{m2} were shared parameters.

	T_{m1} (°C)	44.1 ± 2.5
	T_{m2} (°C)	76.0 ± 3
zone I	dH_1 (kcal mol^{-1})	-56.1±3.5
	dH_2 (kcal mol^{-1})	-44.6± 3.4
zone II	dH_1 (kcal mol^{-1})	-18.8±3.5
	dH_2 (kcal mol^{-1})	-38.5±3.5

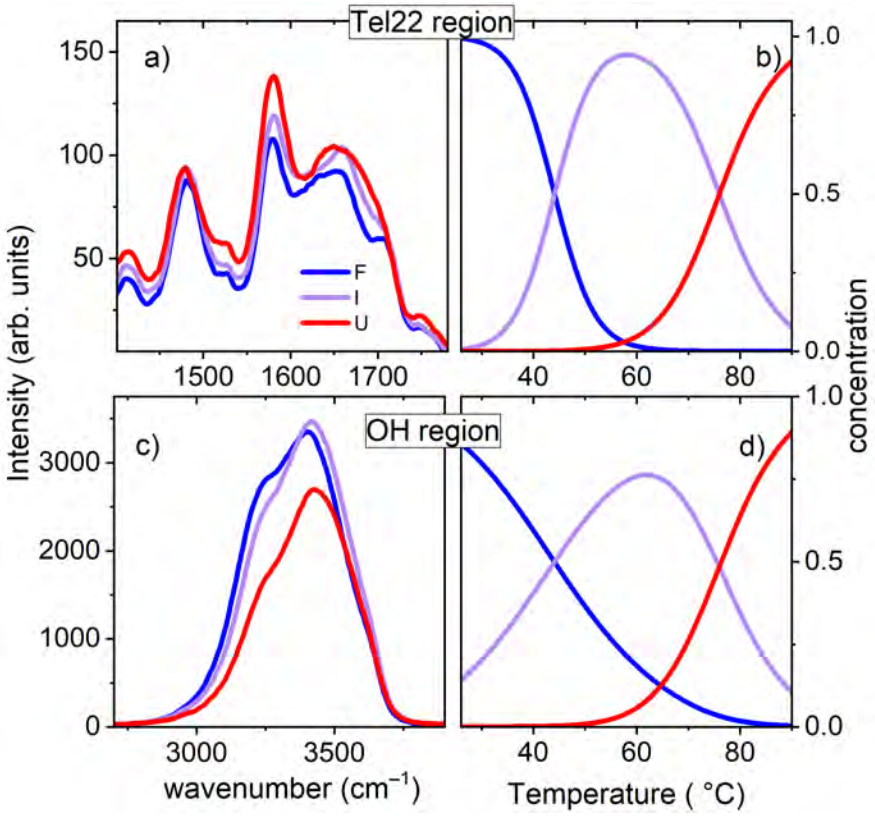

Figure 3.8: SVD results on the two UVVR regions. In a) and c) spectral species of Tel22 and OH stretching region respectively, in b) and d) their populations. Figure is taken from [85].

3.5.2 Gaussian analysis

To get information about modifications induced by temperature on different vibrational groups, Raman spectra of the area I were fitted using Gaussian func-

tions, three of them centred at about 1482, 1575, and 1666 cm^{-1}. With an excitation wavelength of 220 nm, the first is ascribed to out-of-phase stretching of the dT ring coupled to C5H3 and to the C2 carbonyls, the second to dA N6H scissoring, with a smaller component attributed to the stretching of the system C2=N3-C4=C5-N7=C8 of dG, and the third depends on the stretching of carbonyl moieties of dG residues (C6=O) [88, 99]. Temperature leads to a modification in the C5-H bond strength that can be extrapolated following the downshift of the group vibration centred at 1482 cm^{-1} (ν_{1482}), while variations on the N6-H and C6=O bonds are consistent with an upshift of the group vibration centred at 1575 cm^{-1} and 1680 cm^{-1}(ν_{1575} and ν_{1680}, respectively).

The spectra of zone II were deconvolved applying a method employed for water in diluted solutions [100], where three different contributions were considered:

- Connective water, where the OH oscillators are phase-correlated with oscillators of the nearest molecules, ice-like tetrahedral water arrangements (centred at ν_{OH1}=3200 cm^{-1}) [101, 102].
- Close water structures, where there is no phase correlation and the H-bonds are partially distorted (centred at ν_{OH2}=3450 cm^{-1}) [103].
- Transient species formed during the H-bond network reorganisation, where OH groups are feebly stabilised by H-bond interactions (centred at ν_{OH3} = 3600 cm^{-1}) [103, 104].

Figure 3.9 shows the agreement between the experimental and theoretical curves. Upon melting, the behaviour of ν_{OH1} and ν_{OH2} frequency bands suggests a weakening of the hydrogen bonding. Two kinks are visible in the temperature behaviour of the frequency position related to the Tel22 peak and to the ν_{OH1} and ν_{OH2}. These kinks correspond fairly well to the T_{m1} and T_{m2} determined by the SVD analysis. The frequencies assigned to the Tel22 bases and the OH stretching have a linear relationship (figure 3.9 b), c), d)) and a Pearson's r value above 0.75, which is defined as the fraction between the covariance of two variables and the product of their standard deviations. This value confirms a correlation between ν_{1482} *vs* ν_{OH1} (and *vs* ν_{OH2}), ν_{1575} *vs* ν_{OH1} (and *vs* ν_{OH2}), and ν_{1680} *vs* ν_{OH1} (and *vs* ν_{OH2}), demonstrating that the temperature-dependent vibrational features of the G4 structure are strictly correlated with the OH stretching band, which is mainly related to the local hydrogen-bonded network of the solvent. A

correlation, upon melting, between solute and solvent molecular vibrations, is brought to light.

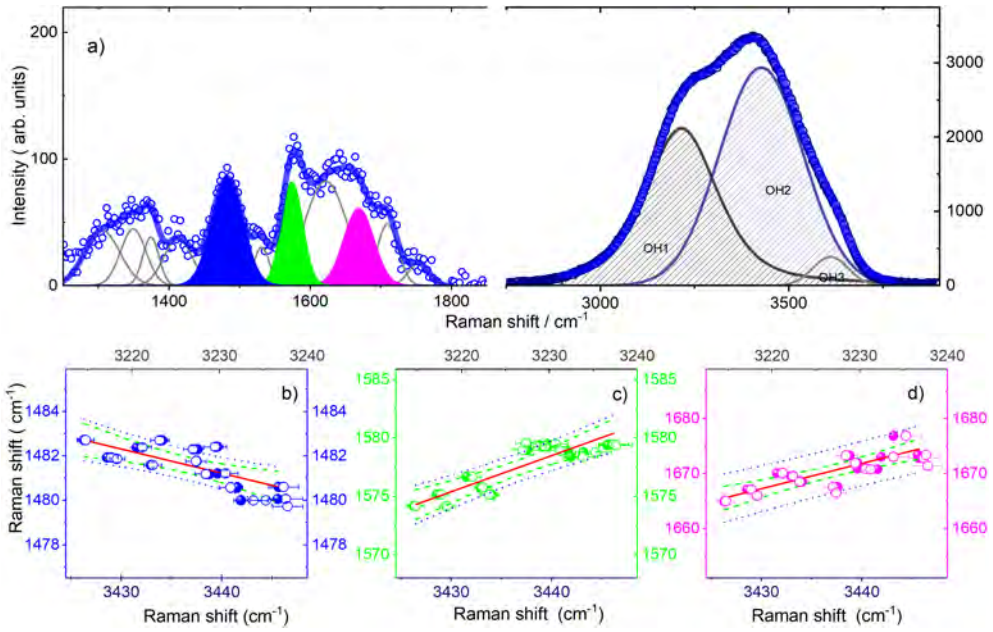

Figure 3.9: a) Experimental and theoretical UVRR spectra of the Tel22 at 45 μM at room temperature. b) Plot of ν_{1482} vs. ν_{OH1} (left-botton) and ν_{1482} vs. ν_{OH2} (right and top), c) plot of ν_{1575} vs. ν_{OH1} (left-botton) and ν_{1575} vs. ν_{OH2} (right and top) and d) ν_{1670} vs. ν_{OH1} (left-botton) and ν_{1670} vs. ν_{OH2} (right and top). In all three plots, the red line shows the fit with a straight line. Figure is taken from [85].

3.5.3 OH structuring/destructuring

A parameter that can test the structuring/destructuring effect on water influenced by the solute is $O(T) = I\nu_{OH1}/I_{OHtot}$, where I$\nu_{OH1}$ is the total area of the OH stretching of the connective water, while Iν_{OHtot} the total area of the OH stretching. In dilute conditions, $O(T)$ gives information on the proportion of OH groups in ordered tetrahedral structures [100]. To understand the effect of Tel22 on the structuring of the hydrogen bonding network, the $O(T)$ was estimated in presence of the G4 and the buffer alone at different temperatures. The value obtained with buffer alone has a linear trend, already observed in literature [100], while the one with Tel22 presents a deviation from the linearity. Figure 3.10 shows these two behaviours and the first derivative of $O(T)$ points out two inflection points at 44°C and 73 °C, which are in agreement with those obtained with the SVD.

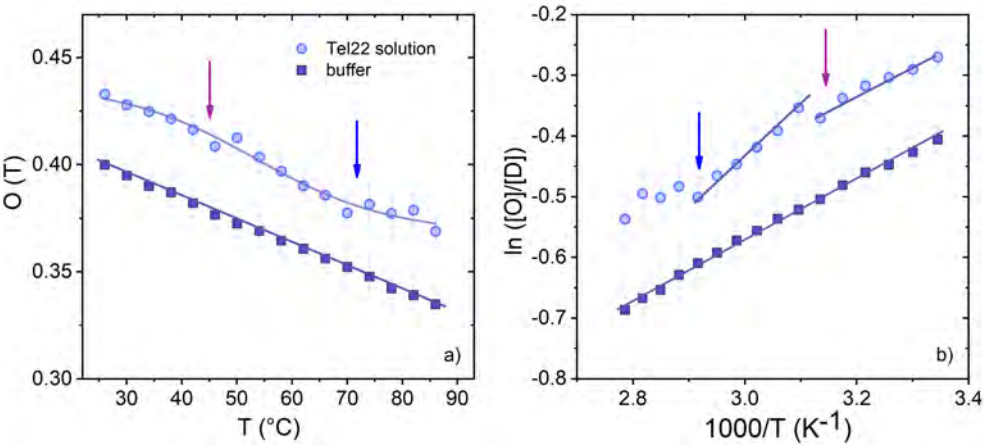

Figure 3.10: a) $O(T)$ parameter as a function of temperature. The buffer is represented by squares while Tel22 in solution by circles. The latter shows two inflection points at about T'_{m1}=44 °C and at T'_{m2}=73 °C. b) van't Hoff plot for the O↔D equilibrium for the Tel22 solution and the corresponding buffer. Arrows serve as visual guides, roughly corresponding to T'_{m1} and T'_{m2}. Figure is taken from [85].

This analysis suggests that the major Tel22 conformational changes are also reflected in the OH stretching structure. This finding supports the idea of a solute-solvent mutual interaction and also suggests that changes in G4 topology have an effect on the tetrahedral water network surrounding the solute as temperature increased. During unfolding, it is known [87] that Tel22 increases its parallel topology at the expense of the antiparallel one and a correlation between the destructuring of the OH signal is related also to this conformational modulation. This effect is in agreement with the fact that antiparallel G4s can host in their grooves ordered water spines, in contrast to what occurs in parallel ones [85].

Moreover, the enthalpy variation connected to the shift from ordered (O) to disordered (D) water structure $\Delta H_{O\leftrightarrow D}$ during the melting can be calculated using the temperature dependence of O↔D equilibrium. The thermodynamic parameter was derived by using a van't Hoff plot, defined as the logarithm of a physical quantity plotted against the inverse of absolute temperature, and shown in figure 3.10 b). In the plot, the $O(T)$ and $1 - O(T)$ are the ordered and disordered fractions of OH oscillators [105]. For the buffer, it was found ΔH= -1.10 ± 0.02 kcal mol^{-1}, while for the Tel22 water solution an irregular trend with a changing slope as temperature increased was observed. From these two trends, ΔH= 1.07 ± 0.02 kcal mol^{-1} and ΔH= 1.10 ± 0.02 kcal mol^{-1} were extracted. Also in this case, a correlation between the G4 intermediate conformational changes upon melting and the OH signal is observed.

Chapter 4:

Tel22 and ligands

4.1 Introduction

This chapter focuses on the Tel22 conformational changes and stabilisation induced by ligand complexation. Three well-known small molecules already used in several applications were selected: Berberine (Ber), Palmatine (Palm), and Braco-19 (B19). This chapter is divided into two main sections:

- In the first part, the effect of complexation of Tel22 with Ber and Palm is analysed and compared. A multi-technique approach based on circular dichroism, UV resonance Raman spectroscopy, and small angle X-ray scattering was used to get information on structural and molecular aspects of human telomeric quadruplex-ligand interactions. The results are taken from [87].

- The second section exploits with a set of biophysical probes the complexation of Tel22 with B19, one of the first rationally designed ligands. UV-Vis absorption, circular dichroism, and UV resonant Raman techniques contributed to gain complementary information about ligand-induced conformational and molecular changes; new details about the electronic transitions were further obtained by fluorescence spectroscopy, providing insights on the vibronic structure of the complex upon binding.

4.2 Berberine and Palmatine

One aspect that has to be taken into account when studying the interaction between small molecules and Tel22 is its polymorphic nature. Finding ligands that

stabilise and select G4s would be relevant for therapeutic purposes. Indeed, many efforts have been made in the drug-discovery field and testing new molecules. In this context, Ber and Palm were chosen since many encouraging results were found in studies on the interaction with G4 and in the ability to inhibit telomere elongation, blocking the telomerase action [106–108]. Ber and Palm are two natural isoquinoline alkaloids (schematic view in figure 4.1), with low toxicity, already used in the pharmaceutical fields. Both of them were isolated from Chinese herbs used in traditional medicine e.g. Coptis chinensis [109, 110]. These chemical species are often used for their ability against digestive disease and metabolic disorders, cardiovascular disease, antibacterial, antiviral, and anti-inflammatory activity, and as a neuroprotective [111, 112].

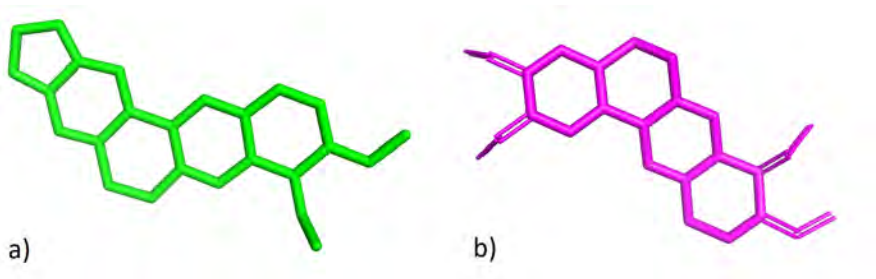

Figure 4.1: Molecular prospectus of a) Berberine and b) Palmatine.

Due to their molecular structure, these compounds can proficiently interact with DNA. Both contain flexible cyclic structure that shows high affinity for G4 [113], as well as the presence of unsaturated rings and the positively charged N atom that can increase the interaction with G4s [114]. The effect of ligand complexation on the structure and thermodynamics of Tel22 will be shown. These two ligands bind to Tel22 inducing G4 structural rearrangements and influencing its thermal pathway upon melting. The details of the conformational landscape vised by Tel22-Ber and Tel22-Palm upon unfolding will be shown, thanks to the support of a biophysical approach that combines CD, SAXS, and UVRR techniques with SVD method. This methodology is able to highlight the different effects generated from the complexation with Ber and Palm.

The G4 sample was dissolved in 50 mM MES buffer at pH 7.0, 100 mM KCl and the Ber and Palm were added to reach a DNA:drug molar ratio of 1:1.

4.2.1 CD profiles

Figure 4.2 a) shows the CD spectra of Tel22 (45 μ M), Tel22–Palm, and Tel22–Ber at 30 °C.

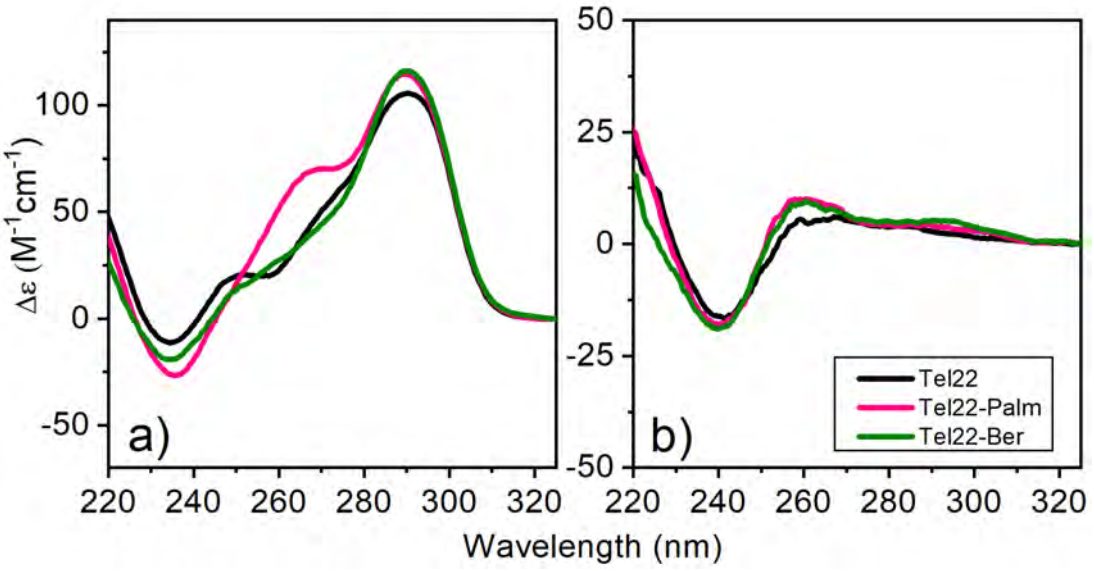

Figure 4.2: Circular Dichroism of Tel22 (black), Tel22-Ber (pink), and Tel22-Palm (green): a) at room temperature and b) at 82 °C. Figure is taken from [87].

Tel22 has a distinctive shape, with a maximum at 290 nm, a minimum at 233 nm, and a shoulder at 270 nm. Complexation induces changes in the ellipticity and, in both cases, there is an increase of the maximum. Moreover, Tel22–Palm CD spectrum has a higher positive peak at 265 nm. In figure 4.2 b) the CD spectra of the unfolded samples are presented, and the three shapes look very similar to each other.

Figure 4.3 shows the CD of Tel22 alone and complexed with Ber and Palm toward unfolding: as for Tel22 alone [79], the other samples visit different topologies as the temperature increases. SVD was used to identify the number of intermediate states and to quantify the thermodynamic parameters upon melting. Since samples were dissolved in MES buffer with lower KCl with respect to the samples described in [79], SVD analysis on Tel22 was repeated as G4 melting parameters are strongly affected by salt concentration. Two intermediates are necessary to describe the whole melting process, according to a sequential model N$\leftrightarrow$ I_1 $\leftrightarrow$ I_2 $\leftrightarrow$U, where N is the native state, I_1 the first intermediate, I_2 the second intermediate, and U the unfolded state. This model well reproduces the experimental

data.

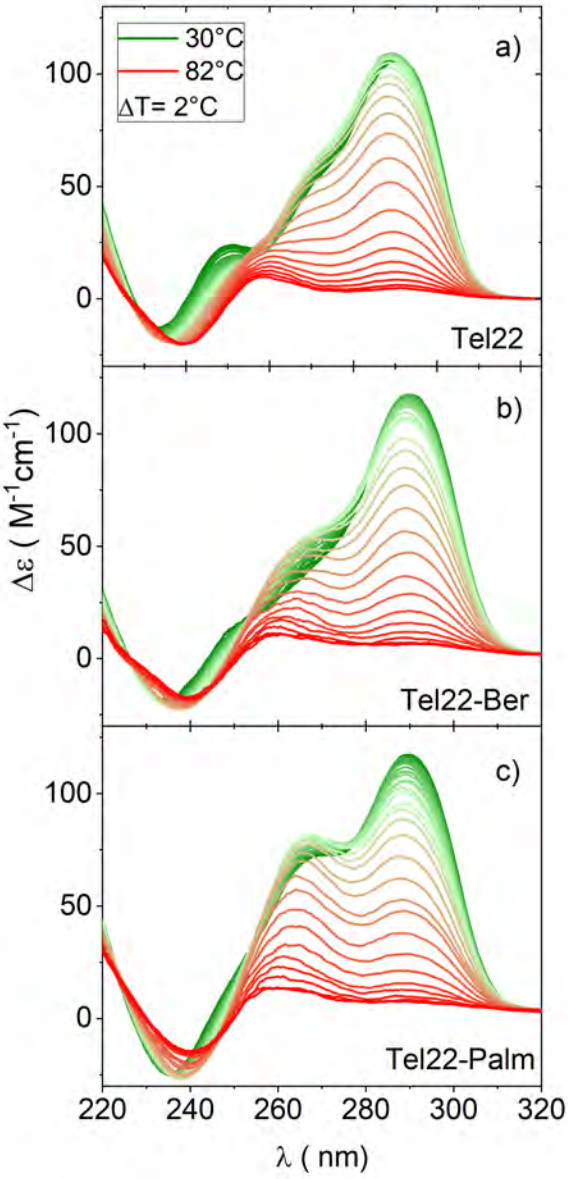

Figure 4.3: Circular Dichroism spectra of a) Tel22, b) Tel22-Ber and c) Tel22-Palm toward the unfolding. Figure taken from [87].

From the global fit on the V vectors, the thermodynamic parameters were extracted and reported in table 4.1. Both Palm and Ber stabilise the Tel22 structure, increasing the melting temperature by 7 °C and 6°C, respectively. From these data, the free energy (ΔG) at 25 °C can be calculated and the difference between the one of Tel22-drug and the one of Tel22 alone ($\Delta\Delta$G=$\Delta G_{Tel22-drug}$-ΔG_{Tel22}) gives an indication on the binding affinity. These values $\Delta\Delta G_{Tel22-Ber}$=

-5 ± 2 kcal mol^{-1} and $\Delta\Delta G_{Tel22-Ber}$= -5 ± 2 kcal mol^{-1} are in agreement with isothermal titration calorimetry estimations [107, 108].

Table 4.1: Thermal melting parameters obtained from SVD for Tel22, Tel22-Ber, and Tel22-Palm in MES buffer.

	Tel22	Tel22-Ber	Tel22-Palm
T_{m1} (°C)	43.0 ± 0.9	40.0 ± 0.8	42.3 ± 0.5
T_{m2} (°C)	58.0 ± 0.8	61.9 ± 0.8	62 ± 2
T_{m3} (°C)	63.0 ± 0.5	70.1 ± 0.5	69.2 ± 0.8
dH_1 (kcal mol^{-1})	-30±3	-22±2	-21±4
dH_2 (kcal mol^{-1})	-34± 3	-52±4	-41±3
dH_3 (kcal mol^{-1})	-40± 4	-74±4	-69±8

Figure 4.4 left panels show the native, the intermediate and the unfolded states built through SVD, and the right panels present the population of each spectrum. Despite the two drugs produce a similar effect on the thermodynamics parameters, the CD profiles are very different towards unfolding, suggesting that they induce diverse conformational changes. Tel22 alone is in a mix of conformations and as the temperature increases, the population of each topology changes. To analyse more in-depth these G4 rearrangements, the native and the intermediate states of each sample were deconvolved into parallel (P), hybrid (H), and antiparallel (AP) spectra. The normalised CD signals for the three main components were taken from [51], where Tel22 secondary structure was analysed in different conformations by changing the Na^+/K^+ concentration. The obtained decomposition is shown in figure 4.5, wherein all the samples a reduction of the anti-parallel conformation as temperature increases can be observed. It is worth noting that, albeit in a different way, both drugs induce growth in the parallel-like topology. These results suggest that ligand complexation and temperature can act as Tel22 conformational switchers. Although in the cases presented here the G4 remains in a mix of configurations, the same methodology can be applied to other drugs or to other external agents to monitor a complete switch. An example of other parameters that can be changed is the DNA concentration, the DNA sequence, the ion strength, as well as the pressure.

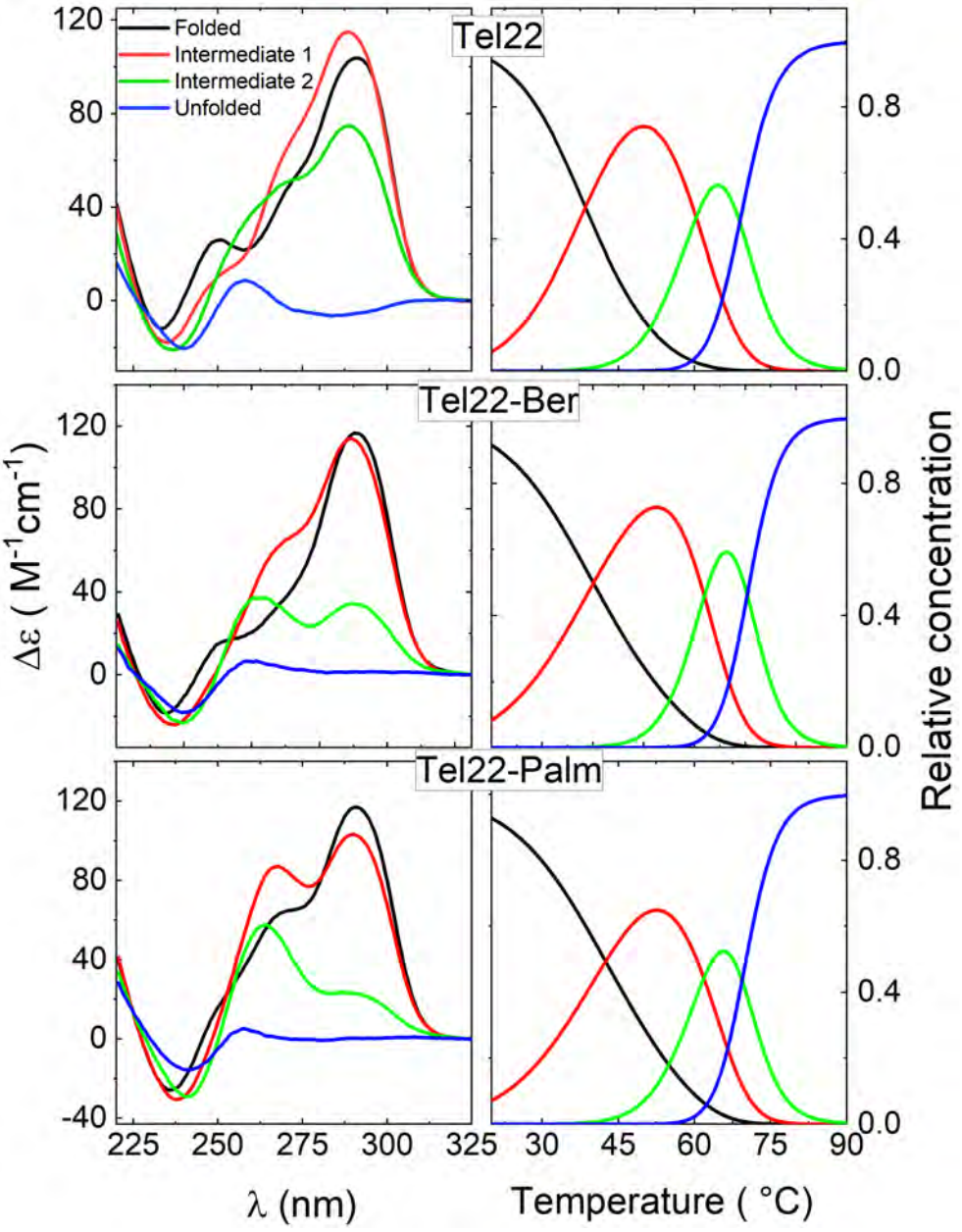

Figure 4.4: Reconstructed spectra from SVD analysis. On the left panel the significative spectral species and on the right their relative populations as a function of temperature. The figure is taken from [87].

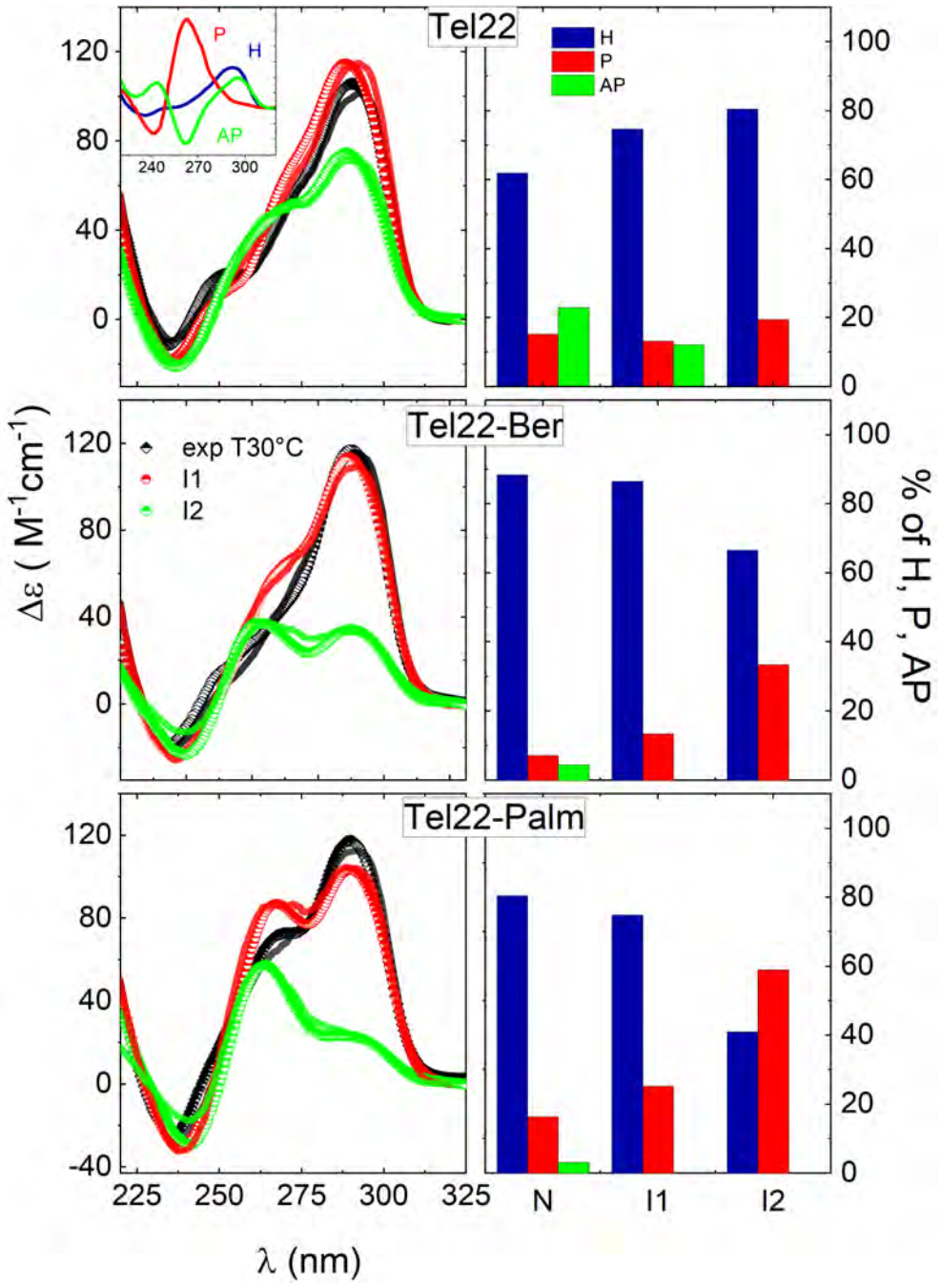

Figure 4.5: Native (experimental profile at room temperature) and intermediates I_1 and I_2 decomposed in terms of parallel, hybrid, and antiparallel signals (basis spectra taken from [51]). Tel22 at the top, Tel22-Ber in the middle, and Tel22-Palm at the bottom. Histograms show the relative amount of parallel, hybrid, and antiparallel species. Figure is taken from [87].

4.2.2 UVRR: binding interaction

To follow the complexation from a molecular point of view, UVRR spectroscopy was employed, with a 266 nm exciting wavelength, which enhances specific vibrational modes of nucleobase groups. As reported in the previous chapter, Tel22 fingerprints are present in the region from 1150 to 1600 cm^{-1}. With 266 nm exciting wavelength, the signal of the thymine is mostly related to the peak at 1375 cm^{-1}, while the contribution of guanosine and adenine overlaps around the peaks at 1325, 1335, 1485, and 1580 cm^{-1}. Figure 4.6 shows the spectrum of Tel22 and the linear combination of the spectra of the following nucleotides: 12 dGTP, 4 dATP, and 6 dTTP. The nucleotide experimental profiles were initially normalised to their total area.

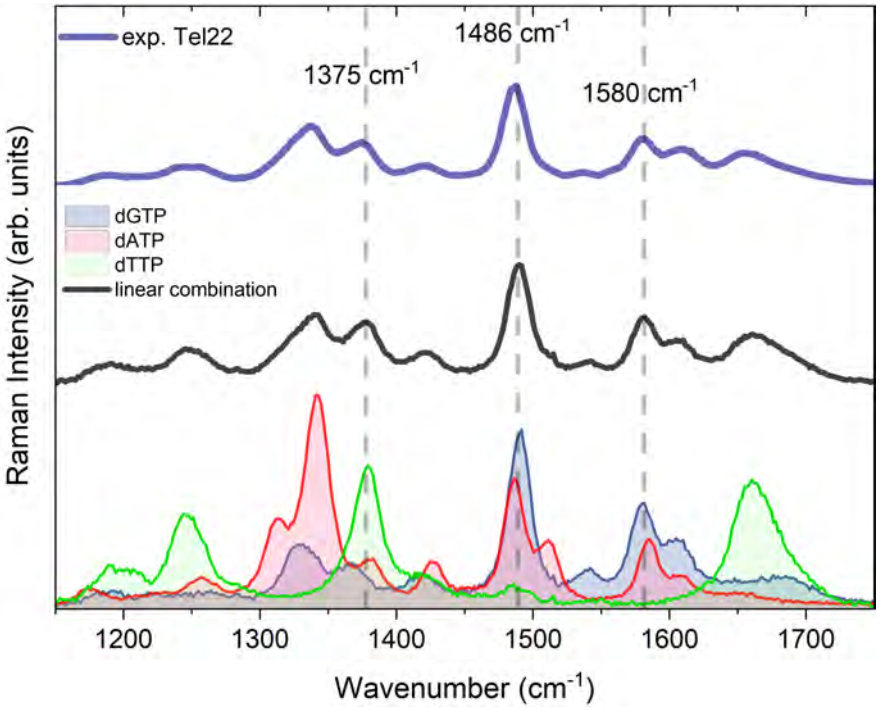

Figure 4.6: UVRR spectrum of the linear combination of 4 dATP + 12 dGTP + 6 dTTP and of Tel22. The nucleobase signals are shown with filled areas and are collected at 10 mM in water. Figure is taken from [87].

Ber and Palm do not produce large modifications on Tel22 UVRR spectrum, as shown in figure 4.7, which reports at the top the difference spectra (DS) between the sample with and without the drugs and the contribution of the two ligands. All the curves are normalised to the peak related to the phosphate ion (1030 cm^{-1}), empty cell was also subtracted. There is almost an overlap between the

DS and that of the drug, there are some differences in the correspondence of the peak at 1486 cm^{-1}, related to base stacking interactions, suggesting that the stacking induced by Ber is slightly stronger than that induced by Palm.

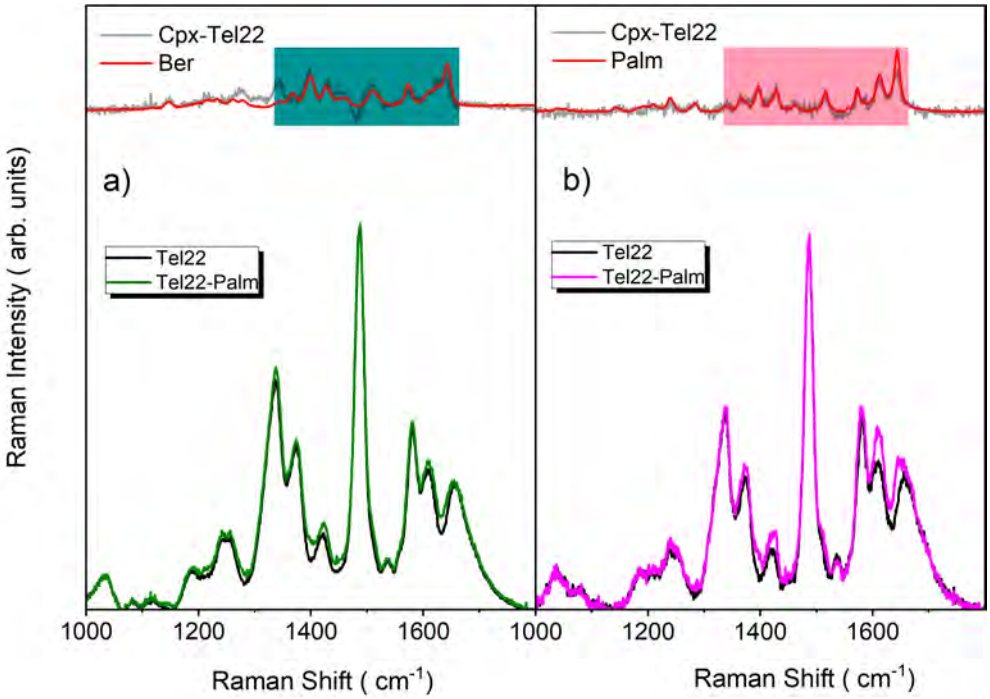

Figure 4.7: a) UVRR of Tel22 at 45 μM in black and Tel22-Palm in green. b) Tel22 in black and Tel22-Ber in magenta. The difference spectrum between complexed and native samples (Cpx-Tel22) is reported at the top of all panels, along with the rescaled profile of pure drug (red line). Figure is taken from [87].

In all the samples, toward unfolding, an increase of the band at 1335 cm^{-1} and a decrease of that at 1325 cm^{-1} are observed (figure 4.8), related to the C2'-*endo/anti* and C2'-*endo/syn* conformers, suggesting a conformational rearrangement already observed with CD.

4.2.3 SAXS: shape and molecularity of Tel22

SAXS measurements were performed to complete the picture of the structural changes of Tel22 induced by Ber and Palm. SAS technique is more sensitive to the G4 large-scale rearrangements, shape modifications, and aggregation. Figure 4.9 shows the form factor P(Q) of Tel22-Ber and Tel22-Palm with the best fit derived from SasView [115]. Squared parallelepiped model, with the short and long sides of a= 18.6 $\pm$ 0.9 Å and c=32 $\pm$ 2 Å well reproduces the P(Q) of Tel22.

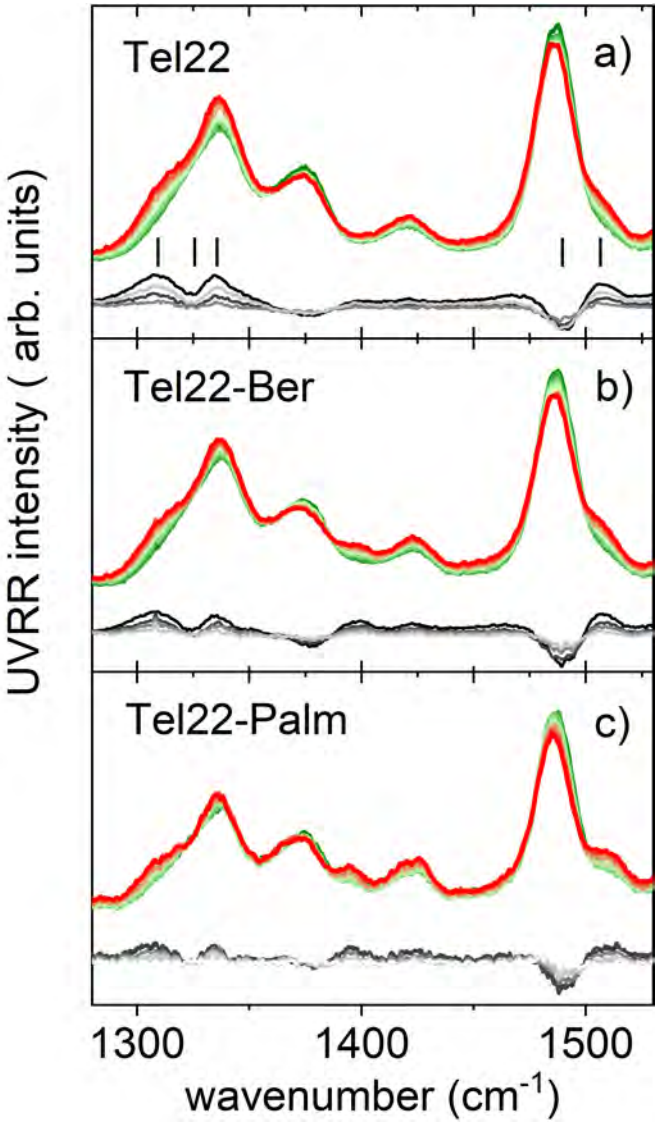

Figure 4.8: UVRR spectra collected as a function of temperature for a) Tel22, b) Tel22-Ber (1:1), and c) Tel22-Palm (1:1). At the bottom of all panels the difference spectrum between each temperature profile from darkest to lightest grey (90-30 °C DS to 40-30 °C DS spectra). The figure is taken from [87].

The same model is also applicable to Tel22-Palm, suggesting that the drug does not produce any modification at the quaternary structure level under the experimental conditions used in this study. It is worth noting that the P(Q) of Tel22-Ber cannot be described just with this simple approximation, whereas it is well fitted by the combination of the form factors of two parallelepipeds: one with the same sizes cited above and the other with the same short side but with a double long side. Such a description represents a solution of Tel22 monomers and dimers. From the fit, the dimer fraction for Tel22-Ber was found to be 0.2.

Literature suggests [107] that the two drugs stack by $\pi - \pi$ interaction on the top of G4, the positively charged N7 of Ber and Palm stabilises the negative charge density of O6 guanines. The lateral moiety probably promotes the partial dimerisation of Tel22-Ber, allowing a more favourable interaction. Even if the two ligands present many structural similarities, Ber can induce partial Tel22 dimerisation more effectively, resulting in a slightly more stable complex. This outcome is very interesting because it could be used as a basis for future studies on G4 natural-interacting small molecules, with possible developments also for medical applications.

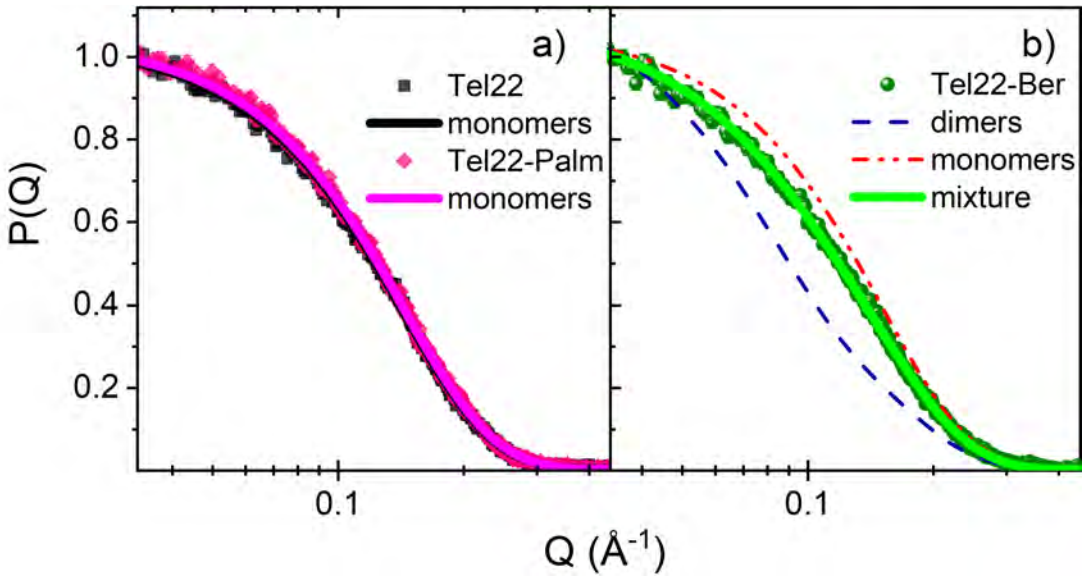

Figure 4.9: Comparison between the normalised experimental and theoretical SAXS profiles of Tel22 alone a), Tel22-Palm b), and Tel22-Ber c). Figure is taken from [87].

4.3 Braco-19

The previous sections have shown the action of natural compounds on Tel22 structure, instead, the next paragraph will be dedicated to the action of B19, one of the first rationally designed G4 ligand [116], whose molecular structure is shown in figure 4.10. It is considered an "end-stacker" and it was chosen because it shows a fair selectivity for G4 over duplex together with high inhibitory activity toward telomerase [1, 54, 99]. The effects of B19 on telomerase function have been evaluated both *in vitro* and *in vivo* tests [1, 117]. One of the fields of investigation concerns lethal cancers; for example, in the human uterus carcinoma

cell line UXF1138L, B19 produced growth inhibition of 96 % [1], in breast cancer, it inhibits diseased cell survival and induced DNA damage, in brain tumour, it may provide a new treatment of glioblastoma multiforme [118]. In addition to being a promising anticancer drug, B19 is also behaving as an antiviral molecule, as it exerts anti–HIV-1 and anti-HSV-1 activity by stabilising HIV-1 and HSV-1 G4s, respectively, and repressing the viral gene transcription [119, 120].

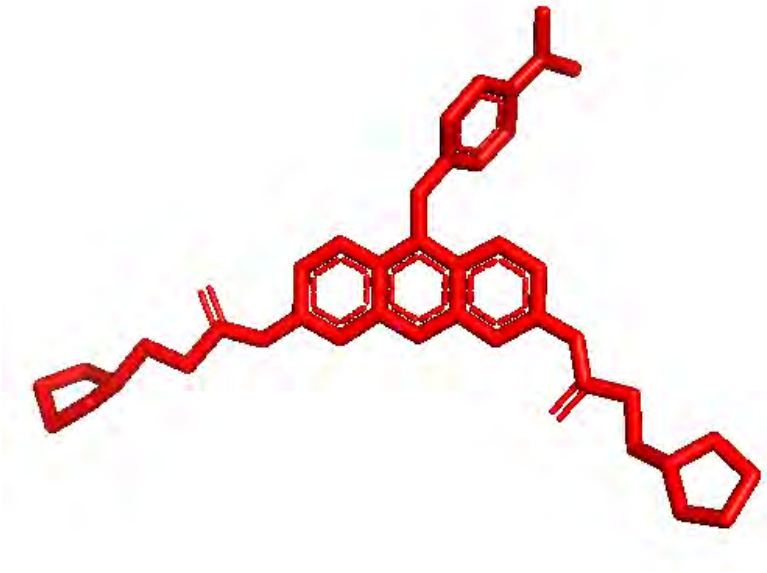

Figure 4.10: Molecular prospectus of B19.

Even if B19 is a well-studied and a good ligand for G4 [1, 121–124], there is no clear structural information on its interaction with the human telomeric G4 in physiological conditions. Moreover, the high degree of polymorphism of quadruplexes does not allow the generalisation of the results, and adding more and more details allows for enriching the database from which to start developing new compounds. Molecular dynamic (MD) simulations, used to characterise the stability of the binding modes of B19 to a telomeric G-quadruplex, showed that, depending on the starting G4 conformation, some differences in the energetic stability of top stacking and bottom intercalation binding modes, both possible, may exist [123]. By using a multi-technique approach, it is possible to explore a wide energetic landscape of G4 and G4-binder conformations. In particular, CD and UVRR spectroscopy provide information about the secondary structure and molecular vibrations upon the thermal unfolding pathway, while UV-Vis absorption and fluorescence titration can give information on the interaction, the binding mode, and the modification of the environment around the ligand due to

complexation. The use of this biophysical approach gives the opportunity to focus on the change induced by the complexation of one component without considering the other. In this section, it is shown that CD and UVVR give information on the G4 modifications, while ABS and FLUO are more sensitive to the B19 alteration.

4.3.1 Titration: Braco-19 viewpoint

In order to explore the Tel22-B19 binding mechanisms, on the basis of a previous work [125], a series of titration experiments were carried out through different optical spectroscopic techniques. To investigate the B19 electronic properties changes induced by complexation with Tel22, UV-absorption and fluorescence spectroscopy were employed. Figure 4.11 a) shows the UV-Vis absorption spectra of B19 at a fixed concentration (80 μM) in the presence of Tel22 at variable molar ratio (Tel22:B19 varies between 0:1 and 1.5:1).

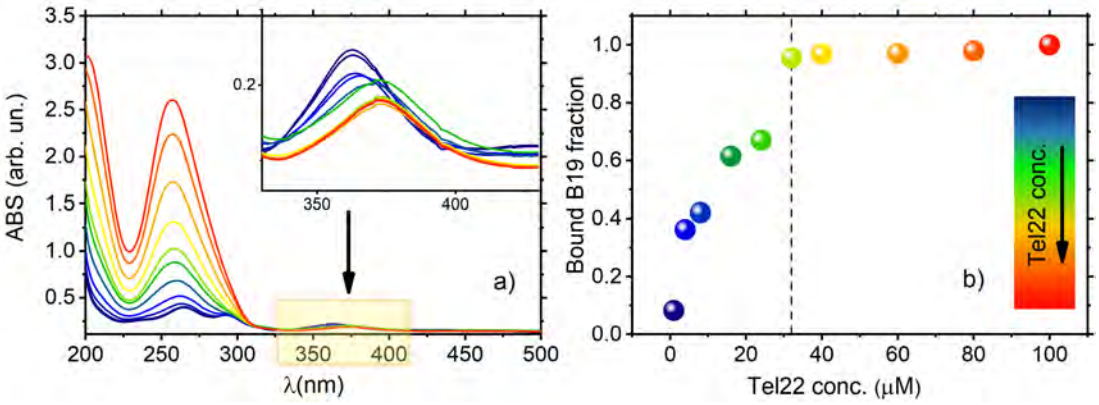

Figure 4.11: a) UV-Vis absorption titration of B19 increasing the Tel22 concentration. In the inset the absorption of B19 at 363 nm. b) Bound B19 fraction as a function of Tel22 concentration.

Increasing Tel22 concentration, the growth of the UV absorption bands at 260 nm can be easily recognised. This band hinders the effects of G4 binding on the main features of the absorption spectrum of B19. In fact, this acridine-based molecule has characteristic absorption bands with three major peaks at 264 nm, 293 nm, and 363 nm. Since Tel22 absorbs at $\sim$ 260 nm, during the titration it was observed just the modification of the band at the higher wavelength where no DNA signal is present (see inset of figure 4.11 a). Tel22 produces a 10 nm red-shift (from 363 nm to 373 nm) and a large hypochromic effect up to $\approx$ 68%. Red-shift (>15 nm) and hypochromicity (>35%) are typical of intercalative binding modes

for duplex and quadruplex DNA (for examples with porphyrins) [126]. Hence, our observation may only imply a possible stacking interaction between B19 and Tel22 but does not point conclusively to such a specific interaction mechanism. A deviation from the isosbestic point is observed, which suggests that the binding is composed of several steps. In figure 4.11 b) it is shown that the bound B19 fraction reaches a plateau at [DNA]:[ligand] ratio of 2.5. The concentrations of bound (C_b) and free (C_f) B19 were evaluated using a standard procedure [125] where C_f = C(1 - α) and C_b=C-C_f, whit C the total ligand concentration (80 μM) and α calculated through the equation: $\alpha = (A_f - A)/(A_f - A_b)$, where A_f and A_b are the absorbances of the free and fully bound B19 at 363 nm and A is the absorbance at the same wavelength for each measurement.

Assuming a single G4-B19 binding mode, one would expect to be able to reconstruct the trend by a linear combination of the spectral signatures corresponding to free and bound B19. On the other hand, the reconstruction of the observed absorption features is not feasible by considering only two states (i.e. bound/unbound). This suggests that more than one B19 binding site could be available on Tel22. In literature, the existence of a double binding mode was investigated by surface plasmon resonance and calorimetry. White et al. [127] showed that the first binding mode between the human telomeric G4 and B19 has an association constant of $K_a \sim 3 \cdot 10^7$ M^{-1}, and it is 10 folds stronger than the second binding mode.

One of the advantages of B19, as other acridine-derived G4 ligands, is the intrinsic fluorescence emission, which can provide complementary information to UV-Vis absorption studies. The fluorescence emission of B19 excited with 365 nm wavelength and its absorption spectra at 80 μM are shown in figure 4.12 a). The mirror-image rule between the absorption and the emission spectra is quite obeyed. This symmetry comes from the fact that the same transitions are involved in the two processes with similar vibrational energy levels of the ground and the excited state. The energy of the emission is less than that of absorption, in fact, fluorescence occurs at higher wavelengths. Generally, the emission spectrum is not dependent on the excitation wavelength and it was decided to excite with 365 nm because it was far from the absorption peak of the DNA. The results of fluorescence titration experiments are displayed in figure 4.12 b), with B19 concentration fixed at 80 μM. At increasing Tel22 concentration, one can notice both a non-monotonic increase in the fluorescence intensity and a gradual red-

shift of the emission spectral structure, accompanied by a loss of the spectral structure characterising the fluorescence emission of B19. As in the case of UV-absorption titration, it is not possible to reconstruct the spectra using just two states (free and bound).

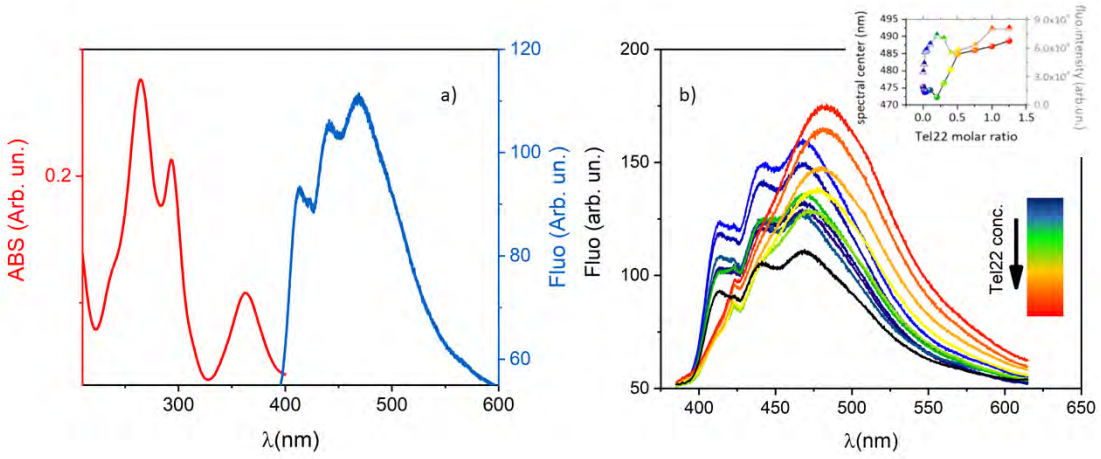

Figure 4.12: a) Absorption (red) and fluorescence (blue) spectra of B19 at 80 μM. b) Fluorescence titration of B19 increasing the Tel22 concentration from 0 μM (black) to 100 μM (red). In the inset, the evolution of the integrated fluorescence intensity (triangles, grey scale to the right) and the spectral centre (circles, black scale to the left), which is defined as the first momentum of the spectral intensity distribution.

These observations can be quantified by monitoring the evolution of the integrated fluorescence intensity (inset in figure 4.12 triangles) and the first momentum of the spectral intensity distribution (inset in figure 4.12 circles), as a function of the Tel22 concentration. Both these quantities vary non-monotonically at increasing Tel22 concentration. The fluorescence titration suggests a change in the local environment of the chromophore as the Tel22 concentration increases, which can also indicate a change in the binding process.

The first steps of the titration show a light-up effect that is probably due to a restriction on the conformational degree of freedom of the B19 when it is bounded with Tel22. This effect has already been reported with other acridine-based molecules [128] and it is probably due to decreased acridine–acridine self-quenching [129]. When 16 μM of Tel22 is added, the B19 fluorescence spectrum starts to change its shape. In general, the red-shift in fluorescence emission can be interpreted in terms of the so-called solvent effect: in the presence of polar solvents, the excited fluorophore dipole moment is partially shielded, hence weakened in dipole strength [62]. Here, however, the red-shift is accompanied by

the loss of the spectral structure that is well visible in the spectrum of B19 alone. The formation of this broad, structureless, red-shifted band with a maximum at about 490 nm, which increases its intensity upon the Tel22 titration, is consistent with an excimer emission [130, 131]. The π-stacking interactions between the Tel22 tetrads and the B19 can modify the B19 excited state and delocalise the photon over the conjugate.

Both the titration experiments do not show an isosbestic/isoemissive point, suggesting the presence of two different binding modes [132]. Moreover, from the fluorescence it is also evident that the G4 strongly changes the properties of B19 environment.

4.3.2 Titration: Tel22 viewpoint

To observe the modification of Tel22 induced by B19, CD and UVRR titration measurements were carried out. UVRR spectroscopy experiments were conducted with λ=250 nm exciting wavelength, where the bands at about 1482 (G-peak), 1578, and 1611 cm^{-1} are mostly ascribed to vibrations of dG residues, and of slight contributions from dA [88, 89]. The spectra measured for the Tel22 and the Tel22-B19 samples at three different molar stoichiometric ratios (1:1, 1:2, 1:4) are shown in figure 4.13 a) in the wavenumber range from 1200 to 1800 cm^{-1}. A decrease in the Raman signal, the hypochromic effect, upon complexation with B19 is observable in figure 4.13 c) and it can be ascribed to a modification of base stacking interactions, suggesting an end-stacking binding mode [90]. Increasing the B19 concentration also leads to a G-peak red-shift, as shown in figure 4.13 c) (green layer), indicating a change in the strength of the bonds.

Tel22 secondary structure modifications induced by B19 were pointed out by CD experiments. Tel22 in potassium buffer shows a CD spectrum characteristic of a hybrid conformation, with a maximum near 290 nm, a shoulder at 270 nm, and a minimum at about 235 nm. The complexation provokes a drastic change, with an increase of the peak at 290 nm and the formation of a minimum at 260 nm, see figure 4.13 b) and d). Therefore, upon complexation, the Tel22 structure undergoes conformational switching from a mix of hybrid and antiparallel topology to an antiparallel-like structure.

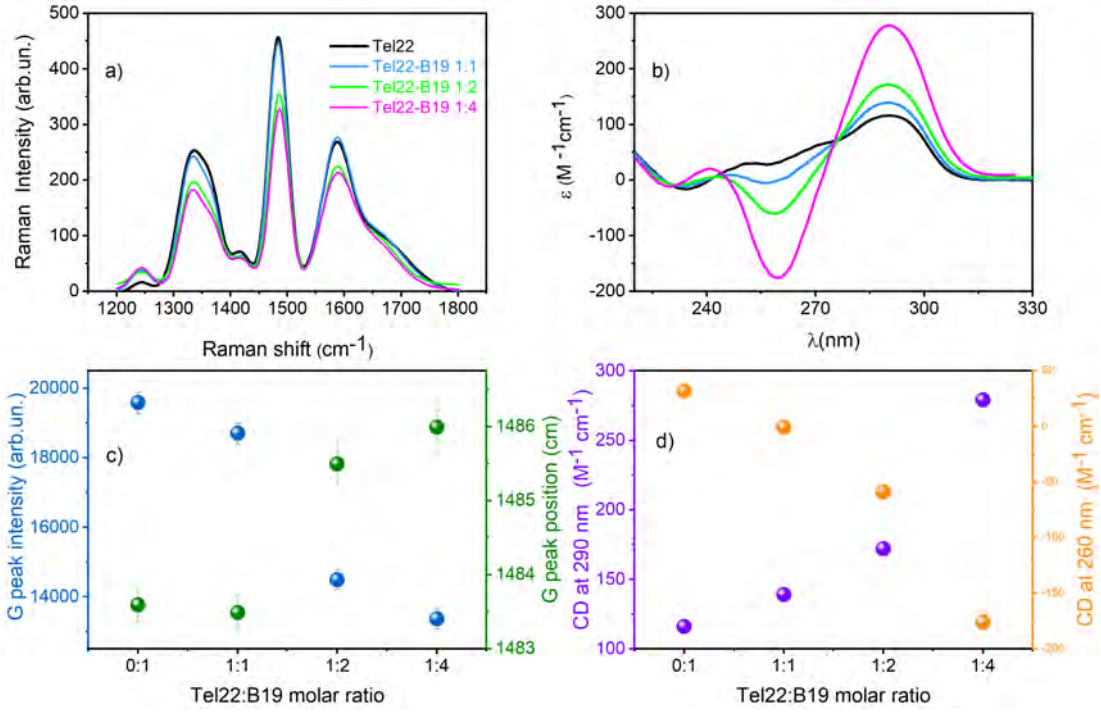

Figure 4.13: a) UVRR and b) CD spectra of Tel22-B19 at different stoichiometric ratios (1:0 black, 1:1 light blue, 1:2 light green, and 1:4 magenta). c) UVRR G-peak intensity (blue layer) and red-shift (green layer) as a function of Tel22-B19 molar ratio. d) CD intensity at 290 nm (violet layer) and at 260 nm (orange layer) as a function of Tel22-B19 molar ratio.

4.3.3 Thermal stabilisation: CD and UVRR

B19 is also an excellent G4 thermal stabiliser, as already demonstrated with other G4 sequences where the melting temperature was increased up to 33 °C after complexation [121, 133]. Therefore, CD and UVRR techniques were also employed to provide information on the Tel22 thermal stabilisation induced by B19. Figure 4.14 b), c), d) shows the Tel22-B19 at different molar ratios (1:1, 1:2, 1:4 respectively). As the concentration of B19 increases, the unfolding occurs at higher temperatures. Unfortunately, the unfolded state is not reached in the temperature range here investigated, i.e. from 24 °C to 84 °C, and a precise SVD analysis could not be performed. However, it is possible to observe that the three complexed samples seem to experience the same unfolding pathway: at 84 °C their CD feature is characterised by a maximum at 263 nm and a minimum at 240 nm, with rather high intensity. Figure 4.14 a) displays the normalised CD signals at 290 nm. Interestingly, we can observe that the unfolding process for all the complexes is not very cooperative. Furthermore, a two-state model cannot

describe the melting pathway. It is also evident that B19 strongly stabilises Tel22 structure.

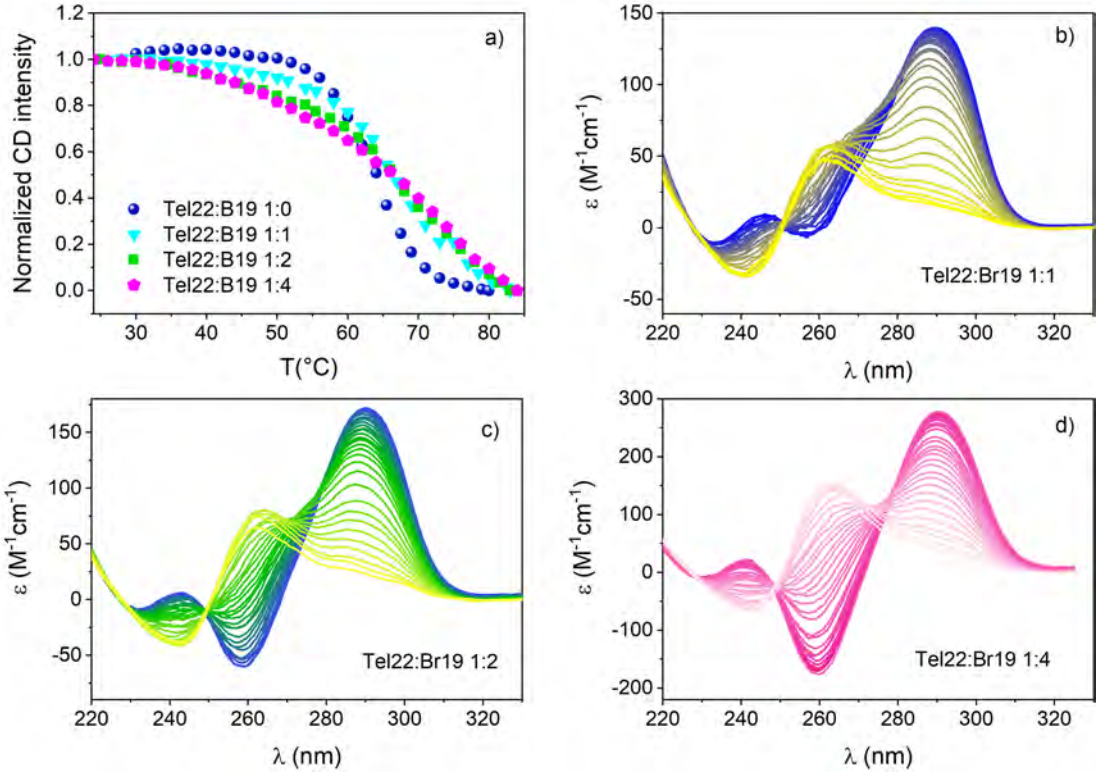

Figure 4.14: a) Normalised CD signal at 290 nm of Tel22-B19 at various molecular ratios. b) CD spectra as a function of temperature of Tel22-B19 1:1, c) Tel22-B19 1:2, and d) Tel22-B19 1:4.

The UVRR spectra as a function of temperature, which confirms the great ability of B19 in stabilising the quadruplex, are reported in figure 4.15 b) and c). During the unfolding, an evident enhancement of the whole UVRR spectra, the hyperchromic effect, in the G4 investigated range (from 1300 to 1800 cm^{-1}), is observed. This behaviour provides specific information on the unstacking of G-tetrads and, to quantify the stabilisation, the peak intensity at 1482 cm^{-1} was monitored (see figure 4.15 a)). This band is related to the guanine in-plane vibrations of the bending of C8-H and the stretching of N9-C8 and C8=N7 bonds [79, 88, 89]. From the data, it emerges that the higher the B19 concentration, the higher the melting temperature. The complex Tel22-B19 1:2 has a melting temperature at least 5 degrees higher than Tel22 alone.

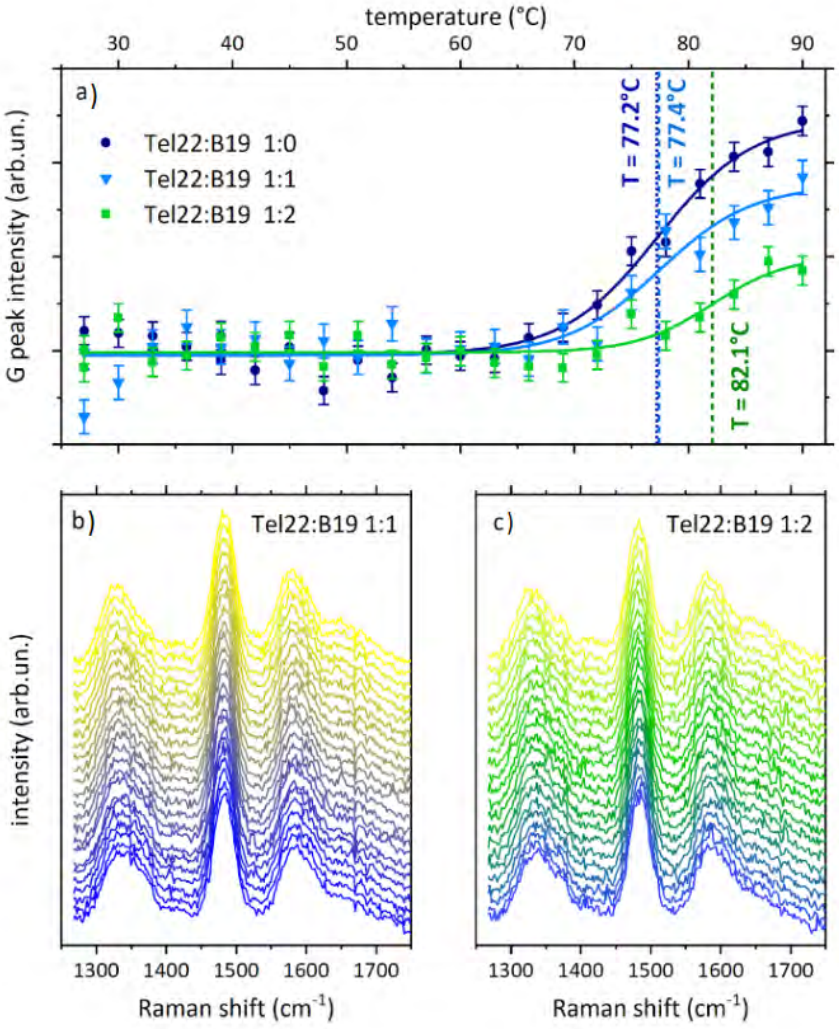

Figure 4.15: a) G peak intensity as a function of temperature. b) and c) UVRR spectra of Tel22-B19 1:1 and 1:2 respectively as temperature increases.

Chapter 5:

Ligand binding and irradiation drive Tel22 conformational changes

---

5.1 Introduction

In this chapter the results obtained using photosensitive ligands, TMPyP4 and DTE, complexed with Tel22 are shown. Dithienylethene derivatives are a family of photochromic compounds with aromatic functional groups, characterised by light-activated isomeric state reversible changes [134]. TMPyP4 is a highly studied G4-ligand, although the effect of complexation on telomeric G4 structure, its binding mode, and stoichiometry are still controversial, and influenced by various factors: the G4 sequence, the presence of flanking bases, the counterions, the crowding conditions and buffer ion concentration [125, 135–140]. Its ring probably binds with G4 tetrads through $\pi - \pi$ interaction with quite high affinity, even though TMPyP4 lacks selectivity with respect to the duplex DNA. Moreover, TMPyP4 porphyrin is renowned for its capacity to induce quadruplex formation in the promoter regions [141, 142], for its effects against a broad variety of tumor cells [143, 144], and for its telomerase inhibition upon binding to telomeric G4s [56].

The discussion of data analysis that follows refers to samples prepared at DNA concentrations in the order of tens of micromolar, while the high concentration regime will be discussed in the next chapter. TMPyP4 and DTE exposed to radiation activate different mechanisms, the former undergoes a chemical reaction, while the latter is subject to a photo-isomerisation. Here, it is demonstrated that these two processes generate a different effect on the structure and stability of the Tel22.

Light presents unmatched prospects since it can be used for biological applica-

tions due to its non-invasive nature and spatio-termporal precision. As a tunable parameter, in addition to light, temperature was also used to induce conformational changes. This research aims to propose a way in which temperature and light are employed to control the G4 structure and thermodynamics.

5.2 Irradiation set-up

Light irradiation was used to control the photochromic properties of DTE and TMPyP4 ligands. To maintain mechanical stability during illumination, thus ensuring that the samples were uniformly illuminated during the experiments, we used a homemade irradiation set-up. It consists of a collimated continuous LED source (ThorLabs) with a wavelength of 430/660 nm, a mobile support where the LED is placed, and a fixed cell holder. The solution of Tel22-drug was placed in a 1 mm thickness quartz cuvette 50 mm from the LED source, with the collimated light spot having a diameter of 25 mm and a power of 50 mW on the sample. When illuminating, the irradiation time (i.t.) is strictly correlated with the power density (power/area) of the laser spot on the sample, so it is essential to define all the best parameters for the measurements. Figure 5.1 shows the schematic set-up with the LED source at 430 nm. All the experiments were made in dark conditions.

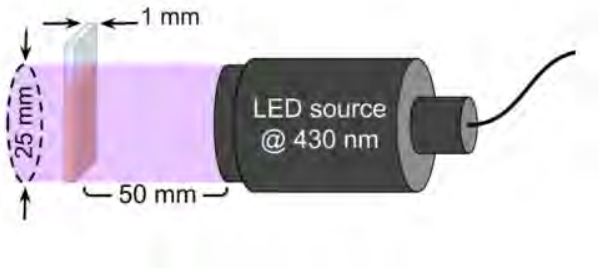

Figure 5.1: Schematic experimental set-up for irradiation.

Tel22-TMPyP4 was irradiated with the LED at 430 nm, since this wavelength is close to the porphyrin Soret band, which is attributed to the transition from the ground state to the second excited state. DTE is a photo-isomer that undergoes reversible conformational switching when it is irradiated with two different wavelengths. Low-energy visible light of 430/660 nm collimated continuous LED

was used to pass from the ring-open/closed isomer to the ring-closed/open isomer. Dark conditions were carefully maintained throughout the experiment in order to avoid unwanted partial photo-isomerisation episodes. Figure 5.2 shows the set-up and the sample irradiation with two different LEDs.

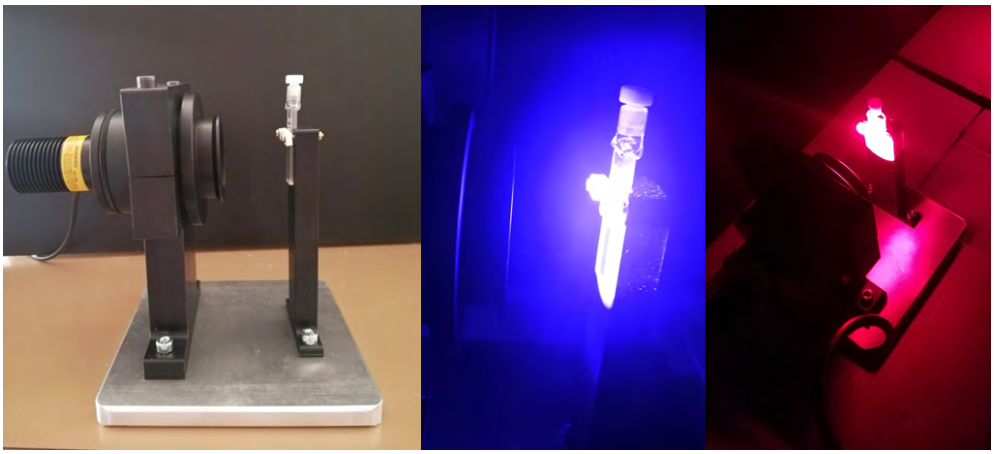

Figure 5.2: On the left, a picture of the homemade irradiation apparatus. On the right, a picture of the set-up with the two different wavelengths LED sources.

5.3 Sample preparation and characterisation

Tel22 was prepared as described in section 3.2. Porphyrin TMPyP4 was dissolved in buffer with 50 mM potassium phosphate 150 mM KCl 0.3 mM EDTA pH 7 (KPES). The porphyrin concentration was estimated from its absorption spectra considering the extinction coefficient $\epsilon_{422} = 2.26 \cdot 10^5$ $M^{-1}cm^{-1}$ at 422 nm [145]. In figure 5.3 a) the UV-Vis absorption spectrum of TMPyP4 and its chemical structure are shown. The Tel22 was complexed with TMPyP4 with a molar stoichiometric ratio DNA:ligand 1:2 and left at room temperature for two hours in dark conditions.

DTE was dissolved in DMSO in a stock solution of 10 mM. It was demonstrated that DTE is able to undergo reversible photo-switching between the open (1o) and closed (1c) isomers by alternate irradiation with blue and red light [61]. Figure 5.3 b) shows the UV-Vis absorption spectra of the two isomers and their chemical structure. First of all, the ligand photo-switching was tested in a buffer solution with 1% of DMSO to find the best irradiation conditions. The buffer used is the same KPES mentioned above. Figure 5.4 a) shows the time trial to achieve

the switch from the open to the closed configuration (1o)→(1c): therefore, 100 μM of DTE were irradiated with 430 nm at different exposure times. The switching (1o)→(1c) is accomplished in 10 minutes with blue radiation, whereas, to reach the complete isomer-switching of the reverse processes, (1c)→(1o), shown in figure 5.4 b), the sample was irradiated for 90 minutes with red light. In both cases, neat photo-isomerisation between the two forms of the ligand is reached as suggested by the presence of clear isosbestic points.

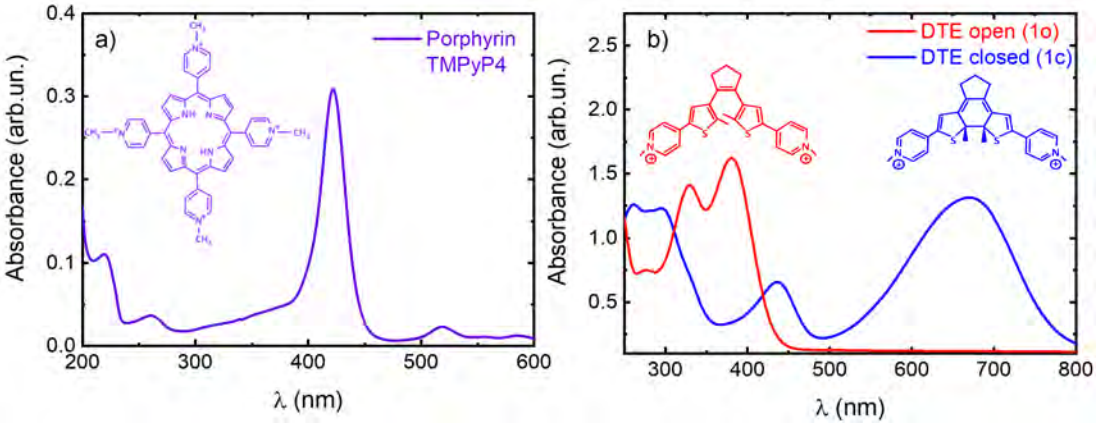

Figure 5.3: UV-Vis absorption spectrum of a) porphyrin TMPyP4 and b) DTE open (1o) and closed (1c) configuration.

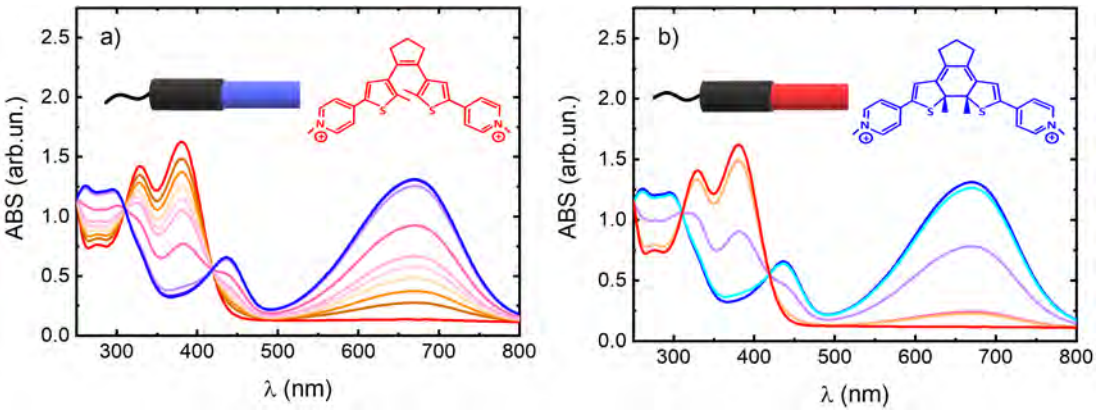

Figure 5.4: UV-Vis absorption spectra of a) DTE open to closed (1o)→(1c) and b) DTE closed to open (1c)→(1o) at different irradiation times. Spectra related to the process (1o)→(1c) were irradiated from 0 to 10 minutes with 430 nm, while those relating to (1c)→(1o) from 0 to 90 minutes with 660 nm light.

5.4 Titration

5.4.1 Tel22-TMPyP4

To estimate the best molar stoichiometric ratio for the binding affinity, UV-Vis absorption titration was performed keeping the TMPyP4 concentration fixed at 80 μM. The Soret band was monitored during the addition of Tel22, as shown in figure 5.5 a). The [DNA]:[ligand] ratios used were: 1:20, 1:10, 1:6.6, 1:3.3, 1:2.5, 1:2, 1:1, 1:0.66. The changes in the absorption intensity and the shift of the Soret band are shown in figure 5.5 b), where it is evident that the plot reaches a plateau when the molar ratio is 1:2 (Tel22:TMPyP4). Therefore, this ratio was the one selected for every measure.

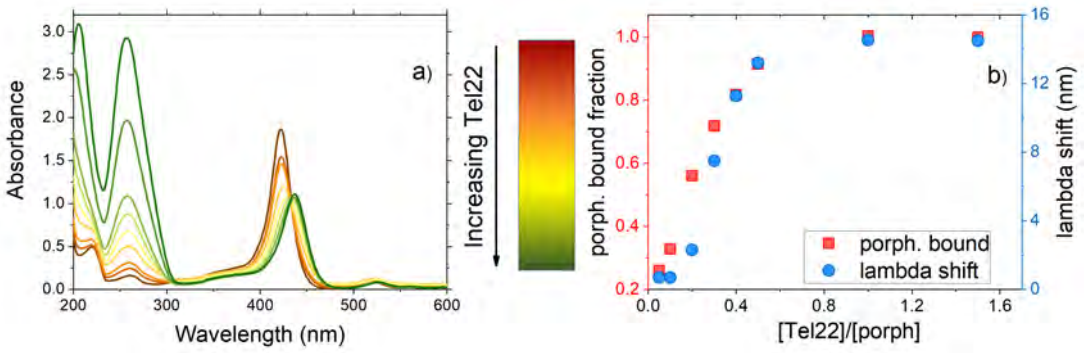

Figure 5.5: a) UV-Vis absorption spectra of TMPyP4 as a function of Tel22 concentration. b) Fraction of bounded TMPyP4 (red layer) and red-shift of the Soret band (blue layer).

To estimate the bound TMPyP4 fraction (C_b), a standard procedure [125] was employed, where $C_b = C - C_f$ was used, where C is the total porphyrin concentration, C_f is the concentration of the free molecule and it is defined as $C_f = C(1-\alpha)$ with $\alpha = (A_f - A)/(A_f - A_b)$, A_f and A_b are the absorbances of the free and fully bound TMPyP4 at the Soret maximum (422 nm) respectively, and A is the absorbance at 422 nm for any given point during the titration. The determined percentage of hypochromicity of TMPyP4 Soret band is approximately 62% and the red-shift of ~15 nm. The absence of an isosbestic point and the strong hypochromic and red-shift effect of the Soret band suggest that complexation of Tel22 with TMPyP4 involves multiple binding sites probably related to stacking and/or intercalation [136, 143].

5.4.2 Tel22-DTE

The same procedure was implemented for DTE in both its isomeric conformations. For the open configuration, the peak at $\sim$ 380 nm was followed, while, for the closed configuration, the peak at $\sim$ 670 nm was chosen. The ligand concentration was fixed at 60 μM while the G4 concentration was varied between 0 and 120 μM. In both cases, the increase of DNA concentration leads to a $\sim$ 15 nm red-shift and a hypochromic effect of 15-20%. These values suggest a possible intercalation mode, already reported in literature for DTE complexed with the human telomeric sequence Tel23, a base longer than Tel22 [61]. From the red-shift saturation plot, a stoichiometric ratio of 1:2 was chosen for the Tel22-DTE complex.

5.5 Irradiation as a trigger parameter

5.5.1 Photo-induced spectral changes of Tel22-DTE

To study the effect of complexation with the two different DTE isomers on Tel22 secondary structure, CD measurements were carried out. First, Tel22 was complexed with DTE (1o) and DTE (1c); the corresponding spectra are reported in figure 5.6 a). Both spectra show a small increase in the peak intensity at 290 nm and in the complex with (1o) configuration a rather strong decrease, with respect to Tel22 alone, of the shoulder at about 250 nm and 270 nm. This result is not far from what was obtained with Tel23 [61], suggesting a possible alteration of the G-tetrad in the Tel22-DTE (1o). Then, the Tel22-DTE (1o) complex was irradiated at 430 nm for 10 minutes, allowing the DTE ring closure, and restoring the Tel22 CD signal. This result is shown in figure 5.6 b), where the CD signal of Tel22-DTE (1c) (blue) and of Tel22-DTE (1c) (cyan) obtained afer ligand photoisomerisation overlaps, pointing out the capability of photo-controlling the Tel22 secondary structure. This result could have many implications in the field of G4 photopharmacological strategies and in nanotechnology.

However, in the next section, it will be shown that the CD spectrum of the sample irradiated with red light to allow photoisomerisation in the open configuration does not overlap with that of the original Tel22-DTE (1o). This result is in contrast with that already published by Galan et al. [61], where a complete

reversibility of the CD spectra was pointed out. Moreover, while in Ref. [61] a better performance of DTE against hybrid rather than antiparallel G4 topology is reported, here it is shown that the type of hybrid conformation (type 1 *vs* a mixture) plays a role in modifying the telomeric secondary structure.

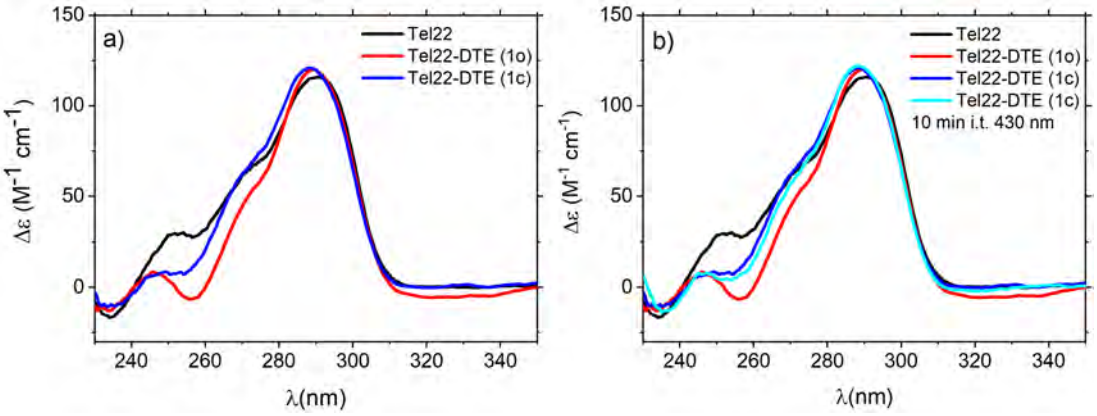

Figure 5.6: a) CD spectra of Tel22 (black), Tel22-DTE (1o) (red), Tel22-DTE (1c) (blue). b) Tel22-DTE (1o) (red), Tel22-DTE (1c) (blue), and Tel22-DTE (1c) i.t. 10 minutes 430 nm (cyan).

5.5.2 The curious case of Tel22-DTE in K^+ environment

As shown in the previous sections, DTE is a photo-reversible isomer; in literature it was reported that, once it is complexed with Tel22 in Na^+ and with Tel23 in K^+ environment, it is capable to photo-switch the G4 CD signal in a reversible way [61]. As for Tel22, the reversibility has also been successfully reproduced in our laboratory in Na^+ environment, while it was no longer valid in the K^+ one, as mentioned in the previous section. The CD and UV-Vis absorption spectra related to the process are shown in figure 5.7 a) and b) respectively. To better understand, in the middle panels of the figure 5.7, the description of each step is provided. First, the Tel22 was complexed with DTE (1o) and the corresponding CD spectrum is reported in red in panel 1, then it was irradiated with blue light allowing the DTE transition to the closed configuration (1c), which in turn made changes to the Tel22 secondary structure (blue spectra, panel 2). By irradiating the sample with red light, DTE returned to the open configuration (1o) and, theoretically, the CD spectrum (orange spectrum in panel 3) should also come back to the original signal. To complete the cycle, a second irradiation with blue light was carried out (light blue spectrum, panel 4). Figure 5.7 c) shows all the

CD spectra collected during the first cycle.

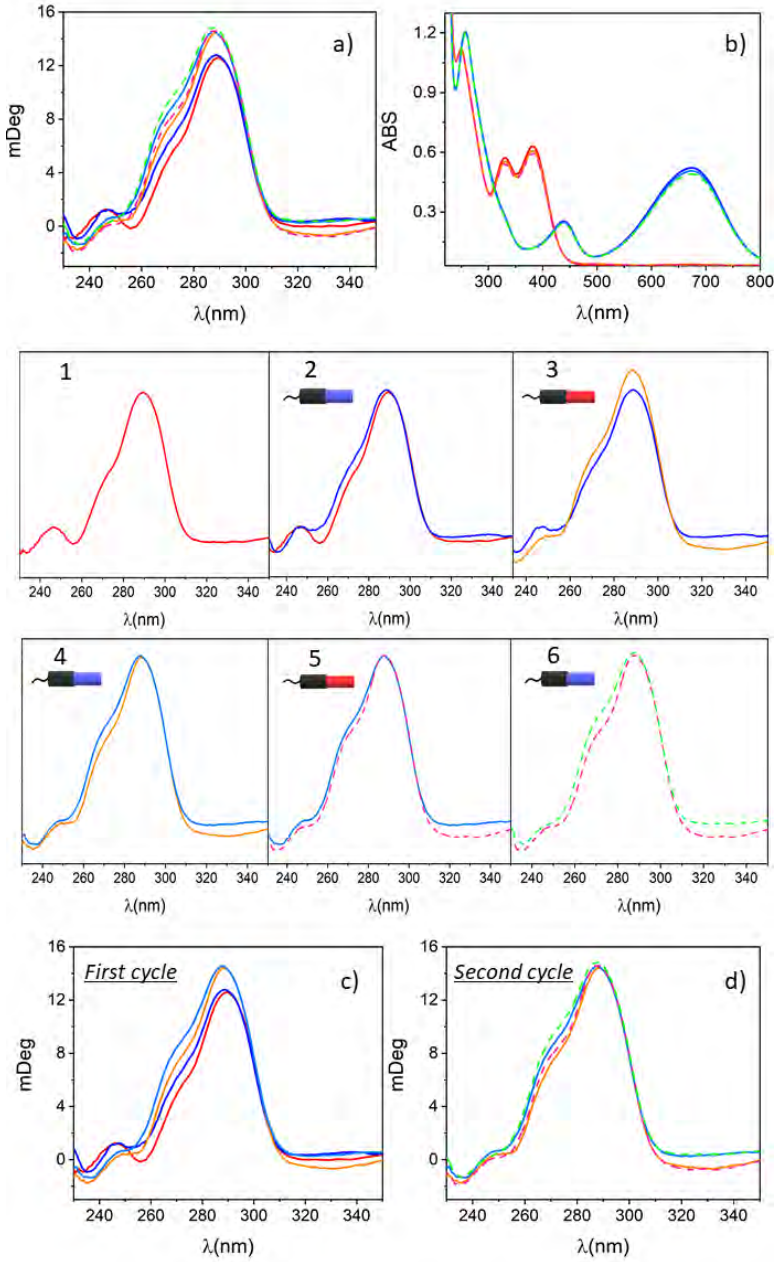

Figure 5.7: a) CD spectra and b) UV-Vis absorption of the photo-switching process. c) First and d) second cycle. In the middle, all the steps of the process are described. Tel22-DTE (1o) in red, Tel22-DTE (1c) in blue (i.t. 10 min 430 nm), Tel22-DTE (1o) in orange (i.t. 90 min 660 nm), Tel22-DTE (1c) in light blue (i.t. 10 min 430 nm), Tel22-DTE (1o) dashed pink (i.t. 90 min 660 nm),Tel22-DTE (1c) dashed green (i.t. 10 min 430 nm).

For reversibility, the orange and light blue signals should overlap the red and blue ones, respectively, but in both cases, the features at 290 nm and 264 nm have

a higher intensity. The process was repeated to obtain a second cycle (panels 5 and 6): even if there is no complete agreement, the signals almost come back (pink on orange and green on light blue). From the UV-Vis absorption spectra in figure 5.7 b) it is clear that irradiation successfully produces the DTE ring closure and aperture, therefore, even if the ligand photo-switching is reversible, some changes on Tel22 conformation can be identified. The reason why the first switch is not reversible provides the impetus for future investigation, starting by testing the complexation of DTE with other hybrid telomeric sequences.

5.5.3 Photo-induced Tel22-TMPyP4 structure destabilisation

CD technique was also employed to study the effect on Tel22 structure due to complexation with TMPyP4 and subsequent irradiation. Figure 5.8 a) shows the CD spectra of Tel22 and Tel22-TMPyP4 complexes. The first piece of evidence is that the peak at $\sim$ 270 nm, typical of the parallel-like G4 population, increases as a result of the complexation [86]. Then, the complex was irradiated with blue light (430 nm): under this condition, porphyrin can generate singlet oxygen thus oxidising guanines at the exterior face of the quadruplex scaffold.

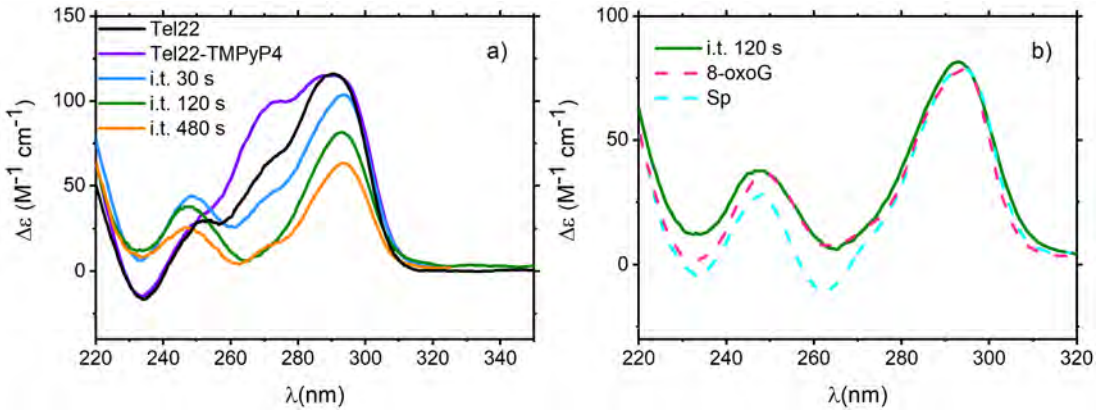

Figure 5.8: a) CD spectra of Tel22 (black), Tel22-TMPyP4 (purple), Tel22-TMPyP4 i.t. 30 s (light blue), Tel22-TMPyP4 i.t. 120 s (green), Tel22-TMPyP4 i.t. 480 s (orange). b) CD spectra of Tel22-TMPyP4 i.t. 120 s (green), 8-oxyG (pink), and Sp (light blue). The dotted CD spectra are taken from [146].

It was discovered that in G4 the major product of oxidation is the 8-oxo-7,8-dihydroguanine (8-oxoG), which is susceptible to further oxidation forming spiroiminodihydantoin (Sp) and guanidinohydantoin [147]. Tel22-TMPyP4

was irradiated at different exposure times, from 30 s to 480 s, and monitored by CD, the corresponding spectra are shown in figure 5.8 a). The progressive exposure produces an evident decrease in ellipticity while promoting conformational switching. The sample irradiated for 120 s has a CD signal that strongly resembles those of 5'-TAGGGTTAXGGTTAGGGTTAGGGTT-3' and 5'-TAGGGTTAGGXTTAGGGTTAGGGTT-3' telomeric DNA sequences, where damage at the GGG triad has been introduced. This similarity is apparent in figure 5.8 b). In the structural formula of the modified DNA samples, lesion X stands for 8-oxo-7,8-dihydroguanine (8-oxoG) or Sp products placed at 5' or 3' ends, respectively [146]. These folds show maxima at 295 and 245 nm, and a minimum at $\sim$ 265 nm, with a shape similar to the antiparallel-like topology. This result is highly likely because, upon exposure to radiation, porphyrin produces singlets oxygen ($^1O_2$) that preferentially oxidise guanines at the external quartets, generating numerous radicals and as the major products 8-oxoG and Sp [148].

The comparison in 5.8 b), between these oxidation products in G4s and Tel22-TMPyP4 irradiated for 120s, is particularly important since it enables localising the damage into Tel22 structure provoked by the irradiation-induced oxidation of the guanines. Furthermore, these measurements indicate that increasing the irradiation time up to 480 s results in the partial destruction of G4s until the tetrads are gradually unstacked. Indeed, the intensity of the Tel22-TMPyP4 i.t. 480 s spectrum is more than halved and the shape is almost all lost.

5.5.4 Irradiation of Tel22 and Tel22-DTE (1c) with blue light

Since the results obtained on Tel22-TMPyP4 complexes with and without irradiation are quite promising for applicative purposes [149–151], the first question that might arise is whether the conformational changes, which we have detected, are due to a combined effect of complexation with TMPyP4 and subsequent irradiation, or irradiation alone can still cause a modification in the quadruplex structure. To be sure that the irradiation with the blue light was not the only cause of the G4 topological modifications, the same exposition time was applied to Tel22 alone. Figure 5.9 a) shows that irradiation does not affect the Tel22 secondary structure, indeed after i.t. 480 s the G4 CD spectrum remains unvaried.

The second speculation could be wondering if other ligands with absorption at $\sim$ 430 nm could produce the same effect on Tel22 once irradiated. To answer this question, the complex Tel22-DTE (1c) was tested through the same procedure applied to Tel22-TMPyP4 samples. As in the case of Tel22, no change is observable in the CD spectrum shown in figure 5.9 b). These tests provide a positive control in favour of porphyrin as a G4 ligand with unique properties and interesting future perspectives.

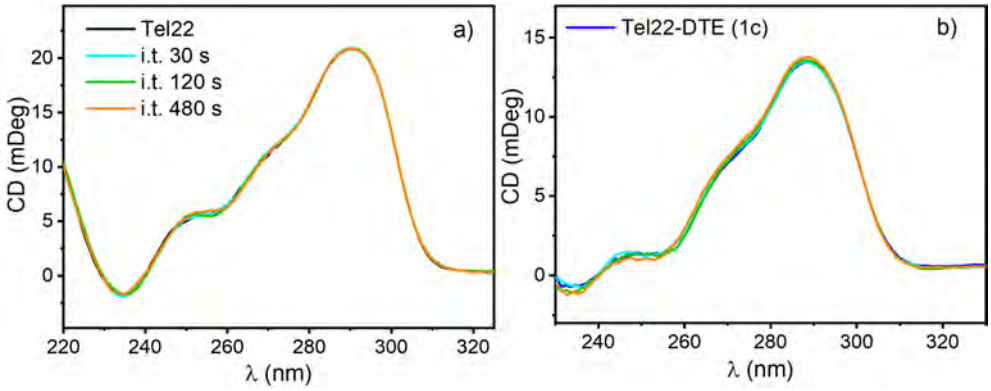

Figure 5.9: a) CD spectra of Tel22 (black), Tel22 i.t. 30 s (light blue), Tel22 i.t. 120 s (green), Tel22 i.t. 480 s (orange). b) CD spectra of Tel22-DTE (1c) (blue), Tel22-DTE (1c) i.t. 30 s (light blue), Tel22-DTE (1c) i.t. 120 s (green), Tel22-DTE (1c) i.t. 480 s (orange).

5.6 Temperature as a trigger parameter

In order to comprehend how switching between conformers might enable the regulation of telomere replication, and to design small molecules that specifically bind to various conformers, it is crucial to understand the thermodynamic factors that affect the relative stability of various conformers. To investigate the thermodynamic impact of ligands on the stability of Tel22, CD measurements were carried out by varying the temperature until unfolding was reached. The measurements were performed in steps of 2 degrees from 24 °C to 92 °C for DTE and from 24 °C to 84 °C for TMPyP4. Measurements upon thermal unfolding gave information on the stabilisation/destabilisation induced by the ligand complexation and/or the irradiation.

5.6.1 Tel22-DTE melting pathway

The melting pathway of Tel22-DTE (1c) and Tel22-DTE (1o) was monitored through CD experiments, shown in figure 5.10 a) and c) respectively. The whole process was analysed by means of the SVD method. In both cases, an intermediate state between folded and unfolded was detected, and the three-step process was described by a sequential unfolding model (F⇌ I ⇌ U). A global nonlinear least-squares fitting on the amplitude vectors obtained from the SVD returned the values to reconstruct the spectra of the significant species (figure 5.10 b) and d)) and to derive the thermodynamic parameters presented in table 5.1.

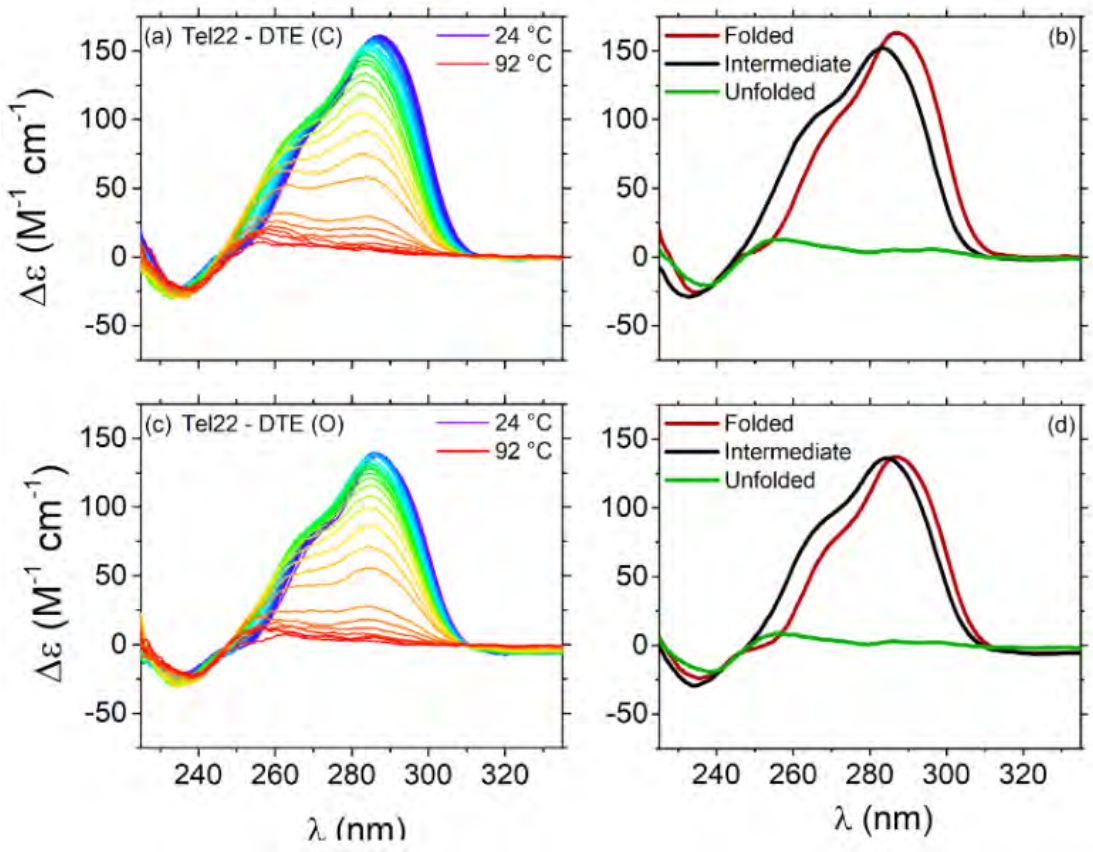

Figure 5.10: CD melting spectra of a) Tel22-DTE (1c) and c) Tel22-DTE (1o). Reconstructed spectra of significant species b) for Tel22-DTE (1c) and for d) Tel22-DTE (1o).

For both cases, the melting temperature (T_{m2}) is, within error, 3-4 degrees higher than that of Tel22 alone. Interestingly, both Tel22-DTE (1c) and (1o) experienced at ∼ 42-45 °C a very similar intermediate state, characterised by a shift and a decrease in the peak at ∼ 290 nm and an increase of the shoulder at

$\sim$ 265 nm. The unfolded states have a typical CD feature of disordered polynucleotide, with a very weak signal. Enthalpies of both steps are smaller in the case of Tel22-DTE (1o) compared with Tel22-DTE (1c), probably due to the fact that the G-tedrads, in the complex with DTE in open configuration, are partially distorted, as suggested by [61].

Table 5.1: Thermal melting parameters for Tel22-DTE (1o) and Tel22-DTE (1c) obtained through a global fit and SVD.

	Tel22-DTE (1o)	Tel22-DTE (1c)
T_{m1} (°C)	42± 1	45 ± 1
T_{m2} (°C)	73 ± 1	72 ± 1
dH_1 (kcal mol^{-1})	-23±2	-30±3
dH_2 (kcal mol^{-1})	-57±3	-62±3

Control experiments revealed significant thermal cyclo-reversion and probably for this reason the complexes with the two isomers pass through a similar melting pathway. A schematic representation of the unfolding pathway is shown in figure 5.11.

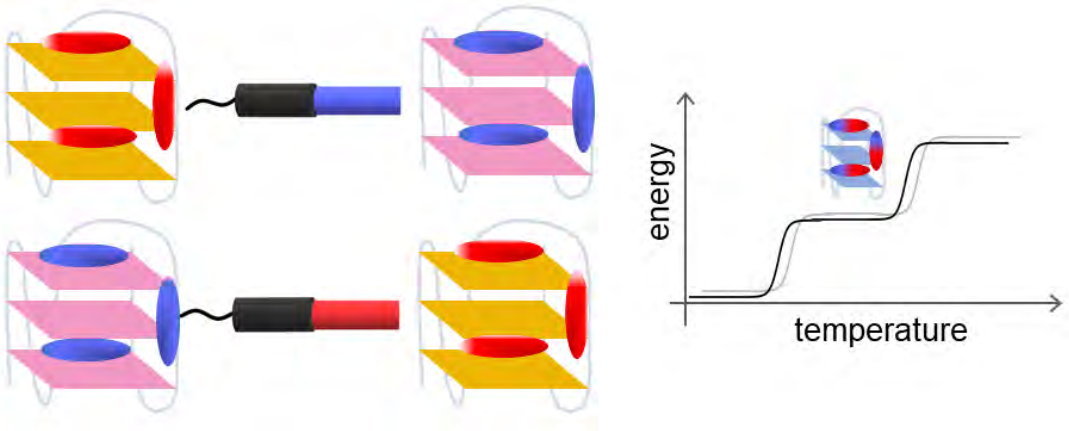

Figure 5.11: Schematic representation of the melting pathway of Tel22-DTE (1o) and Tel22-DTE (1c).

5.6.2 Tel22-TMPyP4 melting pathway

It was observed that guanine oxidation alters the folding of telomeric quadruplexes in KCl solution [146]. Tel22 melting pathway and thermostability are

affected by the interaction with TMPyP4 and subsequent irradiation of the complex. To quantify the complexation and the oxidative effect, the features of the Tel22-TMPyP4 complex ellipticity were monitored as a function of temperature both for the non-irradiated sample and for those exposed to blue light, i.t. 30 s, 120 s, and 480 s. All the corresponding thermal denaturation profiles are displayed in figure 5.12.

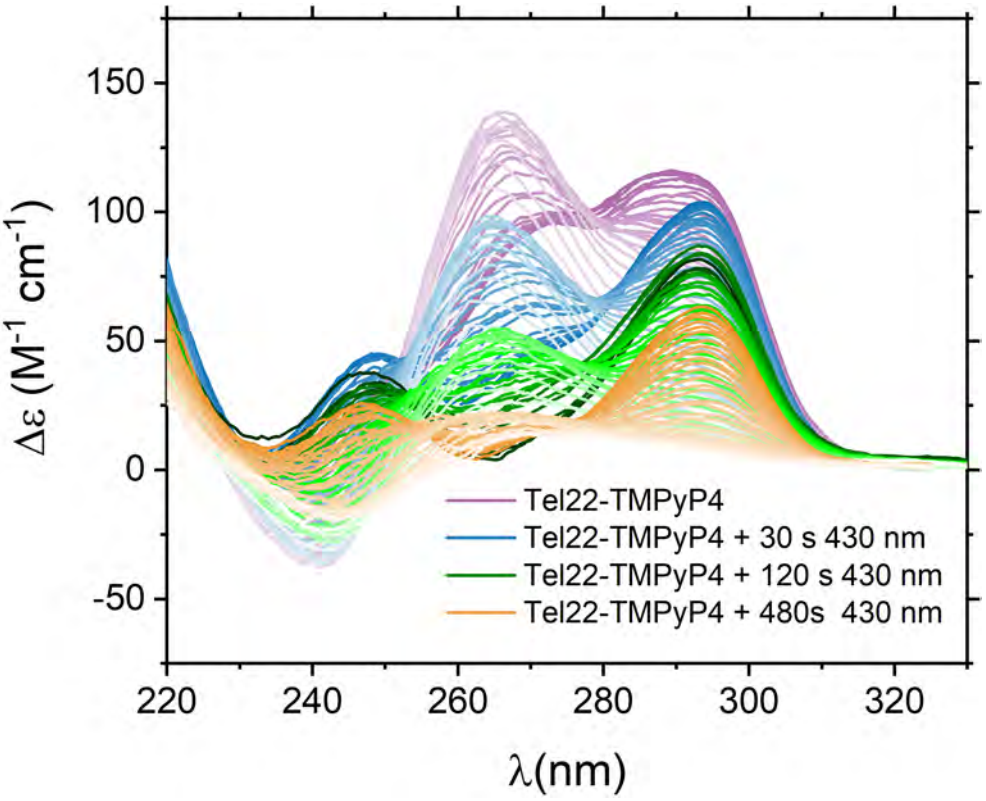

Figure 5.12: Thermal denaturation profiles of Tel22-TMPyP4 (purple), Tel22-TMPyP4 i.t. 30s (light blue), Tel22-TMPyP4 i.t. 120 s (green), and Tel22-TMPyP4 i.t. 480 s (orange) recorded with CD.

The melting data were analysed through the SVD method, and a three-step pathway process was found (F$\rightleftharpoons$ I $\rightleftharpoons$ U). A global nonlinear least-squares fitting on the SVD amplitude vectors allowed us to extract the coefficients needed to reconstruct the spectral features of significant structures of the unfolding process and their relative populations. The obtained thermodynamic parameters are reported in table 5.2, while the reconstructed significant species and their relative concentration as a function of temperature in figure 5.13.

In the presence of TMPyP4, the melting temperature of Tel22 (T_m= 69 °C [79]) is increased by $\sim$ 3 °C, as well as in the case of Tel22-TMPyP4 irradiated

for both 30 s and 120 s. This differs from what occurs in Tel22-TMPyP4 sample irradiated for 480 s, where the melting temperature decreases by 2 °C with respect to the unbound Tel22. As mentioned above, in this case, the DNA begins to lose its structure and the complex becomes thermodynamically more unstable. Indeed, in addition to the decrease in the melting temperature, a reduction in the enthalpy between each step is observed.

Table 5.2: Thermal melting parameters for Tel22-TMPyP4 samples obtained through a global fit and SVD.

	Tel22-TMPyP4	i.t. 30 s	i.t. 120 s	i.t. 480 s
T_{m1} (°C)	50± 1	51.5 ± 0.8	50 ± 1	50± 1
T_{m2} (°C)	71.5 ± 0.7	72.5 ± 0.8	71± 1	66± 2
dH_1 (kcal mol^{-1})	-26±2	-26±2	-23±2	-21± 3
dH_2 (kcal mol^{-1})	-59± 3	-51±4	-48±3	-42± 3

By monitoring the whole melting path, it was observed that, for Tel22-TMPyP4, Tel22-TMPyP4 i.t. 30 s and 120 s, the intermediate states, reported in figure 5.14, although of gradually decreasing intensity, are not very dissimilar in shape, and resemble a triple helical structure [68, 152]. The triplex structure was shown to be a possible form of intermediate state for Tel22 prepared in a different buffer than that used in the present study [68]. Interestingly, the triplex was suggested to be a possible pre-unfolding step for telomeric sequences [153–157]. Moreover, MD simulations revealed that triplex are energetically feasible structures [158]. Biophysical techniques and molecular dynamics have revealed the formation of a triplex structure studying the d[TTA$(GGGTTA)_3$] sequence [152]. Its CD signature is similar to that of the intermediate states obtained from Tel22-TMPyP4 samples.

Furthermore, the complex irradiated for 480 s shows an intermediate state with a few differences from the others. In this case, the intermediate shape resembles that of a triplex with an oxidised guanine in the central tetrad [146], as reported in in figure 5.14. This suggests that, while complexes irradiated for less time only oxidise the external tetrads, those irradiated for 480 s begin to oxidise even the guanines in the central tetrad. A schematic representation of the unfolding pathway is shown in figure 5.15.

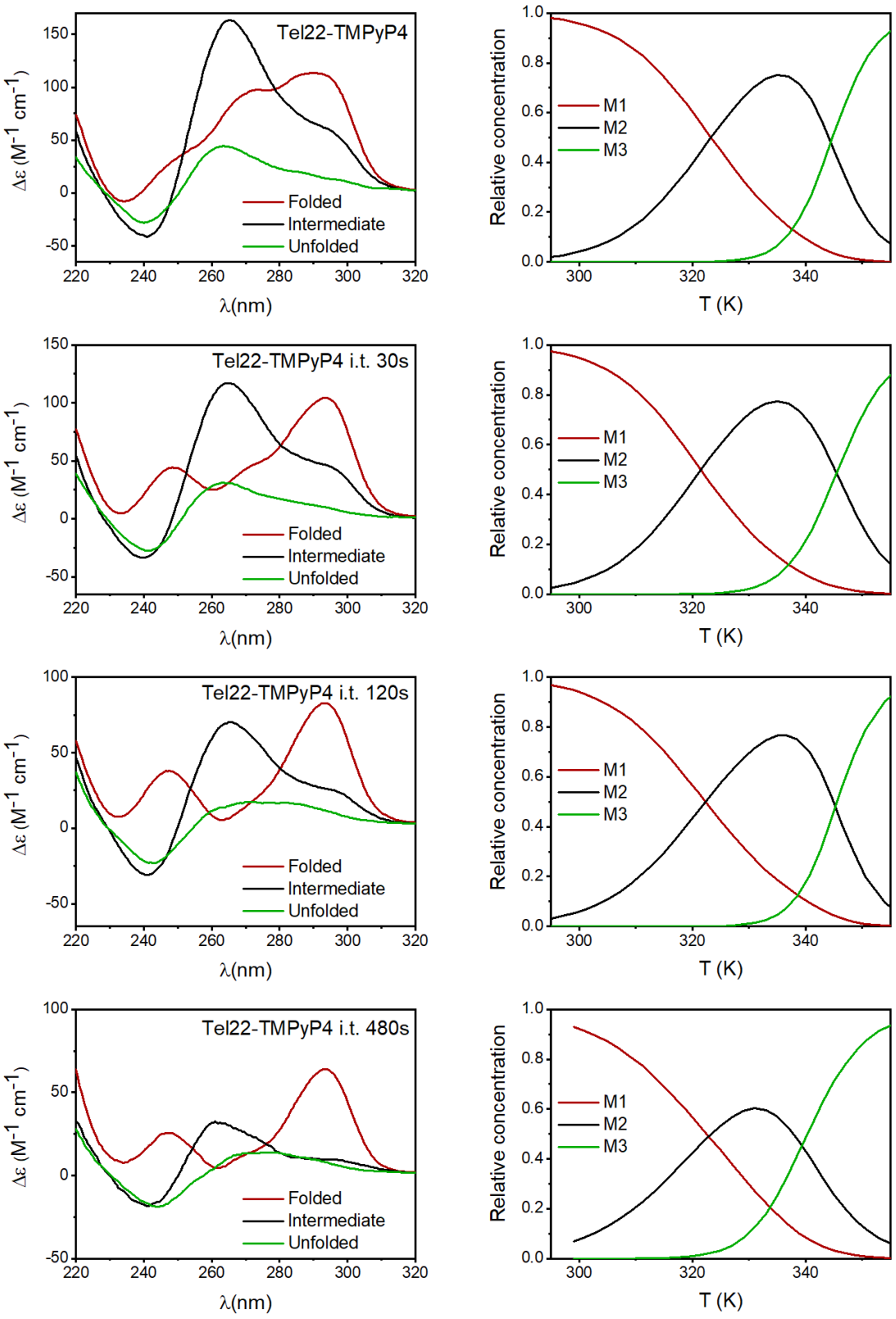

Figure 5.13: On the left the reconstructed significant species and on the right their relative concentrations as a function of temperature.

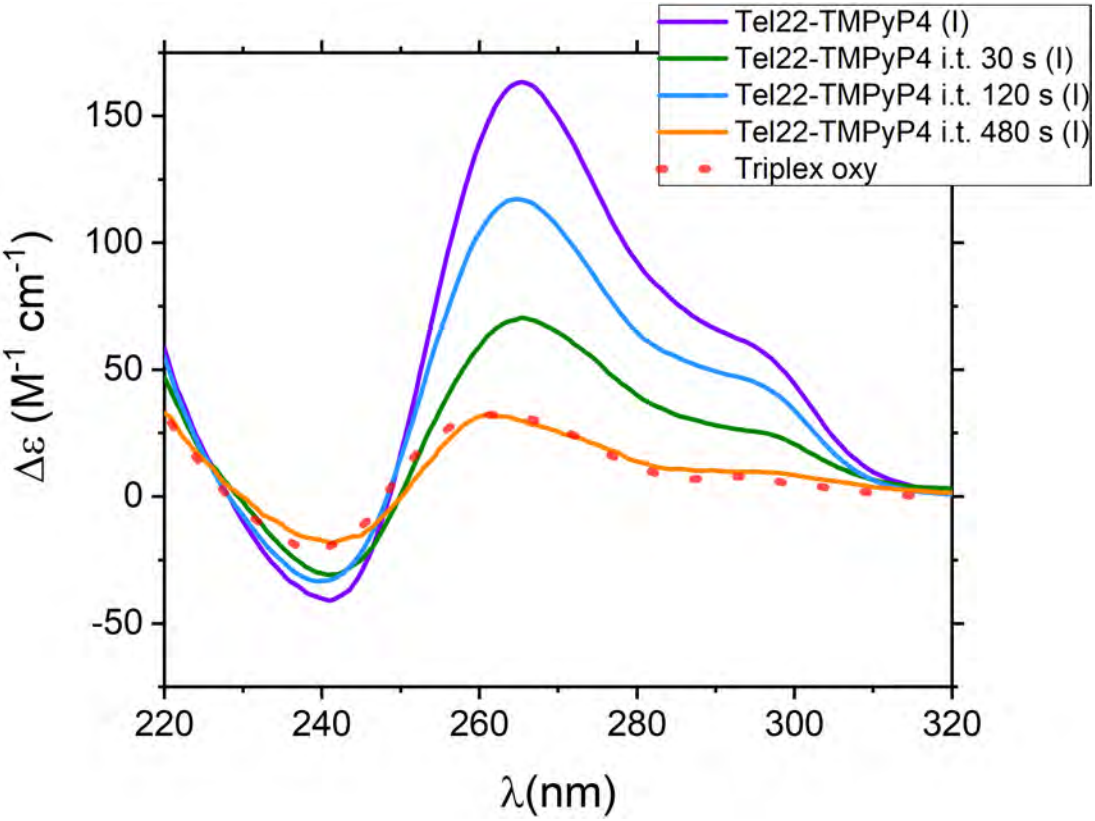

Figure 5.14: CD spectra of the intermediates reconstructed via SVD. Tel22-TMPyP4 in purple, Tel22-TMPyP4 i.t. 30 s in light blue, Tel22-TMPyP4 i.t. 120 s in green, Tel22-TMPyP4 i.t. 480 s in orange, and in dashed orange line a triplex that is a result of telomeric G4 with oxidised guanine in the central tetrads (CD signal taken from [146]).

Figure 5.15: Schematic representation of the melting pathway of Tel22-TMPyP4 complexes.

Chapter 6:

Complexation and irradiation promote dimerisation of Tel22 at high concentration

---

6.1 Introduction

This chapter mainly contains the results reported in the paper published in 2021 [86]. On the basis of the findings presented in the previous chapter, it was decided to use a structure-based strategy, integrating complementary techniques, such as circular dichroism and small-angle scattering, to deeply investigate the Tel22 structural changes induced by the porphyrin TMPyP4 and by light irradiation. These two methods look at structural differences on a distinct spatial scale: SAS is sensitive to the modifications induced on the global protein/DNA structure, such as the changes in shape, size, and oligomerisation state, while CD is powerful to study the secondary structure of biological materials. The purpose is to find a possible link between the changes on the secondary and the quaternary structure when Tel22 interacts with TMPyP4 before and after irradiation with blue light. All the experiments presented in this chapter were performed at $\sim$ 500 μM DNA concentration. Unexpectedly, the results show a very different behaviour compared to those obtained at lower concentrations, which could result from the fact that Tel22 is a really polymorphic structure and its secondary structure is highly concentration-dependent.

6.2 Materials and methods

Tel22 was dissolved in 50 mM K-phosphate buffer, 150 mM KCl, 0.3 mM EDTA, pH 7. To have the same CD and SAS experimental conditions, measurements

were carried out at 500 μM Tel22 concentration, both alone and in the complex with 1 mM TMPyP4. Circular dichroism measurements were performed with 0.1 mm quartz cuvette, and the irradiation procedure was the same as described in the previous chapter. The small-angle X-ray scattering was performed at the SWING beamline at the synchrotron SOLEIL (Paris). To be sure that SAXS data were not affected by X-ray radiation, complementary small-angle neutron scattering measurements were carried out. After the acceptance of a proposal, SANS measurements were performed at the diffractometer D22 at ILL (Institut Laue-Langevin, Grenoble). The following samples were measured: Tel22, Tel22-TMPyP4, and Tel22-TMPyP4 with different 430 nm irradiation times (i.t.) (30 s, 60 s, 120 s, 240 s, 480 s). A schematic view of the irradiation set-up is presented in figure 6.1.

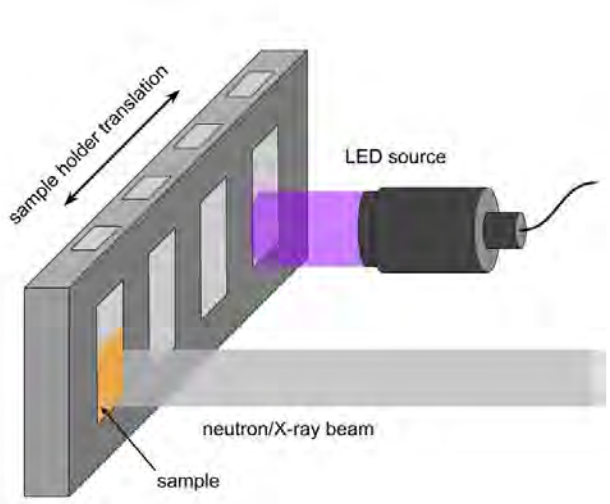

Figure 6.1: Sall-angle scattering irradiation set-up. Figure adapted from [86].

For SAXS, a 1.5 quartz capillary was used and positioned at 90° to the X-ray beam direction, the sample-detector distance was 2 m. X-ray wavelength was 1.03 Å, around 20 images were collected for each sample and 990 ms exposure time was set. An incident wavelength of 6 $\pm$ 0.6 Å was used at D22 beamline with two different sample-detector distances, namely 1.5 m and 5.6 m. These conditions allowed a Q range between 0.01 $Å^{-1}$ and 0.5 $Å^{-1}$. SANS data were reduced using Grasp software (developed by C. Dewhurst) and scaled to absolute intensity. The buffer was not deuterated since for the DNA the contrast is better in H_2O than D_2O, the incoherent background was removed attentively.

6.3 Circular dichroism reveals topology changes

CD measurements were performed to characterise the Tel22 secondary structure changes produced by complexation with TMPyP4 and irradiation with blue light. Figure 6.2 shows that the major secondary structure rearrangement is induced by complexation, while light irradiation increases the effect that occurs at the transition from free to bound.

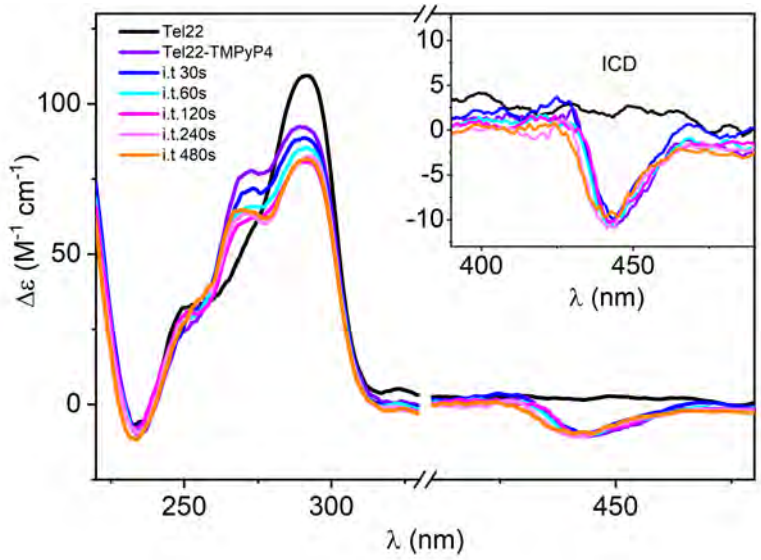

Figure 6.2: CD spectra of Tel22 (black) and Tel22-TMPyP4 at different irradiation times. Figure from [86].

The interaction of Tel22 and TMPyP4 is also confirmed by the well-visible induced CD signal (iCD) around 440 nm, shown in figure 6.2. Porphyrin is achiral but its interaction with other biomolecules can break the central symmetry and generate iCD in the Soret band region. The CD spectrum of the complexed sample has a shape very similar to that obtained at lower concentrations, with a shoulder rising around 270 nm. However, while at lower concentrations irradiation promotes partial destruction of G-tetrads, in these conditions there are just small secondary structure rearrangements. To estimate these changes a method proposed by Chaires' group [77] was used, which employs singular value decomposition and principal component analysis on 23 CD spectra of G-quadruplexes of known structure. This tool is able to quantitatively extract the secondary structure content just from G4 experimental CD spectra.

Each spectrum is decomposed in the following fractions: *anti-anti*, *syn-anti*,

or *anti-syn* conformations, diagonal or lateral loops, and other conformations. In the last component double chain-reversal loops or terminal nucleotides that may or may not be stacked are comprehended, this fraction will be called *ext*. In table 6.1 the results of the decomposition are shown.

Table 6.1: Secondary structural elements percentage obtained from the methodology reported in [77].

Sample	*anti-anti*	*syn-anti*	*anti-syn*	*digonal*	*ext*
Tel22	14.60	15.66	12.42	45.97	12.34
Tel22-TMPyP4	17.19	15.01	12.7	37.10	17.64
i.t. 30 s	17.97	15.06	12.56	36.78	16.64
i.t. 60 s	17.88	14.55	12.29	36.31	17.97
i.t. 120 s	18.21	14.57	12.62	35.95	17.66
i.t. 240 s	18.17	14.01	12.02	36.13	19.67
i.t. 480 s	18.02	13.51	11.40	36.17	19.89

Although the data are in general well fitted by this method, the fit residues of the irradiated samples have a shape that suggests the presence of structured elements formed after light exposure. The non-perfect agreement between the experimental and theoretical curves of Tel22-TMPyP4 sample irradiated for 60 s is shown in figure 6.3 a).

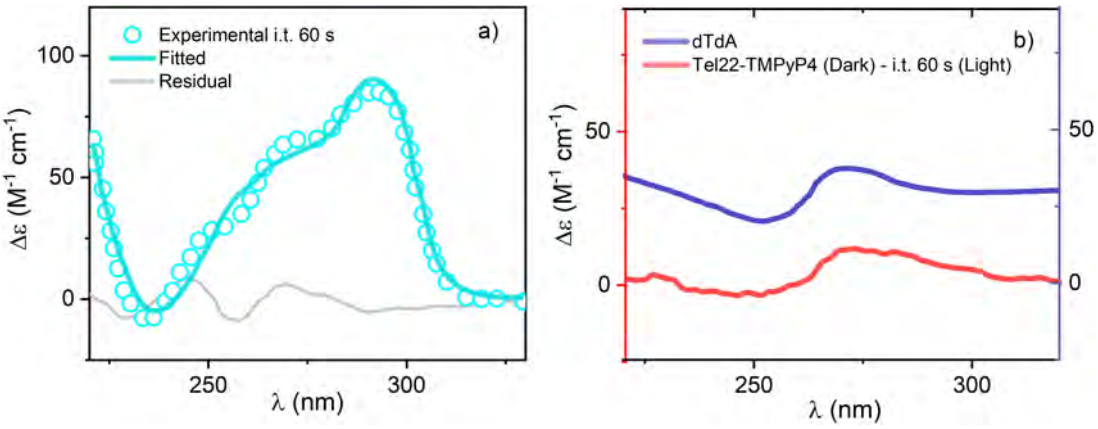

Figure 6.3: a) Experimental CD spectra of Tel22-TMPyP4 sample irradiated for 60 s (circles), fit used to extrapolate the five secondary structure components (cyan line), and residues (grey line). b) CD difference spectra between the Tel22-TMPyP4 dark/light i.t. 60 s (red line) and CD spectra of dTdA oligonucleotide (blue line) (spectrum taken from [159]). The figure is taken from [86].

It is worth noting that the CD difference spectra between the Tel22-TMPyP4 dark/light i.t. 60 s resembles that of the CD profile of the dTdA oligonucleotide,

comparison in figure 6.3 b). These speculations could suggest that light could cause rearrangements or breaks in the extremal parts of the Tel22.

6.4 Dimeric structures revealed by SAS

SAXS and SANS were employed to get information on structural changes, due to the effect of porphyrin complexation before and after irradiation at 430 nm, on a larger scale. The spectra acquired with these two techniques show the same behaviour, as shown in figure 6.4.

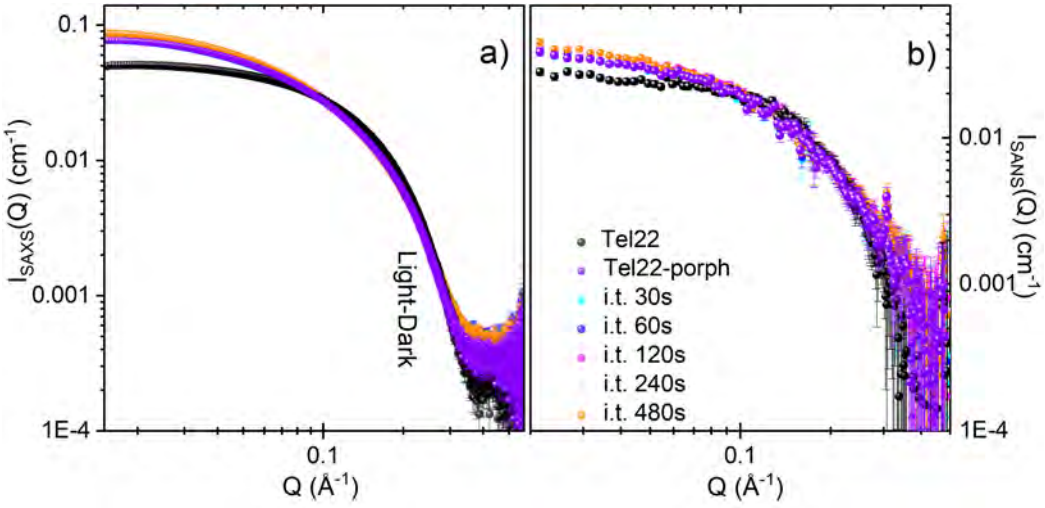

Figure 6.4: a) SAXS and b) SANS profiles of Tel22 (black), Tel22-TMPyP4 (violet) before and after irradiation of the complex with 430 nm light for 30 s (cyan), 60 s (blue), 120 s (magenta), 240 s (pink), and 480 s (orange). Figure adapted from [86].

In agreement with CD results, the major rearrangement is due to complexation. The first approach to check the biomolecule compactness is to look at the Kratky plot, which gives qualitative information on the flexibility and/or degree of unfolding. Figure 6.5 shows the Kratky plot derived from Tel22, and complexed sample without and with irradiation. They present a bell-shaped (Gaussian) peak with a well-defined maximum, typical of globular objects, while highly flexible or unfolded ones reveal a plateau at high Q. This also suggests that irradiation does not lead to degradation in the samples.

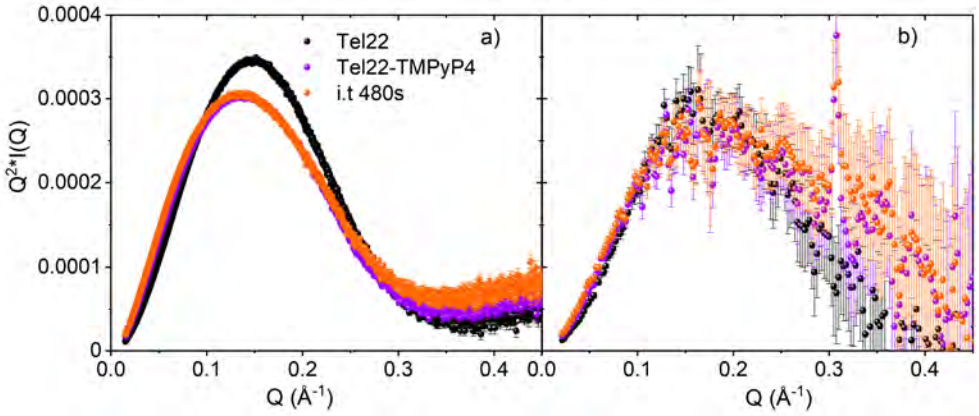

Figure 6.5: a) SAXS and b) SANS Kratky plot of Tel22 (black), Tel22-TMPyP4 (purple), i.t 480s (orange). Figure from [86].

6.5 Model-free analysis

The trend and the shape of the spectra of complexed samples in figure 6.4 suggest the presence of elongated structures. This hypothesis is corroborated by results obtained from independent model approaches that will be discussed in this section. First of all, from the Guinier analysis, it is possible to extrapolate the radius of gyration (R_g) and the scattering intensity at Q $\approx$ 0 (I(0)). Both parameters are proportional to the size of the system.

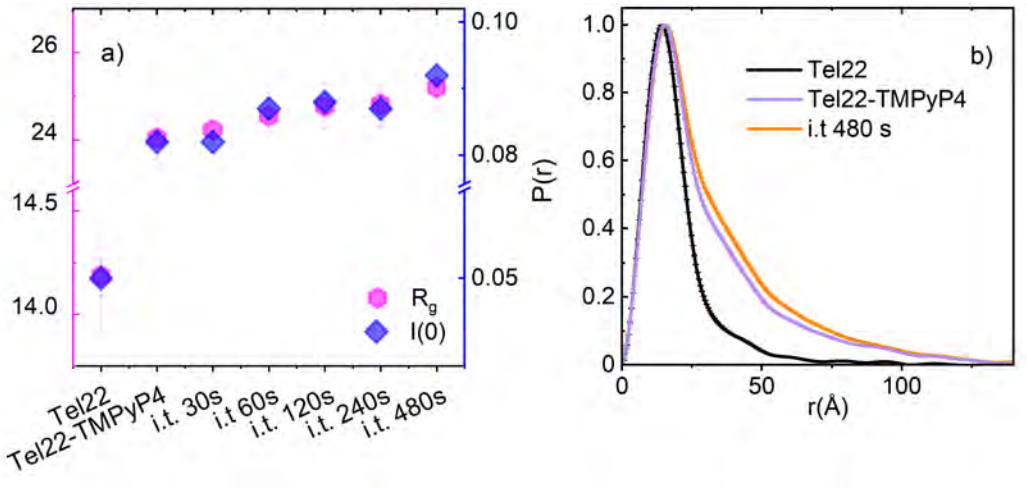

Figure 6.6: a) R_g (Å) (pink axis) and I(0) (cm^{-1}) (blue axis), obtained by the Guinier analysis. b) Pair-distance distribution P(r) functions from SAXS data for Tel22 (black), Tel22-TMPyP4 (purple), and Tel22-TMPyP4 after 480 s irradiation (orange). Figure adapted from [86].

The values obtained from the complexed and illuminated samples are much

larger values (nearly double) compared to those extracted from the Tel22 alone. Tel22 has $R_g \approx 14$ Å while the samples of Tel22-TMPyP4 in both dark and light conditions have $R_g \approx 24$ Å (see figure 6.6 a)).

Another plot really sensitive to the particle shape and size is the pair-distance distribution (P(r)), which was extracted from the GNOM program in the ATSAS package [70]. Figure 6.6 b) shows a narrow single feature on the P(r) of Tel22, suggesting a monomeric state. Complexation induces the appearance of a shoulder at about 40 Å, which increases upon irradiation. The maximum dimension in the system (D_{max}) can also be extrapolated from this discussion: Tel22 has $D_{max} = 65$ Å, while Tel22-TMPyP4 has $D_{max} = 108$ Å in dark condition, then becoming $D_{max} = 110$ Å after irradiation of 480 s.

An estimate of the molecular volume of the various samples can be extracted from the scattering intensity using the Porod invariant through the following equation:

$$I_p = \int \frac{d\Sigma}{d\Omega} Q^2 \, dQ, \tag{6.1}$$

and the particle volume is given by:

$$V_p = \int 2\pi \frac{I(0)}{I_p}, \tag{6.2}$$

The molecular volume of Tel22 is $V_p = 5 \cdot 10^3$ Å^3, while the Tel22-TMPyP4 is $V_p = 8 \cdot 10^3$ Å^3, the complex has almost doubled its volume with the respect to the unbound sample, then it increases with irradiation until it reaches a plateau.

All of these results suggest that the complexation with TMPyP4 induces Tel22 dimerisation. In table 6.2 all the values obtained from the model-free analysis are shown.

6.6 Form factor modelling

To better quantify the Tel22 structural changes upon complexation and irradiation, the SAXS (SANS) experimental form factor of Tel22 was fitted with the cylinder form factor, with radius of 10 ±1 Å (9 ±1 Å) and height 36 ± 1 Å (27 ± 1 Å). As it is known, the Tel22 is in a monomeric state in these conditions,

therefore this cylinder represents the monomeric unit. This theoretical form factor is not able to well fit the samples with the porphyrin, which were analysed using a mixture of monomers and dimers, the latter represented by two adjacent cylinders of radius of 10.3 ± 0.5 Å (9 ± 1 Å) and height 80 ± 1 Å (51 ± 2 Å). It is worth noting that the electron density contrast between G4 and buffer, inclusive of the hydration layer and the ion cloud, is detected by SAXS and not by SANS [91, 92]. As a result, the higher structural values obtained by SAXS can be justified.

Figure 6.7 shows the experimental SAXS profiles for Tel22 fitted by a cylindrical form factor compatible with the monomer size and Tel22-TMPyP4 with its theoretical curve obtained by the fitting procedure in terms of a mixture of monomers and dimers [79, 87]. The monomeric and the dimeric components fitted for Tel22-TMPyP4 before and after 480 s of irradiation are represented in figure 6.9. After binding, the transition from monomers to a mixture of monomers and dimers occurs both in dark and light conditions. The fitting procedure revealed that the complex is composed of 60% of dimers and this percentage progressively increases with exposure times reaching a plateau at ∼75%.

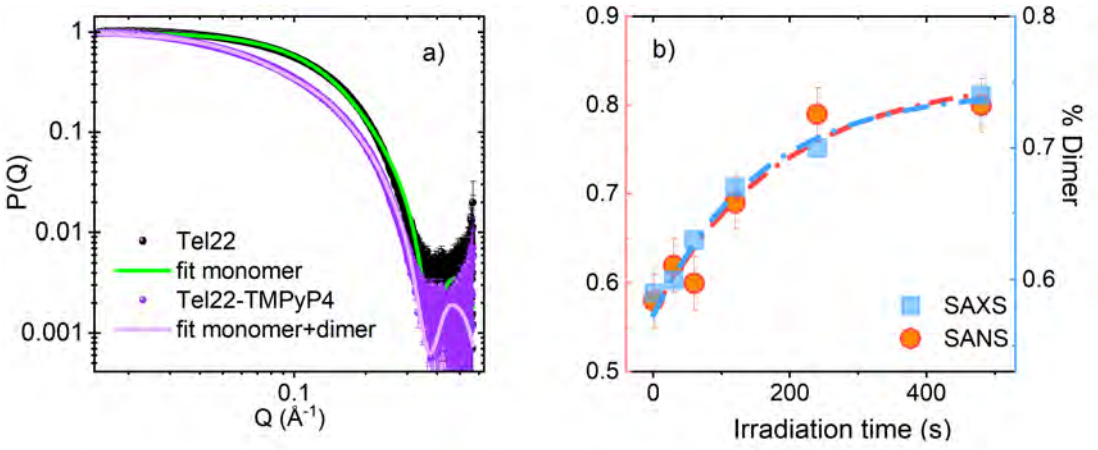

Figure 6.7: a) Experimental and theoretical SAXS profiles for Tel22 and the Tel22-TMPyP4 complex. The Tel22 spectrum (black) is reproduced by a monomer (green), while the Tel22-TMPyP4 (violet) form factor is described by a mixture of monomers and dimers (pink). b) Percentage of dimers over exposure time. The exponential growth of the amount of dimers is shown with dashed line. Figure adapted from [86].

Despite the differences in sensitivity between SAXS and SANS, the overall behaviour of the percentage of dimers is the same, confirming that the process is reproducible. Moreover, an exponential law was used to fit the trend of dimer

proportion as a function of irradiation time, providing the characteristic rising rate of $1/160$ s^{-1}. Within the error, this result is in agreement with a model-free analysis treatment, where the same parameter was obtained.

Table 6.2: Radius of gyration derived from the Guinier plot and percentage of dimers.

Sample	R_g (Å) (SAXS)	R_g (Å) (SANS)	V_p ($\cdot 10^3$) (Å^3)	% dimer (SAXS)	% dimer (SANS)
Tel22	14.1±0.3	10.4 ± 0.4	5.0±0.1	0	0
Tel22-TMPyP4	24.0± 0.5	20.6±0.7	8.8±0.1	59± 3	58±3
i.t. 30s	24.2± 0.5	21.2±0.7	8.9±0.1	60± 3	62±3
i.t. 60s	24.6± 0.5	21.3±0.7	8.9±0.1	63± 3	60±3
i.t. 120s	24.8± 0.5	22.0±0.7	9.3±0.1	67± 3	69±3
i.t. 240s	24.8± 0.5	22.4±0.7	9.6±0.1	70± 3	79±3
i.t. 480s	25.2± 0.5	22.7±0.7	9.6±0.1	74± 3	80±3

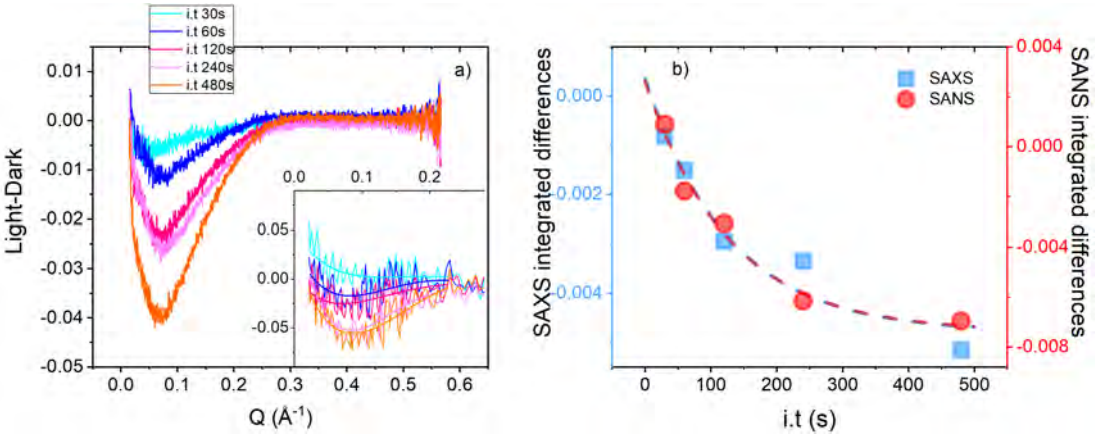

Figure 6.8: a) Difference of SAXS profiles (normalised to I(0)) between the irradiated and the dark (Tel22-TMPyP4). In the inset SANS differences. b) SAXS and SANS integrated (L-D) differences fitted by the $f(t)$. Figure taken from [86].

In whose case, the spectrum of Tel22-TMPyP4 (Dark) was subtracted from that of the exposed samples (Light) and both techniques show that the difference spectra have a minimum at low Q that increases with the exposure time. An exponential decay law $f(t) = A + Be^{-t/\tau}$ fit the integrated area above the curves, the SAXS and SANS data were simultaneously fitted sharing the saturation characteristic time τ, obtaining $\tau = 120 \pm 30s$. The difference, normalised to I(0), and the fitted data are shown in figure 6.8.

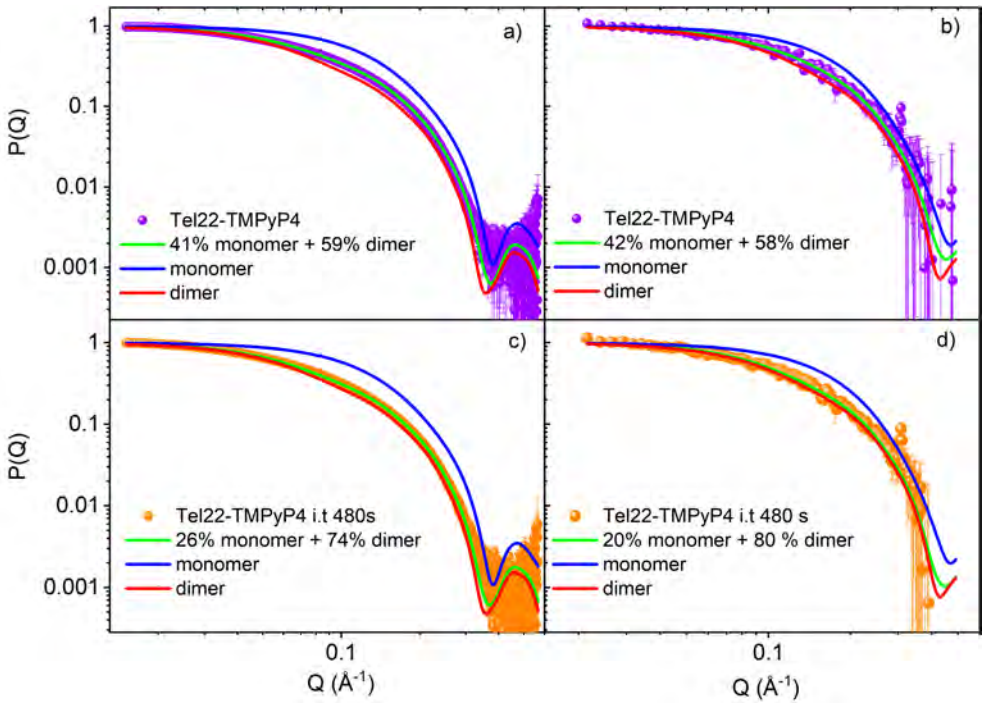

Figure 6.9: Experimental and theoretical patterns of Tel22-TMPyP4 and after irradiation of 480 s: SAXS (a,c) and SANS (b,d) form factor, normalised to one. In green the global fit, in blue the monomeric population, and in red the dimeric one. Figure from [86].

6.7 Correlation between secondary and quaternary structure

SAS experiments revealed the presence of elongated structures in the Tel22 solution induced by the complexation with the porphyrin TMPyP4 and irradiation with 430 nm light. Modelling the form factor, the percentage of dimers was determined for each spectrum. An intriguing aspect to investigate is whether it is possible to establish a correlation between the findings obtained from optical measurements (CD) and the scattering ones (SAS). Plotting the changes in the *ext*/*syn-anti* CD components *vs* the dimeric population percentage, a correlation/anticorrelation is found. As the elongated structures increase, the *ext* contribution grows, whereas the *syn-anti* decreases.

Figure 6.10 shows the secondary and quaternary (SQ) correlation plot, the dashed line represents the linear trend between these two structural changes on Tel22; interestingly, it does not intercept the point related to the Tel22 alone.

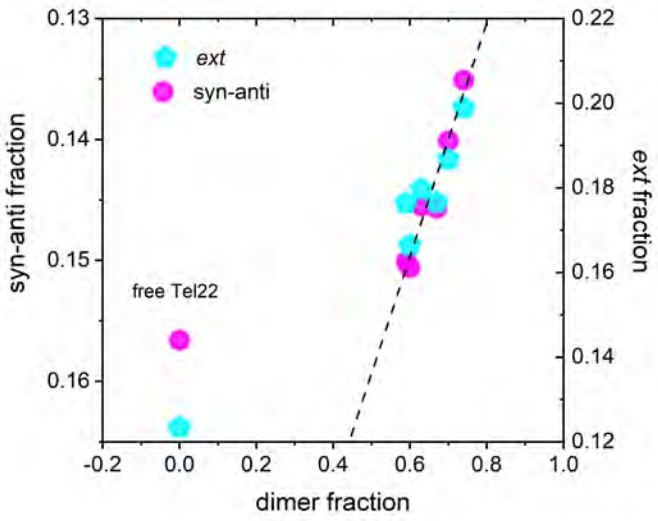

Figure 6.10: Secondary and quaternary correlation plot. Percentage of the *syn-anti* secondary structure (pink, left axis) and *ext* secondary structure (cyan, right axis) as a function of the fraction of Tel22 dimers obtained by SAXS data. Figure adapted from [86].

This behaviour suggests that, upon irradiation, the contribution of the secondary structure rearrangements on the stabilisation of dimers is not the same upon complexation. Looking at the percentage variations, complexation generates 60% of the dimers but only a variation of ~ 0.5 % in the *syn-anti* conformation and $\sim$ 4 % in the ext fraction, whereas, upon irradiation, the same secondary structure percentage change corresponds to an increase of the dimeric structure of only 15 %. The *ext* component, primarily attributes to terminal nucleotides, could be involved in the intermolecular contacts stabilising dimers. The *syn-anti* fraction decreases, most likely as a result of quartet distortion of the external tetrads, allowing the rise of a larger population of elongated forms.

To summarise:

- Tel22 is in a monomeric state in the investigated condition (500 μM, buffer K-phosphate).
- Porphyrin TMPyP4 induces sample dimerisation ($\sim$ 60%).
- Irradiation of Tel22-TMPyP4 with 430 nm light brings the dimer population to $\sim$ 80%.
- The complexation probably favours the dimer formation through its stack-

ing on the G4 tetrads, while the irradiation most likely through the oxidation of the external guanines.

Conclusions and perspectives

This thesis reports the results of a multi-technique biophysical approach applied to the study of the conformational changes triggered in G4s composed of a mixture of topologies. This kind of approach is particularly relevant in the case of telomeric sequences, which *in vitro* and *in vivo* have been shown to consist mainly of a mixture of hybrid conformations. This work is focused on the investigation of the telomeric archetypical sequence Tel22 $AG_3(TTAG_3)_3$, whose elusive and polymorphic structure is strongly influenced by the molecular environment and the experimental conditions.

In this framework, it is worthy of note that the structure of G4s resulting from the commonly used high-resolution techniques is very often different from the G4 topology in physiological conditions. X-ray crystallography and cryogenic electron microscopy need a sample preparation that alters the native structure, so they fail to give reliable insights into the structure of the G4 in solution. On the other hand, NMR measures the sample in conditions close to the physiological ones but, when the G4 has a mixture of conformations, the spectral features overlap and the contribution of the various topologies is very difficult to detect. Thus, a multi-technique approach overcomes these limitations and provides valuable low-resolution information on solutions containing a mix of conformations. To this aim, we combined different length-scale techniques, such as UV-Vis absorption and fluorescence to monitor the electronic properties, UVRR to investigate molecular vibrations, CD for the secondary structure, and SAS at large-scale facilities to visualise the overall G4 shape.

The first purpose of this work was to apply the multi-scale technique approach to study the effect of complexation with small molecules on the structural and thermodynamic properties of Tel22. The perspective is to develop new strategies for cancer therapeutics since ligand-induced G4 stabilisation inhibits the telomerase activity. It was found that Berberine and Palmatine, two well-known natural compounds already employed in pharmacological applications, induce small effects on Tel22 secondary structure while being quite effective in altering the evo-

lution of the G4 topological conformations upon melting. The presence of these two ligands indeed stabilises the G4 structure and produces intermediate states with an increased parallel-like topology compared to that of Tel22 alone. Furthermore, despite having a relatively similar chemical structure, Berberine causes partial quadruplex dimerisation more effectively than Palmatine. The interaction of Tel22 with Braco-19, rationally designed to bind G4s, was also studied and its capability to stabilise and to trigger secondary structure rearrangements towards antiparallel-like topology was shown. The hypochromic effect observed upon complexation in UVRR bands related to the guanines of the tetrads suggests an end-stacking Braco-19 binding mechanism.

The second aim was to employ two photosensitive ligands and subsequent light irradiation to induce Tel22 conformational changes and stabilisation/destabilisation. First of all, the protocol for optimising the irradiation parameters was determined and an *ad-hoc* experimental set-up was built. Then, Tel22 was complexed with DTE, a photo-responsive ligand that is subject to a photo-isomerisation when irradiated. Its open configuration induces a decrease of Tel22 CD intensity, suggesting a modification of the G-tetrad structure, which is partially restored when the complex is irradiated with blue light, responsible for DTE ring closure. Although the great potentiality of DTE photo-reversible interaction, complete reversibility on Tel22 complex was not observed. A major effect was obtained with TMPyP4 porphyrin complexation and irradiation. When Tel22 concentration is around tens of micromolar, TMPyP4 induces secondary structure changes and irradiation at 430 nm leads to guanine oxidation and consequent G-tetrad destabilisation. This finding has an impact on the thermal pathway of the complex, which is characterised by the presence of an intermediate state whose spectroscopic properties suggest that it may be a triplex. When the G4 concentration is one order of magnitude higher, the complexation induces a similar effect on the Tel22 secondary structure, and the results of small-angle scattering analysis disclose the formation of dimers. The guanine oxidation, produced by irradiation, gives rise to a structural rearrangement that promotes the formation of elongated structures of the same size as unirradiated dimers. A correlation between the secondary and quaternary structural changes was observed, and the degree of dimerisation was found to be strictly correlated with the topology modifications.

Overall, it was proven that the present multi-technique approach provides precious information on Tel22 conformational changes at different length scales and

it can be generally applied to other G4 structures, such as longer telomeric sequences, which cannot be resolved with conventional high-resolution techniques. Visible light irradiation shows extraordinary properties of tailoring the G4 structural modifications in complexes with photosensitive ligands. In the particular case of complexation of Tel22 with TMPyP4, illumination is capable of both partially distorting the tetrads and controlling the dimer fraction. The present study shows that light is a powerful trigger for G4 conformational and quaternary structural changes, with unmatched prospects and huge potential in several fields, from nanotechnology to anticancer therapy.

Schematic cartoon of the adopted multi-scale technique approach

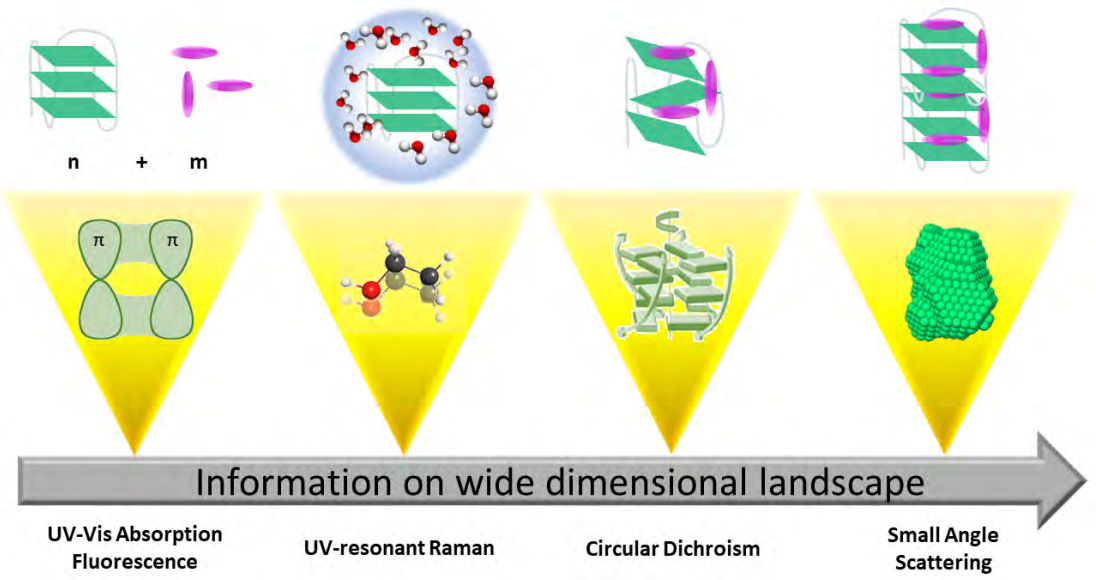

In perspective, G4 structures offer a versatile and tunable platform for developing nanoscale devices. A possible application could be using G4-ligand complex irradiation to control the assembly and disassembly of DNA-based nanostructures. A future goal could be to create structures that can undergo reversible conformational changes in response to light stimuli. These structures have potential applications in sensing and electronic devices. G4s-based logic gates are still in the early stages of development, however, they can be wherewithal for the development of new types of molecular computing devices and nanoscale technologies. G4 complexed with photosensitive ligands can also be used as smart

responsive material in drug delivery. Indeed, light could control drug release in a non-invasive manner.

Particular interest in perspective could be found in cancer treatment where, G4s have been identified as possible targets for photodynamic therapy (PDT) [160, 161]. PDT is a medical treatment that operates with a photosensitising agent, a light source, and oxygen to specifically destroy malignant cells. When the photosensitiser is activated by light of a specific wavelength, it generates reactive oxygen species (ROS), which can lead to cell death. In addition to lung cancer, esophageal cancer, skin cancer, and specific types of head and neck cancer, PDT is also used to treat a number of other medical disorders, such as psoriasis and acne. PDT is less invasive and safer than chemotherapy since it minimises the side effects. Indeed, PDT localises the effect around the cancerous cells rather than normal cells, which will not experience phototoxicity or a cumulative effect [162]. Moreover, targeting G4 structures can enhance the selectivity and effectiveness of PDT in cancer treatments, as many studies have confirmed the presence of G4s in promoter regions [38, 163, 164]. Huge attention has been devoted to the G4 related to c-Myc, vascular endothelial growth factor (VEGF), and BCL-2 gene expression. In particular, c-Myc is overexpressed in more than half of human cancers and, indeed, it is considered a molecular hallmark of tumours. The c-Myc oncogene plays a role in cell growth and proliferation [165, 166]. Its overexpression is linked to a variety of human cancers, including leukaemia, breast, colon, and cervical cancers [97, 167]. It is well known that VEGF participates in the initial stage of tumour development, allowing the cancer cells to form new blood vessels and then permitting their exponential growth, in progression and in metastasis [168]. Particularly, it is a marker for metastasis in human hepatocellular carcinoma [169]. BCL-2 family regulates cell apoptosis and makes easier tumour development. By targeting G4s in the promoter regions of these oncogenes, PDT can selectively inhibit the expression of these genes and induce cell death in cancer cells [170, 171]. Although some studies have been carried out, it is still essential to study G4-ligand interaction to develop more specific and compelling photosensitising agents. In this context, modified porphyrins may be perfect candidates since they have already been used as photosensitising agents, given their ability to produce ROS once irradiated with light [160, 161].

Furthermore, it has recently been proposed that when cells have telomere dysfunction, the RNA G4 TERRA, which is transcribed by telomers, encodes

two dipeptide repeat proteins [172]. In this context, a treatment that can work directly on telomere G-rich zones could stop the growth of these dipeptides, preventing changes in nucleic acid metabolism and inflammatory reactions.

For more generic medical applications, the structural characterisation at a low spatial resolution of the G4-ligand complexes before and after irradiation presented in this work can contribute to the design of new photosensitive molecules in order to increase their selectivity for G4 structures and reduce toxic effects. As a future perspective, the objective is to implement the methodology presented with time-resolved absorption and fluorescence spectroscopy (fs and ns resolution) to characterise the kinetics of photoinduced conformational changes in G4-ligand complexes. This profound characterisation of the complex could fit into the context of optogenetics, which consists of a class of methods developed to control cellular processes with high spatial and temporal precision using photoreceptors whose molecular interactions can be governed by light. The presented biophysical characterisation provides a first basis for establishing a rational approach to the design of optogenetic tools based on G4 ligands. They will in fact allow optimising the excitation patterns by light for optogenetic control and photoinduced structural reassembly.

References

[1] Angelika M Burger, Fangping Dai, Christoph M Schultes, Anthony P Reszka, Michael J Moore, John A Double, and Stephen Neidle. "The G-quadruplex-interactive molecule BRACO-19 inhibits tumor growth, consistent with telomere targeting and interference with telomerase function". *Cancer Research* 65.4, 1489–1496. 2005.

[2] Jochen Spiegel, Santosh Adhikari, and Shankar Balasubramanian. "The structure and function of DNA G-quadruplexes". *Trends in Chemistry* 2.2, 123–136. 2020.

[3] Mateus Webba da Silva. "Geometric formalism for DNA quadruplex folding". *Chemistry–A European Journal* 13.35, 9738–9745. 2007.

[4] Julian L Huppert and Shankar Balasubramanian. "Prevalence of quadruplexes in the human genome". *Nucleic Acids Research* 33.9, 2908–2916. 2005.

[5] Matthew L Bochman, Katrin Paeschke, and Virginia A Zakian. "DNA secondary structures: stability and function of G-quadruplex structures". *Nature Reviews Genetics* 13.11, 770–780. 2012.

[6] Robert Hänsel-Hertsch, Marco Di Antonio, and Shankar Balasubramanian. "DNA G-quadruplexes in the human genome: detection, functions and therapeutic potential". *Nature Reviews Molecular Cell Biology* 18.5, 279–284. 2017.

[7] James D Watson and Francis HC Crick. "Molecular structure of nucleic acids: a structure for deoxyribose nucleic acid". *Nature* 171.4356, 737–738. 1953.

[8] Martin Gellert, Marie N Lipsett, and David R Davies. "Helix formation by guanylic acid". *Proceedings of the National Academy of Sciences* 48.12, 2013–2018. 1962.

[9] Stephen Neidle, Shankar Balasubramanian, SF Campbell, M Clore, and DM Lilley. *Quadruplex nucleic acids*. Vol. 7. Royal Society of Chemistry Cambridge. 2006.

[10] Dipankar Sen and Walter Gilbert. "A sodium-potassium switch in the formation of four-stranded G4-DNA". *Nature* 344.6265, 410–414. 1990.

[11] Debmalya Bhattacharyya, Gayan Mirihana Arachchilage, and Soumitra Basu. "Metal cations in G-quadruplex folding and stability". *Frontiers in Chemistry* 4, 38. 2016.

[12] Dipankar Sen and Walter Gilbert. "Formation of parallel four-stranded complexes by guanine-rich motifs in DNA and its implications for meiosis". *Nature* 334.6180, 364–366. 1988.

[13] Wesley I Sundquist and Aaron Klug. "Telomeric DNA dimerizes by formation of guanine tetrads between hairpin loops". *Nature* 342.6251, 825–829. 1989.

[14] Eric Henderson, Charles C Hardin, Steven K Walk, Ignacio Tinoco Jr, and Elizabeth H Blackburn. "Telomeric DNA oligonucleotides form novel intramolecular structures containing guanine· guanine base pairs". *Cell* 51.6, 899–908. 1987.

[15] Christiane Schaffitzel, Imre Berger, Jan Postberg, Jozef Hanes, Hans J Lipps, and Andreas Plückthun. "In vitro generated antibodies specific for telomeric guanine-quadruplex DNA react with Stylonychia lemnae macronuclei". *Proceedings of the National Academy of Sciences* 98.15, 8572–8577. 2001.

[16] Giulia Biffi, David Tannahill, John McCafferty, and Shankar Balasubramanian. "Quantitative visualization of DNA G-quadruplex structures in human cells". *Nature Chemistry* 5.3, 182–186. 2013.

[17] Alexander Henderson, Yuliang Wu, Yu Chuan Huang, Elizabeth A Chavez, Jesse Platt, F Brad Johnson, Robert M Brosh, Dipankar Sen, and Peter M Lansdorp. "Detection of G-quadruplex DNA in mammalian cells". *Nucleic Acids Research* 42.2, 860–869. 2013.

[18] Alexander Henderson, Yuliang Wu, Yu Chuan Huang, Elizabeth A Chavez, Jesse Platt, F Brad Johnson, Robert M Brosh, Dipankar Sen, and Peter M Lansdorp. "Detection of G-quadruplex DNA in mammalian cells". *Nucleic Acids Research* 45.10, 6252–6252. 2017.

[19] Hui-Yun Liu, Qi Zhao, Tian-Peng Zhang, Yue Wu, Yun-Xia Xiong, Shi-Ke Wang, Yuan-Long Ge, Jin-Hui He, Peng Lv, Tian-Miao Ou, et al. "Conformation selective antibody enables genome profiling and leads to discovery of parallel G-quadruplex in human telomeres". *Cell Chemical Biology* 23.10, 1261–1270. 2016.

[20] Gary N Parkinson, Michael PH Lee, and Stephen Neidle. "Crystal structure of parallel quadruplexes from human telomeric DNA". *Nature* 417.6891, 876–880. 2002.

[21] Attila Ambrus, Ding Chen, Jixun Dai, Tiffanie Bialis, Roger A Jones, and Danzhou Yang. "Human telomeric sequence forms a hybrid-type intramolecular G-quadruplex structure with mixed parallel/antiparallel strands in potassium solution". *Nucleic Acids Research* 34.9, 2723–2735. 2006.

[22] Dengguo Wei, Gary N Parkinson, Anthony P Reszka, and Stephen Neidle. "Crystal structure of a c-kit promoter quadruplex reveals the structural role of metal ions and water molecules in maintaining loop conformation". *Nucleic Acids Research* 40.10, 4691–4700. 2012.

[23] Attila Ambrus, Ding Chen, Jixun Dai, Roger A Jones, and Danzhou Yang. "Solution structure of the biologically relevant G-quadruplex element in the human c-MYC promoter. Implications for G-quadruplex stabilization". *Biochemistry* 44.6, 2048–2058. 2005.

[24] Alan K Todd, Matthew Johnston, and Stephen Neidle. "Highly prevalent putative quadruplex sequence motifs in human DNA". *Nucleic Acids Research* 33.9, 2901–2907. 2005.

[25] Vineeth Thachappilly Mukundan and Anh Tuân Phan. "Bulges in G-quadruplexes: broadening the definition of G-quadruplex-forming sequences". *Journal of the American Chemical Society* 135.13, 5017–5028. 2013.

[26] Anjali Sengar, J Jeya Vandana, Vicki S Chambers, Marco Di Antonio, Fernaldo Richtia Winnerdy, Shankar Balasubramanian, and Anh Tuân Phan. "Structure of a (3+ 1) hybrid G-quadruplex in the PARP1 promoter". *Nucleic Acids Research* 47.3, 1564–1572. 2019.

[27] Aleksandr B Sahakyan, Vicki S Chambers, Giovanni Marsico, Tobias Santner, Marco Di Antonio, and Shankar Balasubramanian. "Machine learning model for sequence-driven DNA G-quadruplex formation". *Scientific Reports* 7.1, 1–11. 2017.

[28] Andreas Ioannis Karsisiotis, Christopher O'Kane, and Mateus Webba da Silva. "DNA quadruplex folding formalism–a tutorial on quadruplex topologies". *Methods* 64.1, 28–35. 2013.

[29] Scarlett A Dvorkin, Andreas I Karsisiotis, and Mateus Webba da Silva. "Encoding canonical DNA quadruplex structure". *Science Advances* 4.8, eaat3007. 2018.

[30] Vicki S Chambers, Giovanni Marsico, Jonathan M Boutell, Marco Di Antonio, Geoffrey P Smith, and Shankar Balasubramanian. "High-throughput sequencing of DNA G-quadruplex structures in the human genome". *Nature Biotechnology* 33.8, 877–881. 2015.

[31] Yun Ding, Aaron M Fleming, and Cynthia J Burrows. "Case studies on potential G-quadruplex-forming sequences from the bacterial orders Deinococcales and Thermales derived from a survey of published genomes". *Scientific Reports* 8.1, 1–11. 2018.

[32] Jennifer A Hackett, David M Feldser, and Carol W Greider. "Telomere dysfunction increases mutation rate and genomic instability". *Cell* 106.3, 275–286. 2001.

[33] Alan M Zahler, James R Williamson, Thomas R Cech, and David M Prescott. "Inhibition of telomerase by G-quartet DMA structures". *Nature* 350.6320, 718–720. 1991.

[34] Matthew Meyerson, Christopher M Counter, Elinor Ng Eaton, Leif W Ellisen, Philipp Steiner, Stephanie Dickinson Caddle, Liuda Ziaugra, Roderick L Beijersbergen, Michael J Davidoff, Qingyun Liu, et al. "hEST2, the putative human telomerase catalytic subunit gene, is up-regulated in tumor cells and during immortalization". *Cell* 90.4, 785–795. 1997.

[35] Nam W Kim, Mieczyslaw A Piatyszek, Karen R Prowse, Calvin B Harley, Michael D West, Peter LC Ho, Gina M Coviello, Woodring E Wright, Scott L Weinrich, and Jerry W Shay. "Specific association of human telomerase activity with immortal cells and cancer". *Science* 266.5193, 2011–2015. 1994.

[36] Julian Leon Huppert. "Four-stranded nucleic acids: structure, function and targeting of G-quadruplexes". *Chemical Society Reviews* 37.7, 1375–1384. 2008.

[37] Susanna Cogoi and Luigi E Xodo. "G-quadruplex formation within the promoter of the KRAS proto-oncogene and its effect on transcription". *Nucleic Acids Research* 34.9, 2536–2549. 2006.

[38] Tracy A Brooks, Samantha Kendrick, and Laurence Hurley. "Making sense of G-quadruplex and i-motif functions in oncogene promoters". *The FEBS Journal* 277.17, 3459–3469. 2010.

[39] Thomas S Dexheimer, Daekyu Sun, and Laurence H Hurley. "Deconvoluting the structural and drug-recognition complexity of the G-quadruplex-forming region upstream of the bcl-2 P1 promoter". *Journal of the American Chemical Society* 128.16, 5404–5415. 2006.

[40] Sarah Rankin, Anthony P Reszka, Julian Huppert, Mire Zloh, Gary N Parkinson, Alan K Todd, Sylvain Ladame, Shankar Balasubramanian, and Stephen Neidle. "Putative DNA quadruplex formation within the human c-kit oncogene". *Journal of the American Chemical Society* 127.30, 10584–10589. 2005.

[41] Daekyu Sun, Kexiao Guo, Jadrian J Rusche, and Laurence H Hurley. "Facilitation of a structural transition in the polypurine/polypyrimidine tract within the proximal promoter region of the human VEGF gene by the presence of potassium and G-quadruplex-interactive agents". *Nucleic Acids Research* 33.18, 6070–6080. 2005.

[42] Carolina Roxo, Weronika Kotkowiak, and Anna Pasternak. "G-quadruplex-forming aptamers—characteristics, applications, and perspectives". *Molecules* 24.20, 3781. 2019.

[43] I Bang. "Untersuchungen über die Guanylsäure". *Biochemische Zeitschrift* 26, 293–311. 1910.

[44] Arrigo Calzolari, Rosa Di Felice, Elisa Molinari, and Anna Garbesi. "G-quartet biomolecular nanowires". *Applied Physics Letters* 80.18, 3331–3333. 2002.

[45] Yahui Guo, Weirong Yao, Yunfei Xie, Xiaodong Zhou, Jiming Hu, and Renjun Pei. "Logic gates based on G-quadruplexes: principles and sensor applications". *Microchimica Acta* 183.1, 21–34. 2016.

[46] Liliya A Yatsunyk, Oscar Mendoza, and Jean-Louis Mergny. ""Nano-oddities": unusual nucleic acid assemblies for DNA-based nanostructures and nanodevices". *Accounts of Chemical Research* 47.6, 1836–1844. 2014.

[47] Robert K Moyzis, Judy M Buckingham, L Scott Cram, Maria Dani, Larry L Deaven, Myrna D Jones, Julianne Meyne, Robert L Ratliff, and Jung-Rung Wu. "A highly conserved repetitive DNA sequence,(TTAGGG) n, present at the telomeres of human chromosomes." *Proceedings of the National Academy of Sciences* 85.18, 6622–6626. 1988.

[48] Yong Wang and Dinshaw J Patel. "Solution structure of the human telomeric repeat d [AG3 (T2AG3) 3] G-tetraplex". *Structure* 1.4, 263–282. 1993.

[49] Jixun Dai, Chandanamali Punchihewa, Attila Ambrus, Ding Chen, Roger A Jones, and Danzhou Yang. "Structure of the intramolecular human telomeric G-quadruplex in potassium solution: a novel adenine triple formation". *Nucleic Acids Research* 35.7, 2440–2450. 2007.

[50] Jixun Dai, Megan Carver, Chandanamali Punchihewa, Roger A Jones, and Danzhou Yang. "Structure of the Hybrid-2 type intramolecular human telomeric G-quadruplex in K+ solution: insights into structure polymorphism of the human telomeric sequence". *Nucleic Acids Research* 35.15, 4927–4940. 2007.

[51] Daniel Renčiuk, Iva Kejnovská, Petra Školáková, Klára Bednářová, Jitka Motlová, and Michaela Vorlíčková. "Arrangements of human telomere DNA quadruplex in physiologically relevant K+ solutions". *Nucleic Acids Research* 37.19, 6625–6634. 2009.

[52] Hong-Liang Bao, Hong-shan Liu, and Yan Xu. "Hybrid-type and two-tetrad antiparallel telomere DNA G-quadruplex structures in living human cells". *Nucleic Acids Research* 47.10, 4940–4947. 2019.

[53] Qian Li, Jun-Feng Xiang, Qian-Fan Yang, Hong-Xia Sun, Ai-Jiao Guan, and Ya-Lin Tang. "G4LDB: a database for discovering and studying G-quadruplex ligands". *Nucleic Acids Research* 41.D1, D1115–D1123. 2013.

[54] David Monchaud and Marie-Paule Teulade-Fichou. "A hitchhiker's guide to G-quadruplex ligands". *Organic & biomolecular chemistry* 6.4, 627–636. 2008.

[55] Daekyu Sun, Brian Thompson, Brian E Cathers, Miguel Salazar, Sean M Kerwin, John O Trent, Terence C Jenkins, Stephen Neidle, and Laurence H Hurley. "Inhibition of human telomerase by a G-quadruplex-interactive compound". *Journal of Medicinal Chemistry* 40.14, 2113–2116. 1997.

[56] Richard T Wheelhouse, Daekyu Sun, Haiyong Han, Frank Xiaoguang Han, and Laurence H Hurley. "Cationic porphyrins as telomerase inhibitors: the interaction of tetra-(N-methyl-4-pyridyl) porphine with quadruplex DNA". *Journal of the American Chemical Society* 120.13, 3261–3262. 1998.

[57] Mu-Yong Kim, Hariprasad Vankayalapati, Kazuo Shin-Ya, Konstanty Wierzba, and Laurence H Hurley. "Telomestatin, a potent telomerase inhibitor that interacts quite specifically with the human telomeric intramolecular G-quadruplex". *Journal of the American Chemical Society* 124.10, 2098–2099. 2002.

[58] Kazuo Shin-ya, Konstanty Wierzba, Ken-ichi Matsuo, Toshio Ohtani, Yuji Yamada, Kazuo Furihata, Yoichi Hayakawa, and Haruo Seto. "Telomestatin, a novel telomerase inhibitor from Streptomyces anulatus". *Journal of the American Chemical Society* 123.6, 1262–1263. 2001.

[59] Rhianna K Morgan and Tracy A Brooks. "Targeting Promoter G-Quadruplexes for Transcriptional Control". *Small-Molecule Transcription Factor Inhibitors in Oncology*. Royal Society of Chemistry, 169–193. 2018.

[60] Denis Drygin, Adam Siddiqui-Jain, Sean O'Brien, Michael Schwaebe, Amy Lin, Josh Bliesath, Caroline B Ho, Chris Proffitt, Katy Trent, Jeffrey P Whitten, et al. "Anticancer activity of CX-3543: a direct inhibitor of rRNA biogenesis". *Cancer Research* 69.19, 7653–7661. 2009.

[61] Michael P O'Hagan, Javier Ramos-Soriano, Susanta Haldar, Sadiyah Sheikh, Juan C Morales, Adrian J Mulholland, and M Carmen Galan. "Visible-light photoswitching of ligand binding mode suggests G-quadruplex DNA as a target for photopharmacology". *Chemical Communications* 56.38, 5186–5189. 2020.

[62] Christiane Albrecht. *Joseph R. Lakowicz: Principles of fluorescence spectroscopy*. 2008.

[63] Antonio Randazzo, Gian Piero Spada, and Mateus Webba da Silva. "Circular dichroism of quadruplex structures". *Quadruplex Nucleic Acids*, 67–86. 2012.

[64] Gerald D Fasman. *Circular dichroism and the conformational analysis of biomolecules*. Springer Science & Business Media. 2013.

[65] Nina Berova, Koji Nakanishi, and Robert W Woody. *Circular dichroism: principles and applications*. John Wiley & Sons. 2000.

[66] Barbara Rossi, Cettina Bottari, Sara Catalini, Francesco D'Amico, Alessandro Gessini, and Claudio Masciovecchio. "Synchrotron-based ultraviolet resonance Raman scattering for material science". *Molecular and Laser Spectroscopy*. Elsevier, 447–482. 2020.

[67] Robert D Gray and Jonathan B Chaires. "Analysis of Multidimensional G-Quadruplex Melting Curves". *Current Protocols in Nucleic Acid Chemistry* 45.1, 17–4. 2011.

[68] Robert D Gray, Robert Buscaglia, and Jonathan B Chaires. "Populated intermediates in the thermal unfolding of the human telomeric quadruplex". *Journal of the American Chemical Society* 134.40, 16834–16844. 2012.

[69] ER Henry and J Hofrichter. "[8] Singular value decomposition: Application to analysis of experimental data". *Methods in Enzymology*. Vol. 210. Elsevier, 129–192. 1992.

[70] DI Svergun. "Determination of the regularization parameter in indirect-transform methods using perceptual criteria". *Journal of Applied Crystallography* 25.4, 495–503. 1992.

[71] Boualem Hammouda. "Probing nanoscale structures-the sans toolbox". *National Institute of Standards and Technology*, 1–717. 2008.

[72] David A Jacques and Jill Trewhella. "Small-angle scattering for structural biology—Expanding the frontier while avoiding the pitfalls". *Protein Science* 19.4, 642–657. 2010.

[73] Benedetta Petra Rosi, Valeria Libera, Andrea Orecchini, Silvia Corezzi, Giorgio Schirò, Petra Pernot, Caterina Petrillo, Lucia Comez, Cristiano De Michele, and Alessandro Paciaroni. "Connecting Structure, Conformation and Energetics of Human Telomere G-quadruplex Multimers". *arXiv preprint arXiv:2203.06521*. 2022.

[74] Leigh B Clark. "Electronic spectra of crystalline guanosine: transition moment directions of the guanine chromophore". *Journal of the American Chemical Society* 116.12, 5265–5270. 1994.

[75] Markus P Fülscher, Luis Serrano-Andrés, and Björn O Roos. "A theoretical study of the electronic spectra of adenine and guanine". *Journal of the American Chemical Society* 119.26, 6168–6176. 1997.

[76] Nobuyuki Harada and Kōji Nakanishi. *Circular dichroic spectroscopy: exciton coupling in organic stereochemistry*. Univ Science Books. 1983.

[77] Rafael del Villar-Guerra, John O Trent, and Jonathan B Chaires. "G-quadruplex secondary structure obtained from circular dichroism spectroscopy". *Angewandte Chemie* 130.24, 7289–7293. 2018.

[78] Werner Hug and Ignacio Tinoco. "Electronic spectra of nucleic acid bases. I. Interpretation of the in-plane spectra with the aid of all valence electron MO-CIA [configuration interaction] calculations". *Journal of the American Chemical Society* 95.9, 2803–2813. 1973.

[79] Federico Bianchi, Lucia Comez, Ralf Biehl, Francesco D'Amico, Alessandro Gessini, Marialucia Longo, Claudio Masciovecchio, Caterina Petrillo, Aurel Radulescu, Barbara Rossi, et al. "Structure of human telomere G-quadruplex in the presence of a model drug along the thermal unfolding pathway". *Nucleic Acids Research* 46.22, 11927–11938. 2018.

[80] Dmitri I Svergun and Michel HJ Koch. "Small-angle scattering studies of biological macromolecules in solution". *Reports on Progress in Physics* 66.10, 1735. 2003.

[81] Cy M Jeffries and Dmitri I Svergun. "High-throughput studies of protein shapes and interactions by synchrotron small-angle X-ray scattering". *Structural Proteomics: High-Throughput Methods*, 277–301. 2015.

[82] Petra Pernot, Adam Round, Ray Barrett, Alejandro De Maria Antolinos, Alexandre Gobbo, Elspeth Gordon, Julien Huet, Jerôme Kieffer, Mario Lentini, Muriel Mattenet, et al. "Upgraded ESRF BM29 beamline for SAXS on macromolecules in solution". *Journal of synchrotron radiation* 20.4, 660–664. 2013.

[83] John W. Eaton. *GNU Octave Manual*. Network Theory Limited. 2002. ISBN: 0-9541617-2-6.

[84] Thomas Williams, Colin Kelley, and many others. *Gnuplot 4.6: an interactive plotting program*. `http://gnuplot.sourceforge.net/`. 2013.

[85] Valeria Libera, Federico Bianchi, Barbara Rossi, Francesco D'Amico, Claudio Masciovecchio, Caterina Petrillo, Francesco Sacchetti, Alessandro Paciaroni, and Lucia Comez. "Solvent vibrations as a proxy of the telomere G-quadruplex rearrangements across thermal unfolding". *International Journal of Molecular Sciences* 23.9, 5123. 2022.

[86] Valeria Libera, Elena A Andreeva, Anne Martel, Aurelien Thureau, Marialucia Longo, Caterina Petrillo, Alessandro Paciaroni, Giorgio Schirò, and Lucia Comez. "Porphyrin Binding and Irradiation Promote G-Quadruplex DNA Dimeric Structure". *The Journal of Physical Chemistry Letters* 12.33, 8096–8102. 2021.

[87] L Comez, F Bianchi, V Libera, M Longo, C Petrillo, F Sacchetti, F Sebastiani, F D'Amico, B Rossi, A Gessini, et al. "Polymorphism of human telomeric quadruplexes with drugs: A multi-technique biophysical study". *Physical Chemistry Chemical Physics* 22.20, 11583–11592. 2020.

[88] Stephen PA Fodor, Richard P Rava, Thomas R Hays, and Thomas G Spiro. "Ultraviolet resonance Raman spectroscopy of the nucleotides with 266-, 240-, 218-, and 200-nm pulsed laser excitation". *Journal of the American Chemical Society* 107.6, 1520–1529. 1985.

[89] Joseph R Perno, Christine A Grygon, and Thomas G Spiro. "Ultraviolet Raman excitation profiles for the nucleotides and for the nucleic acid duplexes poly (rA)-poly-(rU) and poly (dG-dC)". *The Journal of Physical Chemistry* 93.15, 5672–5678. 1989.

[90] Enoch W Small and Warner L Peticolas. "Conformational dependence of the Raman scattering intensities from polynucleotides". *Biopolymers: Original Research on Biomolecules* 10.1, 69–88. 1971.

[91] Kurt Andresen, R Das, Hye Yoon Park, H Smith, Lisa W Kwok, Jessica S Lamb, EJ Kirkland, D Herschlag, KD Finkelstein, and Lois Pollack. "Spatial distribution of competing ions around DNA in solution". *Physical Review Letters* 93.24, 248103. 2004.

[92] Steve P Meisburger, Suzette A Pabit, and Lois Pollack. "Determining the locations of ions and water around DNA from X-ray scattering measurements". *Biophysical Journal* 108.12, 2886–2895. 2015.

[93] Sofia Kolesnikova and Edward A Curtis. "Structure and function of multimeric G-quadruplexes". *Molecules* 24.17, 3074. 2019.

[94] Luigi Petraccone, Bruno Pagano, and Concetta Giancola. "Studying the effect of crowding and dehydration on DNA G-quadruplexes". *Methods* 57.1, 76–83. 2012.

[95] Haiqing Yu, Xiaobo Gu, Shu-ichi Nakano, Daisuke Miyoshi, and Naoki Sugimoto. "Beads-on-a-string structure of long telomeric DNAs under molecular crowding conditions". *Journal of the American Chemical Society* 134.49, 20060–20069. 2012.

[96] Daisuke Miyoshi, Hisae Karimata, and Naoki Sugimoto. "Hydration regulates thermodynamics of G-quadruplex formation under molecular crowding conditions". *Journal of the American Chemical Society* 128.24, 7957–7963. 2006.

[97] M Clarke Miller, Robert Buscaglia, Jonathan B Chaires, Andrew N Lane, and John O Trent. "Hydration is a major determinant of the G-quadruplex stability and conformation of the human telomere 3' sequence of d (AG3 (TTAG3) 3)". *Journal of the American Chemical Society* 132.48, 17105–17107. 2010.

[98] Kevin Li, Liliya Yatsunyk, and Stephen Neidle. "Water spines and networks in G-quadruplex structures". *Nucleic Acids Research* 49.1, 519–528. 2021.

[99] Jan Palackỳ, Peter Mojzeš, Iva Kejnovská, and Michaela Vorlíčková. "Does Raman spectroscopy recognize different G-quadruplex arrangements?" *Journal of Raman Spectroscopy* 51.2, 301–312. 2020.

[100] Cettina Bottari, L Comez, M Paolantoni, S Corezzi, F D'Amico, A Gessini, C Masciovecchio, and B Rossi. "Hydration properties and water structure in aqueous solutions of native and modified cyclodextrins by UV R aman and B rillouin scattering". *Journal of Raman Spectroscopy* 49.6, 1076–1085. 2018.

[101] JL Green, AR Lacey, and MG Sceats. "Spectroscopic evidence for spatial correlations of hydrogen bonds in liquid water". *The Journal of Physical Chemistry* 90.17, 3958–3964. 1986.

[102] GE Walrafen and YC Chu. "Linearity between structural correlation length and correlated-proton Raman intensity from amorphous ice and supercooled water up to dense supercritical steam". *The Journal of Physical Chemistry* 99.28, 11225–11229. 1995.

[103] GE Walrafen. "Effects of equilibrium H-bond distance and angle changes on Raman intensities from water". *The Journal of chemical physics* 120.10, 4868–4876. 2004.

[104] JD Eaves, JJ Loparo, Ch J Fecko, ST Roberts, A Tokmakoff, and PL Geissler. "Hydrogen bonds in liquid water are broken only fleetingly". *Proceedings of the National Academy of Sciences* 102.37, 13019–13022. 2005.

[105] M Paolantoni, N Faginas Lago, M Albertí, and A Laganà. "Tetrahedral ordering in water: Raman profiles and their temperature dependence". *The Journal of Physical Chemistry A* 113.52, 15100–15105. 2009.

[106] Marco Franceschin, Luigi Rossetti, Anna D'Ambrosio, Stefano Schirripa, Armandodoriano Bianco, Giancarlo Ortaggi, Maria Savino, Christoph Schultes, and Stephen Neidle. "Natural and synthetic G-quadruplex interactive berberine derivatives". *Bioorganic & Medicinal Chemistry Letters* 16.6, 1707–1711. 2006.

[107] Amit Arora, Chandramouli Balasubramanian, Niti Kumar, Saurabh Agrawal, Rajendra P Ojha, and Souvik Maiti. "Binding of berberine to human telomeric quadruplex–spectroscopic, calorimetric and molecular modeling studies". *The FEBS Journal* 275.15, 3971–3983. 2008.

[108] Kakali Bhadra and Gopinatha Suresh Kumar. "Interaction of berberine, palmatine, coralyne, and sanguinarine to quadruplex DNA: a comparative spectroscopic and calorimetric study". *Biochimica et Biophysica Acta (BBA)-General Subjects* 1810.4, 485–496. 2011.

[109] Nagendra Sastry Yarla, Anupam Bishayee, Gautam Sethi, Pallu Reddanna, Arunasree M Kalle, Bhadrapura Lakkappa Dhananjaya, Kaladhar SVGK Dowluru, Ramakrishna Chintala, and Govinda Rao Duddukuri. "Targeting arachidonic acid pathway by natural products for cancer prevention and therapy". *Seminars in Cancer Biology*. Vol. 40. Elsevier, 48–81. 2016.

[110] Seong Baek Yang, Eun Hee Kim, Seung Hee Kim, Young Hun Kim, Weontae Oh, Jin-Tae Lee, Young-Ah Jang, Yeasmin Sabina, Byung Chul Ji, and Jeong Hyun Yeum. "Electrospinning fabrication of poly (vinyl alcohol)/coptis chinensis extract nanofibers for antimicrobial exploits". *Nanomaterials* 8.9, 734. 2018.

[111] Danyang Song, Jianyu Hao, and Daiming Fan. "Biological properties and clinical applications of berberine". *Frontiers of Medicine* 14, 564–582. 2020.

[112] Jiaying Long, Jiawen Song, Li Zhong, Yanmei Liao, Luona Liu, and Xiaofang Li. "Palmatine: a review of its pharmacology, toxicity and pharmacokinetics". *Biochimie* 162, 176–184. 2019.

[113] Roberta Rocca, Federica Moraca, Giosuè Costa, Stefano Alcaro, Simona Distinto, Elias Maccioni, Francesco Ortuso, Anna Artese, and Lucia Parrotta. "Structure-based virtual screening of novel natural alkaloid derivatives as potential binders of h-telo and c-myc DNA G-quadruplex conformations". *Molecules* 20.1, 206–223. 2014.

[114] Xiaohui Ji, Hongxia Sun, Huaxi Zhou, Junfeng Xiang, Yalin Tang, and Changqi Zhao. "The interaction of telomeric DNA and C-myc22 G-quadruplex with 11 natural alkaloids". *Nucleic Acid Therapeutics* 22.2, 127–136. 2012.

[115] M Doucet, JH Cho, G Alina, J Bakker, W Bouwman, P Butler, K Campbell, M Gonzales, R Heenan, A Jackson, et al. "SasView". *Version In* 5. 2019.

[116] Martin Read, R John Harrison, Barbara Romagnoli, Farial A Tanious, Sharon H Gowan, Anthony P Reszka, W David Wilson, Lloyd R Kelland, and Stephen Neidle. "Structure-based design of selective and potent G quadruplex-mediated telomerase inhibitors". *Proceedings of the National Academy of Sciences* 98.9, 4844–4849. 2001.

[117] Mekala Gunaratnam, Olga Greciano, Cristina Martins, Anthony P Reszka, Christoph M Schultes, Hamid Morjani, Jean-Francois Riou, and Stephen Neidle. "Mechanism of acridine-based telomerase inhibition and telomere shortening". *Biochemical Pharmacology* 74.5, 679–689. 2007.

[118] Guangtong Zhou, Xinrui Liu, Yunqian Li, Songbai Xu, Chengyuan Ma, Xinmin Wu, Ye Cheng, Zhiyun Yu, Gang Zhao, and Yong Chen. "Telomere targeting with a novel G-quadruplex-interactive ligand BRACO-19 induces T-loop disassembly and telomerase displacement in human glioblastoma cells". *Oncotarget* 7.12, 14925. 2016.

[119] Emanuela Ruggiero and Sara N Richter. "Viral G-quadruplexes: New frontiers in virus pathogenesis and antiviral therapy". *Annual Reports in Medicinal Chemistry*. Vol. 54. Elsevier, 101–131. 2020.

[120] Sara Artusi, Matteo Nadai, Rosalba Perrone, Maria Angela Biasolo, Giorgio Palu, Louis Flamand, Arianna Calistri, and Sara N Richter. "The Herpes Simplex Virus-1 genome contains multiple clusters of repeated G-quadruplex: Implications for the antiviral activity of a G-quadruplex ligand". *Antiviral Research* 118, 123–131. 2015.

[121] Bruno Pagano, Nunzia Iaccarino, Anna Di Porzio, Antonio Randazzo, and Jussara Amato. "Screening of DNA G-quadruplex stabilizing ligands by nano differential scanning fluorimetry". *Analyst* 144.22, 6512–6516. 2019.

[122] Alessia Pagano, Nunzia Iaccarino, Mahmoud AS Abdelhamid, Diego Brancaccio, Emanuele U Garzarella, Anna Di Porzio, Ettore Novellino, Zoë AE Waller, Bruno Pagano, Jussara Amato, et al. "Common G-quadruplex binding agents found to interact with i-motif-forming DNA: Unexpected multi-target-directed compounds". *Frontiers in Chemistry* 6, 281. 2018.

[123] Babitha Machireddy, Holli-Joi Sullivan, and Chun Wu. "Binding of BRACO19 to a telomeric G-quadruplex DNA probed by all-atom molecular dynamics simulations with explicit solvent". *Molecules* 24.6, 1010. 2019.

[124] David Moreira, Daniela Leitão, Jéssica Lopes-Nunes, Tiago Santos, Joana Figueiredo, André Miranda, Daniela Alexandre, Cândida Tomaz, Jean-Louis Mergny, and Carla Cruz. "G-Quadruplex Aptamer-Ligand Characterization". *Molecules* 27.20, 6781. 2022.

[125] Chunying Wei, Guoqing Jia, Jingli Yuan, Zhaochi Feng, and Can Li. "A spectroscopic study on the interactions of porphyrin with G-quadruplex DNAs". *Biochemistry* 45.21, 6681–6691. 2006.

[126] Loryn R Keating and Veronika A Szalai. "Parallel-stranded guanine quadruplex interactions with a copper cationic porphyrin". *Biochemistry* 43.50, 15891–15900. 2004.

[127] Elizabeth W White, Farial Tanious, Mohamed A Ismail, Anthony P Reszka, Stephen Neidle, David W Boykin, and W David Wilson. "Structure-specific recognition of quadruplex DNA by organic cations: influence of shape, substituents and charge". *Biophysical Chemistry* 126.1-3, 140–153. 2007.

[128] Balayeshwanth R Vummidi, Jawad Alzeer, and Nathan W Luedtke. "Fluorescent probes for G-quadruplex structures". *ChemBioChem* 14.5, 540–558. 2013.

[129] Jan Kapuscinski, Zbigniew Darzynkiewicz, and Myron R Melamed. "Interactions of acridine orange with nucleic acids: properties of complexes of acridine orange with single stranded ribonucleic acid". *Biochemical Pharmacology* 32.24, 3679–3694. 1983.

[130] JB Birks. "Excimers". *Reports on Progress in Physics* 38.8, 903. 1975.

[131] Zhaochao Xu, Suki Kim, Keun-Hyeung Lee, and Juyoung Yoon. "A highly selective fluorescent chemosensor for dihydrogen phosphate via unique excimer formation and PET mechanism". *Tetrahedron letters* 48.22, 3797–3800. 2007.

[132] Patrizia Alberti, Philippe Schmitt, Chi-Hung Nguyen, Christian Rivalle, Magali Hoarau, David S Grierson, and Jean-Louis Mergny. "Benzoindoloquinolines interact with DNA tetraplexes and inhibit telomerase". *Bioorganic & Medicinal Chemistry Letters* 12.7, 1071–1074. 2002.

[133] Michael JB Moore, Francisco Cuenca, Mark Searcey, and Stephen Neidle. "Synthesis of distamycin A polyamides targeting G-quadruplex DNA". *Organic & Biomolecular Chemistry* 4.18, 3479–3488. 2006.

[134] Masahiro Irie, Thorsten Lifka, Kingo Uchida, Seiya Kobatake, and Yuriko Shindo. "Fatigue resistant properties of photochromic dithienylethenes: by-product formation". *Chemical Communications* 8, 747–750. 1999.

[135] Hui-Juan Zhang, Xue-Fei Wang, Peng Wang, Xi-Cheng Ai, and Jian-Ping Zhang. "Spectroscopic study on the binding of a cationic porphyrin to DNA G-quadruplex under different K+ concentrations". *Photochemical & Photobiological Sciences* 7.8, 948–955. 2008.

[136] Haiyong Han, David R Langley, Anupama Rangan, and Laurence H Hurley. "Selective interactions of cationic porphyrins with G-quadruplex structures". *Journal of the American Chemical Society* 123.37, 8902–8913. 2001.

[137] Hajime Mita, Takako Ohyama, Yoshiyuki Tanaka, and Yasuhiko Yamamoto. "Formation of a complex of 5, 10, 15, 20-tetrakis (N-methylpyridinium-4-yl)-21 H, 23 H-porphyrin with G-quadruplex DNA". *Biochemistry* 45.22, 6765–6772. 2006.

[138] Ihtshamul Haq, John O Trent, Babur Z Chowdhry, and Terence C Jenkins. "Intercalative G-tetraplex stabilization of telomeric DNA by a cationic porphyrin1". *Journal of the American Chemical Society* 121.9, 1768–1779. 1999.

[139] Luigi Martino, Bruno Pagano, Iolanda Fotticchia, Stephen Neidle, and Concetta Giancola. "Shedding light on the interaction between TMPyP4 and human telomeric quadruplexes". *The Journal of Physical Chemistry B* 113.44, 14779–14786. 2009.

[140] Shuntaro Takahashi, Sudipta Bhowmik, Shinobu Sato, Shigeori Takenaka, and Naoki Sugimoto. "Replication Control of Human Telomere G-Quadruplex DNA by G-Quadruplex Ligands Dependent on Solution Environment". *Life* 12.4, 553. 2022.

[141] Kexiao Guo, Vijay Gokhale, Laurence H Hurley, and Daekyu Sun. "Intramolecularly folded G-quadruplex and i-motif structures in the proximal promoter of the vascular endothelial growth factor gene". *Nucleic Acids Research* 36.14, 4598–4608. 2008.

[142] Yong Qin, Evonne M Rezler, Vijay Gokhale, Daekyu Sun, and Laurence H Hurley. "Characterization of the G-quadruplexes in the duplex nuclease hypersensitive element of the PDGF-A promoter and modulation of PDGF-A promoter activity by TMPyP4". *Nucleic Acids Research* 35.22, 7698–7713. 2007.

[143] Elzbieta Izbicka, Richard T Wheelhouse, Eric Raymond, Karen K Davidson, Richard A Lawrence, Daekyu Sun, Bradford E Windle, Laurence H Hurley, and Daniel D Von Hoff. "Effects of cationic porphyrins as G-quadruplex interactive agents in human tumor cells". *Cancer Research* 59.3, 639–644. 1999.

[144] Mekala Gunaratnam, Stephen Swank, Shozeb M Haider, Katja Galesa, Anthony P Reszka, Monica Beltran, Francisco Cuenca, Jonathan A Fletcher, and Stephen Neidle. "Targeting human gastrointestinal stromal tumor cells with a quadruplex-binding small molecule". *Journal of Medicinal Chemistry* 52.12, 3774–3783. 2009.

[145] Robert F Pasternack, Peter R Huber, P Boyd, G Engasser, L Francesconi, E Gibbs, P Fasella, G Cerio Venturo, and L deC Hinds. "Aggregation of meso-substituted water-soluble porphyrins". *Journal of the American Chemical Society* 94.13, 4511–4517. 1972.

[146] Jia Zhou, Aaron M Fleming, April M Averill, Cynthia J Burrows, and Susan S Wallace. "The NEIL glycosylases remove oxidized guanine lesions

from telomeric and promoter quadruplex DNA structures". *Nucleic Acids Research* 43.8, 4039–4054. 2015.

[147] Aaron M Fleming and Cynthia J Burrows. "G-quadruplex folds of the human telomere sequence alter the site reactivity and reaction pathway of guanine oxidation compared to duplex DNA". *Chemical Research in Toxicology* 26.4, 593–607. 2013.

[148] Shinji Oikawa, Saeko Tada-Oikawa, and Shosuke Kawanishi. "Site-specific DNA damage at the GGG sequence by UVA involves acceleration of telomere shortening". *Biochemistry* 40.15, 4763–4768. 2001.

[149] Maureen B Poh-Fitzpatrick. "[43] Porphyrias: Photosensitivity and phototherapy". *Methods in Enzymology* 319, 485–493. 2000.

[150] Zhenhua Liu, Hui Li, Zejie Tian, Xin Liu, Yu Guo, Jun He, Zhenyu Wang, Tao Zhou, and Yunmei Liu. "Porphyrin-Based Nanoparticles: A Promising Phototherapy Platform". *ChemPlusChem* 87.8, e202200156. 2022.

[151] Johan Moan. "Porphyrin photosensitization and phototherapy". *Photochemistry and Photobiology* 43.6, 681–690. 1986.

[152] Deepak Koirala, Tomoko Mashimo, Yuta Sannohe, Zhongbo Yu, Hanbin Mao, and Hiroshi Sugiyama. "Intramolecular folding in three tandem guanine repeats of human telomeric DNA". *Chemical Communications* 48.14, 2006–2008. 2012.

[153] Zhenjiang Zhang, Jixun Dai, Elizabeth Veliath, Roger A Jones, and Danzhou Yang. "Structure of a two-G-tetrad intramolecular G-quadruplex formed by a variant human telomeric sequence in K+ solution: insights into the interconversion of human telomeric G-quadruplex structures". *Nucleic Acids Research* 38.3, 1009–1021. 2010.

[154] Jixun Dai, Megan Carver, and Danzhou Yang. "Polymorphism of human telomeric quadruplex structures". *Biochimie* 90.8, 1172–1183. 2008.

[155] Dian GT Su, Huafeng Fang, Michael L Gross, and John-Stephen A Taylor. "Photocrosslinking of human telomeric G-quadruplex loops by anti cyclobutane thymine dimer formation". *Proceedings of the National Academy of Sciences* 106.31, 12861–12866. 2009.

[156] Tomoko Mashimo, Yuta Sannohe, Hirotaka Yagi, and Hiroshi Sugiyama. "Folding pathways of hybrid-1 and hybrid-2 G-quadruplex structures". *Nucleic Acids Symposium Series*. Vol. 52. 1. Oxford University Press, 409–410. 2008.

[157] Robert D Gray, Jing Li, and Jonathan B Chaires. "Energetics and kinetics of a conformational switch in G-quadruplex DNA". *The Journal of Physical Chemistry B* 113.9, 2676–2683. 2009.

[158] Tomoko Mashimo, Hirotaka Yagi, Yuta Sannohe, Arivazhagan Rajendran, and Hiroshi Sugiyama. "Folding pathways of human telomeric type-1 and type-2 G-quadruplex structures". *Journal of the American Chemical Society* 132.42, 14910–14918. 2010.

[159] Charles R Cantor, Myron M Warshaw, and Herman Shapiro. "Oligonucleotide interactions. III. Circular dichroism studies of the conformation of deoxyoligonucleolides". *Biopolymers: Original Research on Biomolecules* 9.9, 1059–1077. 1970.

[160] Keiko Kawauchi, Ryoto Urano, Natsuki Kinoshita, Shin Kuwamoto, Takeru Torii, Yoshiki Hashimoto, Shinya Taniguchi, Mitsuki Tsuruta, and Daisuke Miyoshi. "Photosensitizers based on G-quadruplex ligand for cancer photodynamic therapy". *Genes* 11.11, 1340. 2020.

[161] Meng Cheng, Yun-Xi Cui, Jing Wang, Jing Zhang, Li-Na Zhu, and De-Ming Kong. "G-quadruplex/porphyrin composite photosensitizer: a facile way to promote absorption redshift and photodynamic therapy efficacy". *ACS applied materials & interfaces* 11.14, 13158–13167. 2019.

[162] Ahmed El-Hussein, Sello L Manoto, Saturnin Ombinda-Lemboumba, Ziya A Alrowaili, and Patience Mthunzi-Kufa. "A review of chemotherapy and photodynamic therapy for lung cancer treatment". *Anti-Cancer Agents in Medicinal Chemistry (Formerly Current Medicinal Chemistry-Anti-Cancer Agents)* 21.2, 149–161. 2021.

[163] Shankar Balasubramanian and Stephen Neidle. "G-quadruplex nucleic acids as therapeutic targets". *Current opinion in chemical biology* 13.3, 345–353. 2009.

[164] Julian L Huppert and Shankar Balasubramanian. "G-quadruplexes in promoters throughout the human genome". *Nucleic acids research* 35.2, 406–413. 2007.

[165] Cameron D Little, Marion M Nau, Desmond N Carney, Adi F Gazdar, and John D Minna. "Amplification and expression of the c-myc oncogene in human lung cancer cell lines". *Nature* 306.5939, 194–196. 1983.

[166] SJ Garte. "The c-myc oncogene in tumor progression." *Critical reviews in oncogenesis* 4.4, 435–449. 1993.

[167] Bing-Jia Chen, Yan-Ling Wu, Yoshimasa Tanaka, and Wen Zhang. "Small molecules targeting c-Myc oncogene: promising anti-cancer therapeutics". *International journal of biological sciences* 10.10, 1084. 2014.

[168] Henk MW Verheul and Herbert M Pinedo. "The role of vascular endothelial growth factor (VEGF) in tumor angiogenesis and early clinical development of VEGFReceptor kinase inhibitors". *Clinical Breast Cancer* 1, S80–S84. 2000.

[169] Lei Zhang, Jia-Ning Wang, Jun-Ming Tang, Xia Kong, Jian-Ye Yang, Fei Zheng, Ling-Yun Guo, Yong-Zhang Huang, Li Zhang, Lin Tian, et al. "VEGF is essential for the growth and migration of human hepatocellular carcinoma cells". *Molecular biology reports* 39, 5085–5093. 2012.

[170] Anna Frenzel, Francesca Grespi, Waldemar Chmelewskij, and Andreas Villunger. "Bcl2 family proteins in carcinogenesis and the treatment of cancer". *Apoptosis* 14, 584–596. 2009.

[171] Shanna Qian, Zhong Wei, Wanting Yang, Jinling Huang, Yinfeng Yang, and Jinghui Wang. "The role of BCL-2 family proteins in regulating apoptosis and cancer therapy". *Frontiers in Oncology* 12. 2022.

[172] Taghreed M Al-Turki and Jack D Griffith. "Mammalian telomeric RNA (TERRA) can be translated to produce valine–arginine and glycine–leucine dipeptide repeat proteins". *Proceedings of the National Academy of Sciences* 120.9, e2221529120. 2023.